Inertia Supervision for BESS Grid-forming Inverter

TESI DI LAUREA MAGISTRALE IN
Electrical ENGINEERING
INGEGNERIA Elettrica

Author: **Seifeldin Nafea**

Student ID: 994720
Advisor: Roberto Perini
Co-advisor: Francesco Palombi
Academic Year: 2023-2024

Abstract

This thesis addresses the increasing need for sophisticated grid stability solutions in the context of growing renewable energy integration. The study's uniqueness come from its focus on the application of Battery Energy Storage Systems (BESS) to provide ancillary services, particularly in enhancing grid inertia. The work explores novel grid-forming inverter technologies that allow BESS to emulate the inertial response of conventional synchronous generators. The thesis takes a comprehensive approach, beginning with examination of BESS role in ancillary services, highlighting their fast response and versatility. It proceeds to analysis different grid-forming control methods, concentrating on the Virtual Synchronous Machine (VSM), Generalized Virtual Synchronous Generator (GVSG), and Compensated Generalized Virtual Synchronous Generator (CGVSG) approaches. The control structure is defined to include outer voltage controller and inner current controller to avoid steady-state errors and introduce current limitation strategies. A virtual impedance is added to achieve decoupled active and reactive power flow. The methodology main objective is to model and tune the VSM, GVSG, and CGVSG blocks to achieve constant inertial response with good dynamics. Dynamic simulations using Simulink are performed, assessing the response of these systems under frequency perturbations and power setpoint changes. Moreover, the effectiveness of varying short circuit ratio (SCR) on the dynamics of these systems is investigated to examine how much they preserve their response.

The research findings reveal that specific grid-forming control methods, namely the VSM and Compensated GVSG, effectively provide constant inertial response, offer good transient response, and comparatively maintain response dynamics with SCR adjustments. The study demonstrates how these systems can offer grid support, ensuring more stable and reliable grid operations, particularly in areas with a high renewable energy penetration.

Key-words: BESS, inertia, short circuit ratio, VSM, GVSG, CGVSG.

Abstract in italiano

Questa tesi affronta la crescente necessità di soluzioni sofisticate per la stabilità della rete nel contesto della crescente integrazione delle energie rinnovabili. L'unicità dello studio deriva dal suo focus sull'applicazione dei sistemi di accumulo di energia a batteria (BESS) per fornire servizi ausiliari, in particolare per migliorare l'inerzia della rete. Il lavoro esplora nuove tecnologie di inverter per la formazione della rete che consentono a BESS di emulare la risposta inerziale dei generatori sincroni convenzionali. La tesi adotta un approccio globale, a partire dall'esame del ruolo dei BESS nei servizi ancillari, evidenziandone la rapidità di risposta e la versatilità. Si procede all'analisi di diversi metodi di controllo della formazione della griglia, concentrandosi sugli approcci Virtual Synchronous Machine (VSM), Generalized Virtual Synchronous Generator (GVSG) e Compensated Generalized Virtual Synchronous Generator (CGVSG). La struttura di controllo è definita per includere il regolatore di tensione esterno e il regolatore di corrente interno per evitare errori di stato stazionario e introdurre strategie di limitazione della corrente. Viene aggiunta un'impedenza virtuale per ottenere un flusso di potenza attivo e reattivo disaccoppiato. L'obiettivo principale della metodologia è quello di modellare e mettere a punto i blocchi VSM, GVSG e CGVSG per ottenere una risposta inerziale costante con una buona dinamica. Vengono eseguite simulazioni dinamiche utilizzando Simulink, valutando la risposta di questi sistemi alle perturbazioni di frequenza e alle variazioni del setpoint di potenza. Inoltre, viene studiata l'efficacia della variazione del rapporto di corto circuito (SCR) sulla dinamica di questi sistemi per esaminare quanto preservino la loro risposta.

I risultati della ricerca rivelano che specifici metodi di controllo della formazione della griglia, vale a dire il VSM e il GVSG compensato, forniscono efficacemente una risposta inerziale costante, offrono una buona risposta ai transienti e mantengono relativamente le dinamiche di risposta con le regolazioni SCR. Lo studio dimostra come questi sistemi possano offrire supporto alla rete, garantendo operazioni di rete più stabili e affidabili, in particolare nelle aree con un'elevata penetrazione di energia rinnovabile.

Parole chiave: BESS, inerzia, rapporto di cortocircuito, VSM, GVSG, CGVSG

Contents

Introduction

In recent years, the renewable energy generation started to rise dramatically for most countries. In Europe, following the introduction of the renewable energy directive 2009/28/EC, the region increased the share of renewable energies in energy consumption to 20% by 2020, according to Eurostat [1]. Out of such energy consumption, 23% was consumed by the electricity sector as the second highest source of energy consumption [1]. Nevertheless, renewable energy generation is expected to continue rising in the coming years as part of the decarbonization plan. The directive EU/2018/2001 has set the renewable energy target to reach 32% by the year 2030 [2]. Subsequently, a provisional agreement was accepted to raise that target to at least 42.5%, with an aim for 45% [2]. The Continuous rise of renewable generation in the electricity sector can cause some problems for the grid, which need to be addressed.

In traditional power systems, the synchronous generator is the main source offering support to the grid through its kinetic energy and governor control. The synchronous machine has the capability to participate in the primary frequency control using the governor speed control mechanism and dampen the system dynamics through its inertia. However, the power converters connecting renewables with the grid do not possess such capabilities. In fact, their control structure is more focused on extracting the maximum power from the renewable source. With the growth of renewable energy sources, the use of synchronous machines is expected to decline, hence decreasing the system inertia and support [3]. Remarkable efforts are focused on developing a control approach that allows power converters to mimic the behavior of a synchronous machine. A captivating control family has emerged, called 'Grid-forming Inverters,' allowing the inverters to provide some of the synchronous machine functionalities like primary frequency control, oscillation damping, and contributing to system inertia. This control methodology is best suited to be implemented with batteries. The high ramp rate along with power and energy characteristics of batteries ensures compliance with the control output power signals. The grid-forming presents multiple control approaches [10], with the utmost attention focused on the so called "Virtual Synchronous Machine". It directs the power converters to act in a similar manner to a synchronous generator, thus providing all its functions mentioned above. A novel

approach called "Generalized Virtual Synchronous Generator" was developed to tackle the main problems associated with the VSM [4].

This thesis is focused on the investigation of different grid-forming technologies. Following that, the most suitable grid-forming topologies for inertia provision will be chosen for further analysis to determine the most suitable technology for the thesis application.

This thesis starts by introducing the importance of using batteries in ancillary service market. Then, the grid-following and grid-forming control methods are compared for usage with batteries. A detailed investigation is carried out for the various grid-forming control structures found in the literature to select the most suitable ones for inertia supervision.

In the second chapter, the complete control structure for the selected control topologies is revealed. The case study is presented with the circuit schematic of the system. In the last section of the chapter, the modelling and tuning of all controllers found in the control structure is performed along with the active and reactive power controllers of the virtual synchronous machine. The tuning of the VSM is focused on obtaining a constant inertial response along with a good dynamic behaviour.

In the third chapter, the dynamic model implemented in Simulink is presented. The performance of the VSM is analysed thorough three main tests that focuses on applying frequency and power setpoint perturbations. The aim of this chapter is to examine the dynamic behaviour of VSM, and the inertial response supplied during frequency changes.

In the fourth chapter, new control methods developed from VSM were introduced called GVSG and CGVSG. The tuning of inner and outer controllers is adapted from VSM in chapter two. The tuning and modelling of inertia block for both methods was carried out to achieve a similar constant inertial response of the VSM and have a dynamic response that is fast and provide low overshoot.

In the fifth chapter, the GVSG and CGVSG dynamic performance was tested with the same tests defined in chapter three. At the end of the chapter, a comparison is conducted between the reference control topologies for identifying the best control method for implementation in inertia supervision.

1 Battery Energy Storage System for Ancillary Services

Ancillary services in the context of power systems refer to services that provide support for the transmission of electricity from producers to customers, ensuring the security and reliability of the grid. The services in this market are mainly focused on providing frequency regulation, voltage regulation, spinning reserves, and black start potential, among other services. Batteries, especially modern advanced ones like lithium-ion have been excellent contenders for the Ancillary services market for multiple reasons:

- Fast Response Time: Batteries have very fast response times compared to conventional synchronous generators. This rapid response can be very beneficial for frequency regulation services for correcting discrepancies in demand and supply. In fact, because of such a fast response, regulators can introduce new frequency regulation services that are stricter in their response time.

- Versatility: Batteries can both absorb and release energy. Such capability can allow for the introduction of asymmetry of service in the ancillary market. (complete this)

- Reduced Wear on Conventional Generator: Continuously adjusting the output of synchronous generators for ancillary services can lead to more tear and wear of these units. Batteries can take responsibility for such services, ensuring operational longevity for generators.

The usage of batteries has been increasing in Ancillary service markets, especially after some modifications that were done in the market by different regulators due to the continuous increase in renewable energies, hence more requirements in terms of the grid needs for security.

1.1. Frequency Regulation

The frequency regulation service is mainly focused on adjusting the output of systems connected to the grid based on the grid's needs. The aim is to maintain the frequency within specified ranges. There are multiple services in the frequency regulation market including:

- **Primary Frequency Regulation:**

  The purpose of primary frequency control is to eliminate any changes in frequency, hence preserving a constant frequency. This goal can be achieved by balancing the supply and demand response. It is mandatory for all generators connected to the grid to participate in this service for a duration ranging from 20 to 30 seconds. The Implementation of the control structure is based on governor control as shown in Fig.1.1, where a change in frequency is transformed into an equivalent change in output power based on a factor called the "Droop Coefficient". Batteries can also provide primary frequency regulation due to their rapid response.
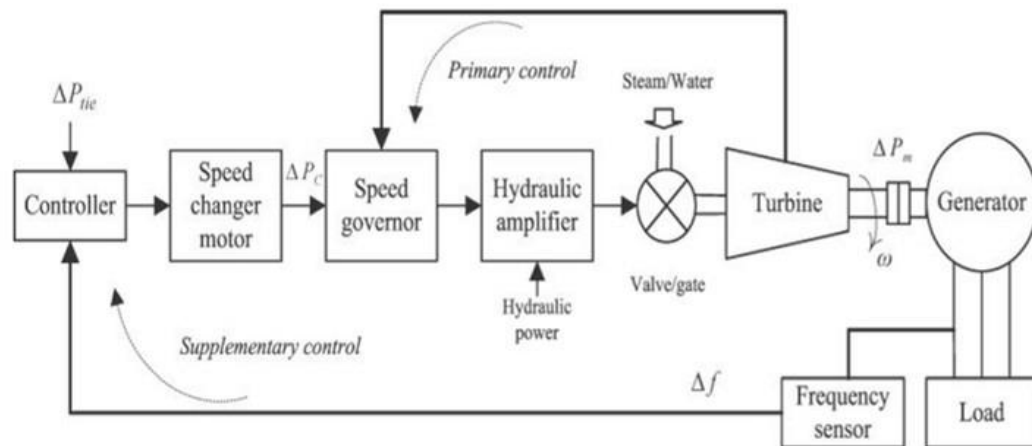

Figure 1.1. Governor control for primary frequency regulation

- **Secondary Frequency Regulation:**

  The secondary frequency control works to restore the frequency to its nominal value. It involves automatic adjustments to generation, usually through a centralized control system in a duration between 5 to 10 mins. Batteries can participate in this process by receiving signals from the grid operator to adjust their output with the help of modern inverter technologies.

- **Tertiary Frequency Regulation:**

   It restores the system's reserves to a desired state after they participate in primary and secondary frequency regulation. For this reason, the duration of this service is long, taking more than 30 mins for execution. The following Figure summarizes the characteristics of the previous frequency regulation services.
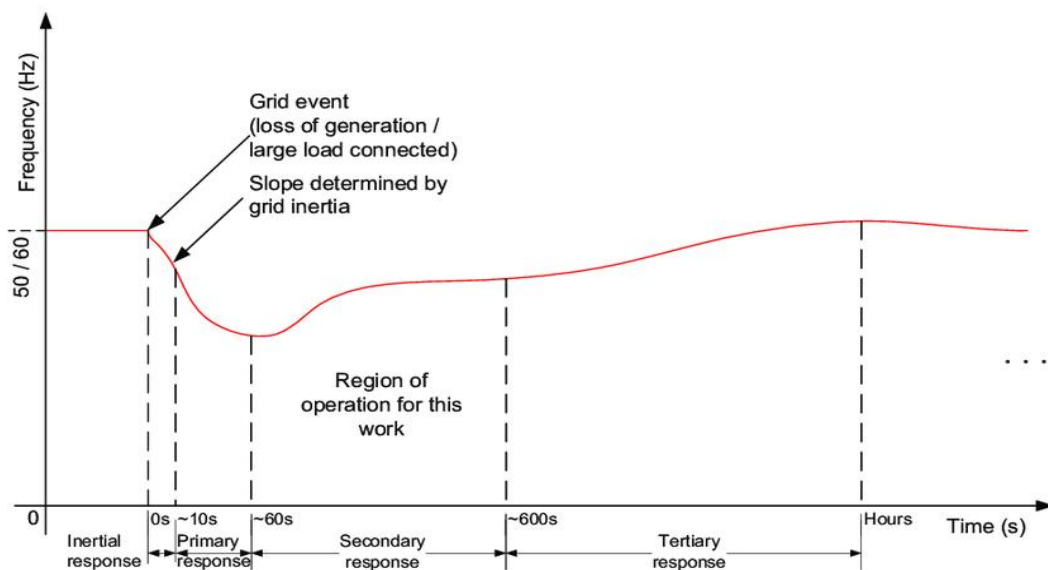

Figure 1.2 Duration required by different frequency regulation services.

- **Fast Frequency Response (FFR):**

   The fast-frequency response market is designed to handle sudden and significant changes in generation, especially in grids with high penetration of renewables. Batteries are the most suitable technology for this market because of their capability to react to deviations within milliseconds. Batteries have ramp rates much higher than conventional units. An evaluation for such characteristics was done by [5], evaluating 1 MW of fast-frequency response equivalent to 20 MW of conventional response.

- **Inertial Response:**

   With the increase of renewable energy, conventional synchronous generators that provide inertia are declining. Some advanced battery systems can emulate

inertia, through modern inverter control structures, to improve system inertia and resist sudden changes in frequency.

In Europe, several regulators have recognized the importance of enhancing ancillary services to keep up with grid requirements with the continuous rise of renewable generation. Various European markets have already implemented the fast frequency response including Great Britain, Ireland, and Finland, while other countries are evaluating the feasibility and necessity of introducing FFR services. On the other hand, for the inertial response market, discussions are still in progress for the needs of this market without any real implementation.

1.2.   Inertial Ancillary Market

Inertia response is linked to large rotating generators providing part of their rotational mechanical energy to counter changes in frequency, thus reducing ROCOF and frequency nadir. The inertia of the system is continuously decreasing as a result of replacing traditional synchronous machines with renewable energy sources. The inertia response can be emulated through modern inverter technologies known as "Grid-forming". Batteries are best suited for this technology because of their electrochemical energy that can be rapidly extracted using an inverter. The remuneration for providing inertia is usually set through regulations.

Regulators are trying to introduce new grid services in response to the decrease in inertia such as fast-acting ancillary services. The current regulatory framework only supports inertia during critical levels when the inertia fall has already taken place. It does not support inertia during normal operating conditions. Also, it doesn't include transparent pricing signals. One of the proposed services to be implemented in the future is a market for Inertia. In fact, Australia tried proposing an inertia spot market option in [6] that is consistent with the existing market design principles. The inertia spot market introduces three types of service providers according to the following bid types:

Energy-only: the service provider is not able to provide inertia in that case, thus it is associated with zero inertia (0 MWs) in its bid. Offers of this type will continue to be treated as they are in the current energy market.

Inertia and energy: the service provider can only provide inertia when it is generating power at a minimum level, doing so includes a positive energy margin that can be utilized to dispense inertia.

Inertia-only: the service provider can provide inertia without any energy output (0 MW). This includes the willingness of the service provider to work in Synchronous Condenser mode.

After the assessment of the proposal of introducing Inertia as an ancillary service, the offer was rejected for further assessment as well as the absence of strong necessity for such service. However, it is expected that with the further decline in system inertia, the inertia ancillary market might be repurposed and developed in the future.

1.3. Power Converters for BESS Control

The response of a battery is controlled to obtain a specific output using inverters. Depending on the type of inverter, the battery will respond in a specific way corresponding to a certain requirement or function implemented by the inverter. The classification of inverters used for battery control can be divided into two categories: Grid-following Inverters and grid-forming Inverters.

1.3.1. Grid-following Inverters

A grid-following Inverter can be deployed for multiple objectives. The most common implementations for grid-following inverters are Maximum Power Point Tracking and frequency regulations. The MPPT is normally set as an objective in the case of renewable energy applications. In that case, we aim to extract the maximum energy possible from the renewable energy source using a grid-following inverter. Grid-following inverters can also perform very well in frequency regulation services due to their fast response. This type of inverter responds faster compared to grid-forming because of its control structure, making it a more attractive solution for fast-acting ancillary services.
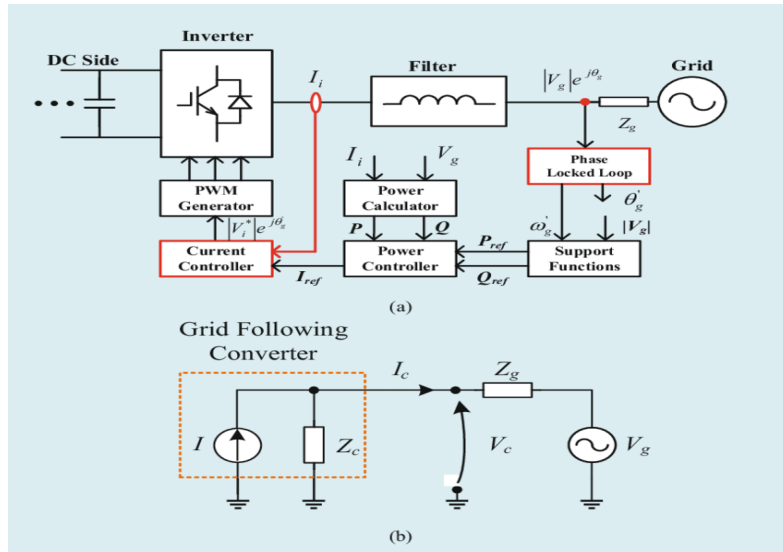
Figure 1.3 General control scheme of grid-following inverters.

The principle of operation for grid-following inverters can be described in Fig.1.3. The support Function block implements the objective of the grid-following control such as MPPT, primary frequency regulation, and fast frequency response. The output from this block is an active power and reactive power signals. These signals are forwarded to a power controller that is asked to calculate a current reference signal in terms of magnitude and phase. Finally, the current reference is sent to the current controller to control the current into the desired reference value. Usually, the current controller has a very fast response ranging from $0.5 - 5$ ms [16].

For synchronizing the grid-following inverter to the grid, a phase locked loop is used that measures the angle of grid voltage. It is important to note that this grid voltage angle, obtained by PLL, acts as a reference for controlling the output current angle. For further elaboration, imagine that the grid-following inverter is controlled to only generate active power output (zero reactive power signal). In this case, the current will be controlled to be in phase with the angle obtained from the phase locked loop (Grid voltage angle), thus from (1.1) and (1.2), $\emptyset$ will be zero injecting only active power into the grid.

$$P = VI \cos \emptyset, \qquad \emptyset = \theta_v - \theta_i \qquad (1.1)$$

$$Q = VI \sin \emptyset \qquad (1.2)$$

Due to the control structure of the grid-following inverters, the equivalent circuit diagram can be represented like [7] as shown in Fig.1.4(a). The grid-following inverter

can be represented as a constant current source connected to a parallel impedance. Because of this behavior, when the grid voltage is subjected to perturbations, the inverter tries to maintain the current value resulting in a change in the converter voltage as shown in Fig.1.4(b). The current reference will only change after the PLL measures the new grid voltage angle. Hence, the grid-following inverter does not support the grid since it does not resist any changes in its voltage magnitude and phase following a perturbation. Moreover, it cannot react instantaneously to grid changes.
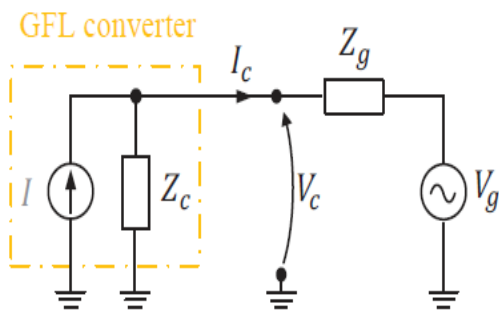
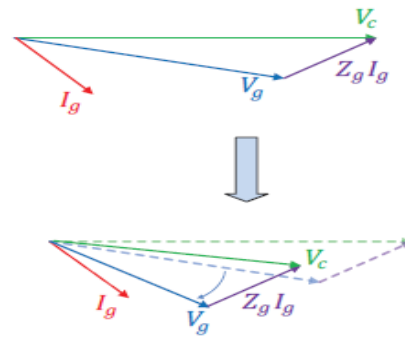

Figure 1.4(a). GFL circuit diagram.

Figure 1.4(b). GFL behavior during grid perturbations

Even though grid-following inverters can be used in frequency regulation services, most of them cannot support the grid in terms of inertia response. Moreover, they run into stability issues during weak grid conditions. To address this issue, the so-called grid-forming inverters have emerged, gaining a lot of research interest in recent years.

1.3.2. Grid-forming Inverters

Grid-forming inverters have gained lots of interest in the past years due to their ability to support the grid. With the continuous rise of renewable energy, grid-forming can tackle the issues related to this increase. The purpose of GFM is to support the grid in terms of frequency regulation as well as inertia. GFM can react instantaneously to grid perturbations faster than GFL as shown in Fig.1.5. In Fig.1.5, the active power change for both multiple GFM and GFL inverters was recorded for a change in grid phase angle.
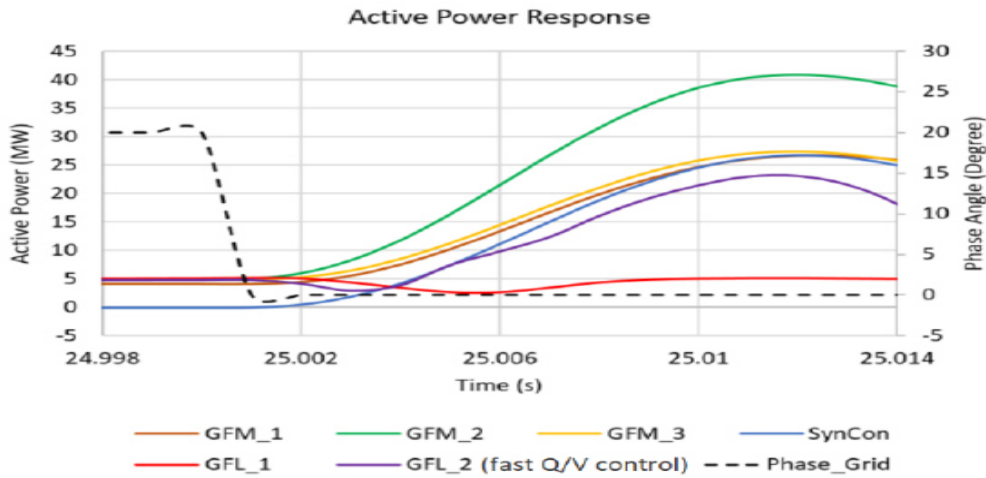
Figure 1.5. Comparison between the reaction of GFM and GFL to grid disturbance [8]

The GFM inverters react almost instantaneously to this change within 2 ms [8]. However, GFL inverters have some changes in their active power measurements due to the PLL dynamics, then they start reacting to support the grid within 4 ms. This feature can be very useful, especially in systems with low inertia, where speed of reaction to perturbations matters. Moreover, synchronization is achieved in GFM inverters like synchronous machines, where a GFM inverter matches power system parameters like voltage magnitude, phase angle, and frequency. In case a disturbance happens to any of these parameters, the power flow from the inverter will change to match these parameters and keep synchronization with the power system. Thus, the GFM inverter doesn't face instability problems during weak grid conditions and there is no need to use PLL for synchronization in this case.

The general control structure of GFM inverters can be represented by Fig.1.6. This control structure is the simplest topology and is usually implemented when the control system of the VSG block is very complex. The general idea here is that we obtain active and reactive power measurements that we then send to the VSM or VSG block. The representation of this VSG block is different for each GFM class. However, the output of this block, for all categories of GFM, is a voltage magnitude signal with speed and phase angle. After that, these signals can be used to calculate the modulation index for the operation of pulse width modulation.

Because of such a structure, the circuit diagram of the GFM inverter can be shown in Fig.1.7a [7]. A GFM can be represented by a constant voltage source with a series impedance. This portrayal allows the inverter to maintain its voltage during grid changes. Fig.1.7b [7] explains the behavior of the inverter after changing the grid voltage magnitude and phase. The inverter reacts by maintaining its voltage, enabling grid support in terms of voltage and frequency. In that case, the current is the changing variable, which might cause some issues for the inverter. The magnitude of this current cannot exceed the IGBT ratings of the inverter. Consequently, the control topology of Fig1.6 isn't the most suitable way to present the GFM inverter since it doesn't allow for overcurrent protection.
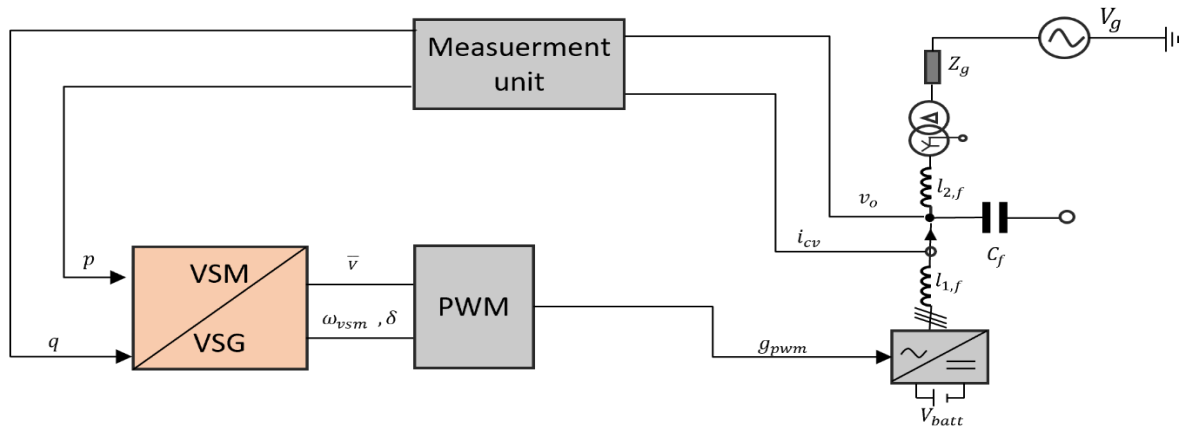
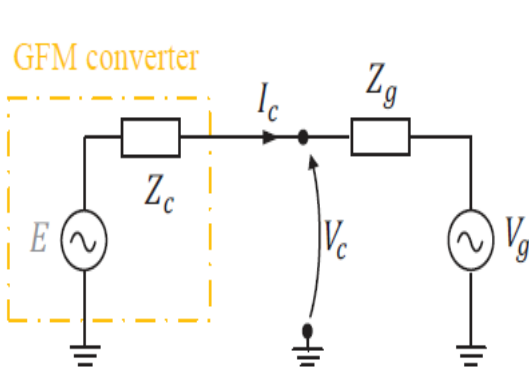Figure 1.6. General control schematic of GFM inverters.

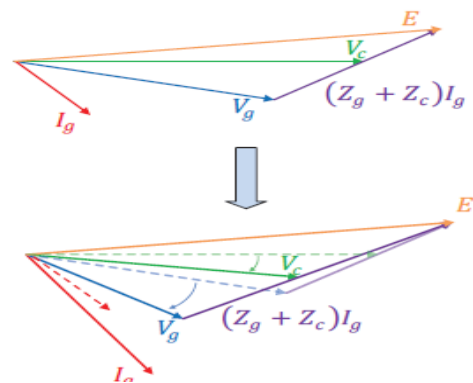Figure 1.7(a). GFM circuit diagram

Figure 1.7(b). GFM behavior during grid perturbations

 As a result, the control structure was developed to include an outer voltage controller and an inner current controller as shown in Fig1.8. The purpose of the voltage controller is to remove any steady-state errors in following the voltage references from

the VSG block, while the current controller objective is to control current, allowing for the implementation of current limiting strategies. The current limitation saturates the current reference signal from the voltage controller in case the current exceeds inverter ratings, then the current controller saturates the current by following the new saturated current reference signals. Furthermore, the virtual impedance decouples the dynamics between active and reactive power as they have separate control, relating voltage magnitude with reactive power flow and phase angle with active power flow [9]. This advanced control structure is applicable only to certain types of GFM inverters as using extra inner current and outer voltage controllers is not possible for all GFM inverters, which will be shown later.

GFM inverters can be classified into two main categories [10] according to the structure of the VSG block in Fig.1.6 or Fig.1.8. The two categories are droop and virtual synchronous machines. More clarifications are going to be made in the next section, classifying different GFM types for each of the two mentioned categories and pointing out which control structure Figure (Fig.1.8 or Fig.1.6) is used for each GFM type.
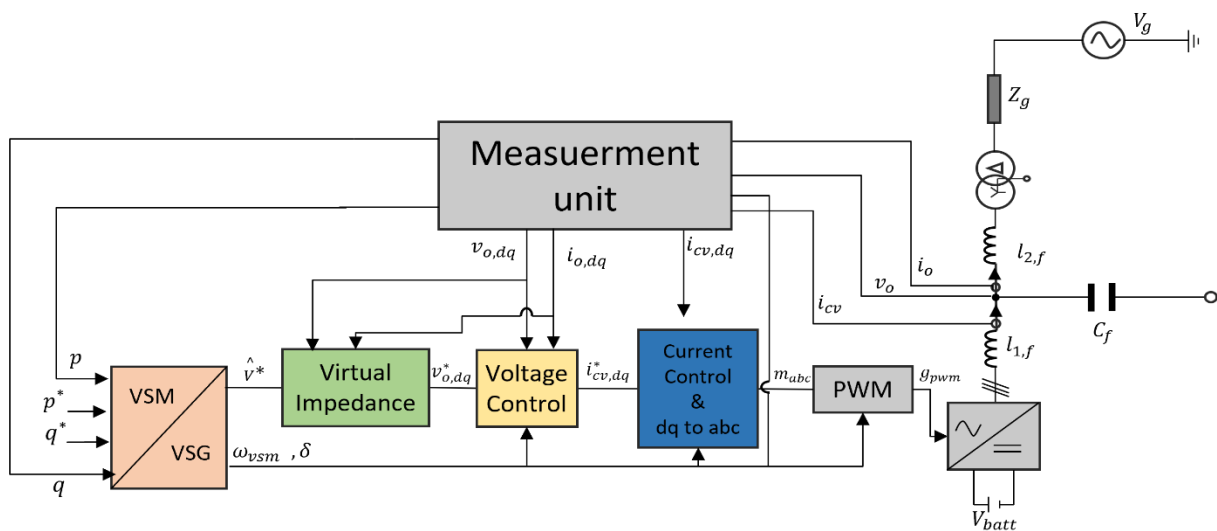

Figure 1.8. Advanced control schematic for GFM inverters

1.3.2.1. Droop

Droop control is the simplest and most common GFM category. It sets the inverter to work like droop control that is performed by the governor in the case of synchronous generators. The most common type of droop is the direct droop shown in Fig.1.9. To avoid confusion, it is important to note that Fig.1.9 represents the

diagram of the VSG block that was shown in Figures 1.6 and 1.8 before. However, the complete control diagram of the direct droop can be represented by Fig.1.8 because of its simple implementation of the VSG block as discussed before. Thus, the outer voltage controller and the inner current controller can be used with the direct droop for accuracy and current protection. In fact, these cascaded controllers can be used for all droop control types as they all have simple control structures.
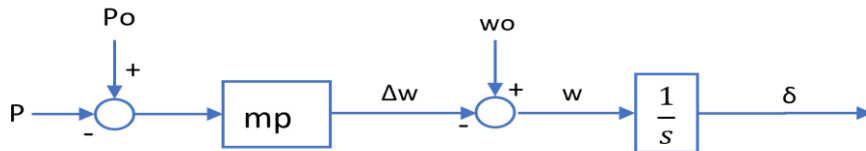

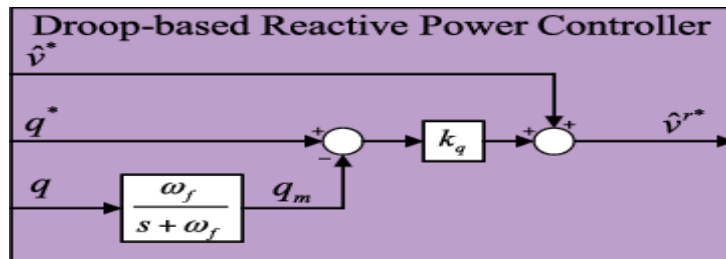Figure 1.9. Active power droop control block diagram

Figure 1.10. Reactive power droop control block diagram

The coefficient m_P shown in Figure 1.9 is the droop gain. It is usually set according to regulations ranging from 3 to 5% [11]. A change between the power measured and the power setpoint corresponds to a change in frequency through that droop gain. A high droop gain allows for better power sharing, but it leads to high power dynamics that can lead to instability. w_0 is a constant reference frequency. The control of reactive power is also droop-based in the direct droop as shown in Figure 1.10. A filter is added to reactive power measurements to remove harmonics. This droop-based reactive power controller is used for most GFM types that will be mentioned next so only active power control diagrams will be represented to avoid repetition. Both Figures 1.9 and 1.10 together represent the full diagram of the VSG block in Figure 1.8 where reactive power droop specifies voltage magnitude and active power specifies the phase angle.

Due to issues associated with high droop gains, the angle-based droop was developed in [12] to improve the transient response. The block diagram is presented in Fig. 1.11. The main difference here between direct droop and angle-based droop is that the reference angle used in the latter isn't obtained from a constant reference

frequency similar to the direct droop, but it is measured from an external source with a real-time measurement. Because of that, setting high droop gain is not a problem in angle-based droop and no power oscillations will occur.
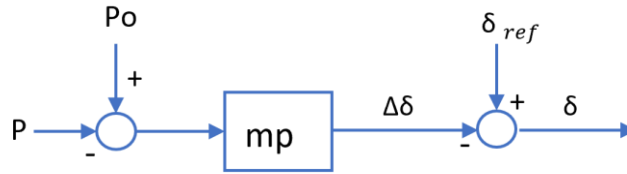

Figure 1.11. Angle-based droop block diagram

The main issue with the droop category is the absence of inertial response. Changes in power happen instantaneously, failing to provide inertia and resisting changes in frequency. However, it was proven by [13] that adding a filter to the active power measurement, like in Fig. 1.12, will correspond to a swing equation emulation. (1.3) shows the time constant and drag coefficient obtained by the droop in that case, where the time constant reflects the inertial response. Tuning both the time constant and drag coefficient for such a case is difficult since both of them are correlated by the droop gain.
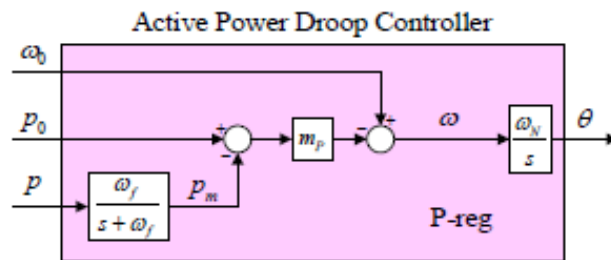

Figure 1.12. Active power droop with a filter block diagram

$$T_a \frac{d\omega}{dt} = P_0 - P - k_d(\omega - \omega_g)$$

$$T_a = \frac{1}{\omega_f \cdot m_p} \qquad\qquad K_d = \frac{1}{m_p}$$

(1.3)

1.3.2.2. Virtual Synchronous Generators

Unlike the droop category, VSG can easily be tuned to provide a specific inertial response due to its control structure. Virtual synchronous machines are modeled to emulate the behavior of synchronous generators. There are three main GFM types that can be included in this VSG category. The first two are VISMA and synchronverter [14] shown in Figures 1.13 and 1.14. The VISMA models the inverter as an electromechanical machine representing both its static and dynamic properties. The representation of such a model is very complex; thus, it can't use cascaded controllers. There are two options included in the implementation of the VISMA model. The first is to have an output current that is directed then to a hysteresis control. The hysteresis control causes lots of harmonics, which is not preferred. The second option is an output voltage signal with a pulse width modulation, which is better than the latter.

Synchronverters model inverters as a synchronous generator representing the dynamics from a grid point of view. Similar to VISMA, synchronverters don't have cascade controller due to their complexity. Hence, also synchronverters have their output directly sent to pulse width modulation and the complete control structure for both models (VISMA and synchronverters) can be presented in Figure 6. It can be noted that the active and reactive power controls are already coupled in these models and no droop-based reactive power controller is used. The overcurrent protection in these models is difficult to obtain in the control structure itself since they have no current controller. The protection is achieved either in the physical circuit or by another control block that overrides the response of the VSG block.
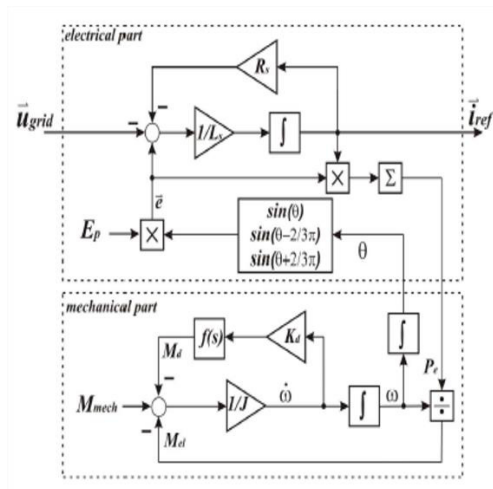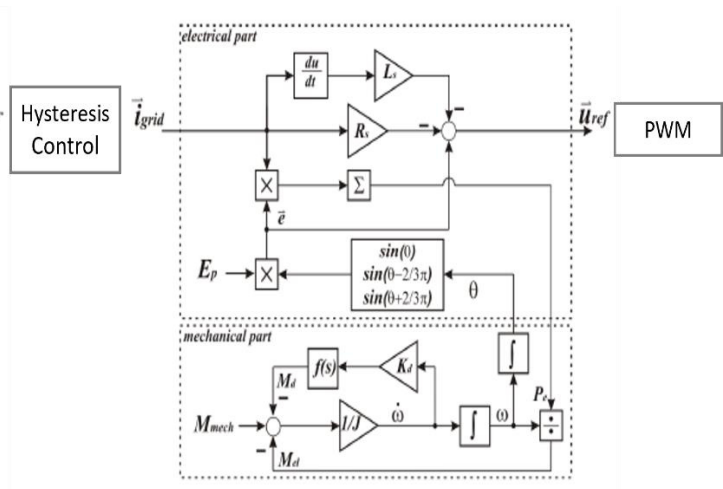

Figure 1.13(a). VISMA model type 1
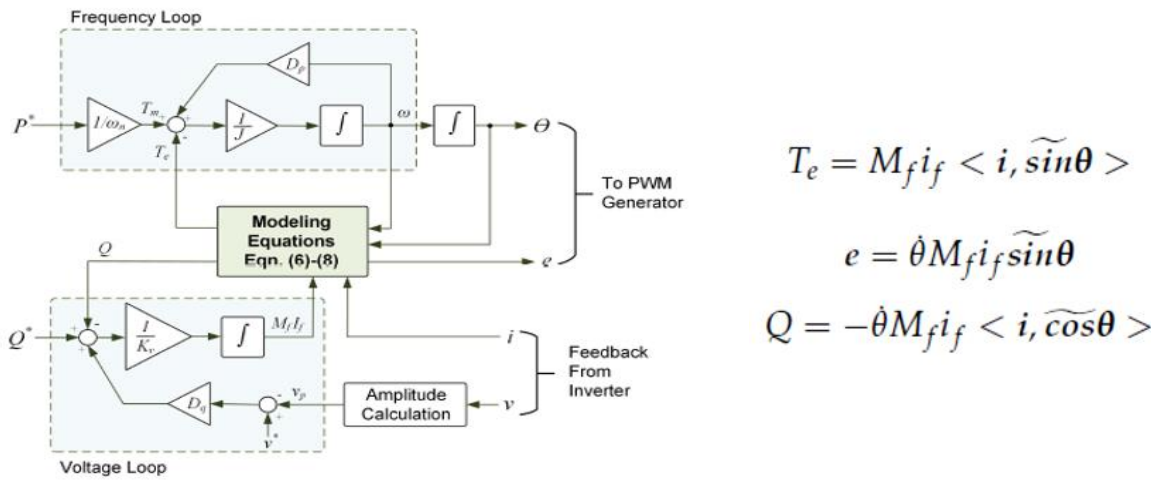
Figure 1.13(b). VISMA model type 2

Figure 1.14. Synchronverter block diagram

The third type is the swing equation emulation, which is also called a virtual synchronous machine. The VSM models an inverter to behave like a 2nd order model of a synchronous generator. Hence, the inverter is modeled to act based on the swing equation of a synchronous machine. This model is simpler compared to the other two leading to its ability to include cascaded controllers within its model. The block diagram of the Virtual Synchronous Machine can be shown in Figure 1.15, while the complete model can be represented in Figure 1.8. A decoupled droop-based reactive power controller is included in the VSG block along with the active power controller shown in Figure 1.15 in that case. The time constant T_a is tuned to obtain the desired inertial response while the drag coefficient K_d is responsible for the dynamic response. Hence, The VSM is characterized by its capability to independently tune both dynamic and inertial behavior, unlike the droop.

The representation of the drag coefficient differs according to the reference grid frequency used. There are three options for the reference frequency: fixed grid frequency, estimated grid frequency using PLL, and internal estimation of grid frequency. A fixed grid frequency turns the drag coefficient into the droop gain. In that case, we are constrained by regulations, and it is difficult to choose a high drag coefficient to dampen the dynamics. An estimated grid frequency solves that problem by allowing the choice of higher drag coefficients with complete freedom in the tuning, considering the stability of the system. An internal estimated grid frequency works in

a similar way as the latter. However, it introduces some time delay to the grid frequency that can affect the inertial response.
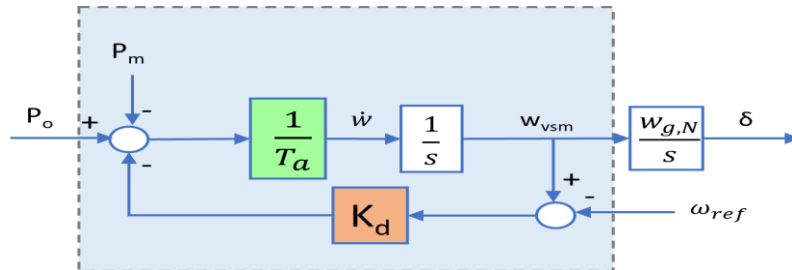

Figure 1.15. Virtual synchronous machine block diagram.

A more advanced control topology has been developed recently, evolved from the virtual synchronous machine, called Generalized Virtual Synchronous Generator. It uses the fixed grid frequency; the drag coefficient is limited by droop gain in that case. An extra zero and pole are placed in the block diagram of the Virtual Synchronous Machine along with the time constant. These extra zero and pole are tuned to obtain a stable and damped response, which is difficult to achieve using only the droop gain. This GVSG model was further developed into a Compensated Generalized Virtual Synchronous Generator, where the extra zero was moved into the feedback path of active power. This extra zero is responsible for further damping of the system to eliminate any overshoot.

According to the previous information concerning different types of grid-forming inverters, the most suitable technologies for inertial supervision applications are VSM, GVSG, and CGVSG due to the possibility of using cascaded controllers, providing inertial response, and independent tuning of inertial and dynamic behavior. These technologies are chosen for a more detailed analysis that includes modeling, tuning, and testing of these inverters to identify the best grid-forming methodology for the application of this thesis.

2   Analysis of Control System

In this chapter, the study case will be introduced along with the grid-forming topologies that we are interested in further analysis. The converter's schematics as well as the control system diagram will be explained. Then, the design of virtual synchronous machine control blocks will be explained in detail.

2.1. Structure of Case Study

The structure of the case study to be analysed is adapted from project CBESS- 2000, that is developed by NHOA Energy. The system rated power is 2 MVA and is provided through two inverters. Each inverter is rated at 1 MVA.
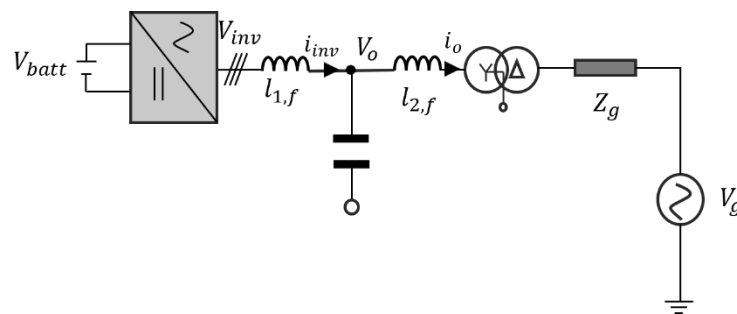

Figure 2.1. Single line diagram of the case under study

For simplicity, only one inverter is analysed in the thesis since the aim of the thesis is to investigate the dynamic response of a single inverter, not multiple inverters. The line diagram representing the structure of a single inverter system is shown in Figure 2.1. The system consists of a battery that is connected to an inverter. The inverter will be controlled by one of the grid-forming topologies mentioned in the literature according to the thesis objectives that will be mentioned soon. The inverter is then

connected to an LCL filter and then to a transformer that connects the system to the grid.

The inverter model used is a two-level voltage source converter. A PWM is used to ensure a perfect sinusoidal response with low THD. The switching frequency is 3 kHz. The LCL filter is designed to act as a low-pass filter, eliminating all the higher-order harmonics. The following Table summarizes the values of the model parameters.

Table 2-1. Parameters of elements used in the circuit diagram.

Parameter		Value
Rated primary Voltage	V_n [V]	690
Rated Secondary Voltage	V_S [kV]	15
Battery Nominal Voltage	V_{batt} [V]	1300
Rated Apparent Power	S_n [MVA]	1
Rated Angular Frequency	W_b [rad/s]	314.16
Short circuit ratio	SCR	10
Grid Inductance	L_g [H]	0.0356
Grid Resistance	R_g [ohm]	1.1194
Filter Inductance 1	$L_{1,f}$ [H]	$1000*10^{-6}$
Filter Inductance 2	$L_{2,f}$ [H]	$4*10^{-6}$
Filter Capacitance	C_f [F]	$960*10^{-6}$
Transformer Short Circuit reactance	x_T [pu]	0.06
Transformer Copper losses	r_T [pu]	0.003

This thesis focuses on the detailed analysis of the most suitable grid-forming structures found in the literature. The choice of grid-forming topologies for this study is based on the objectives of the application, which are:

- Determining a constant inertial response for a given rate of change of frequency (ROCOF)
- Obtaining a good transient response in terms of rise time and overshoot.

- Preserving response dynamics as much as possible with the variation of short circuit ratio.

These objectives align with the selected control methods at the end of Chapter 1, which are VSM, GVSG, and CGVSG, and give more validation for the choice of these control structures.

2.2. Control Approach

The selected control methods will be implemented with the following control blocks: Virtual Impedance, Outer Voltage Controller, and Inner current Controller [20]. Figure 2.2 represents the complete control structure of the inverter. The only difference between the three selected control topologies will be in the inertia emulation block, thus the same control approach is used for the design of inner and outer loop controllers. Also, A PLL is used only in the case of VSM. Although The GVSG and CGVSG do not have PLL in their control system [4], it will be explained that under specific conditions, we can use a PLL for GVSG.
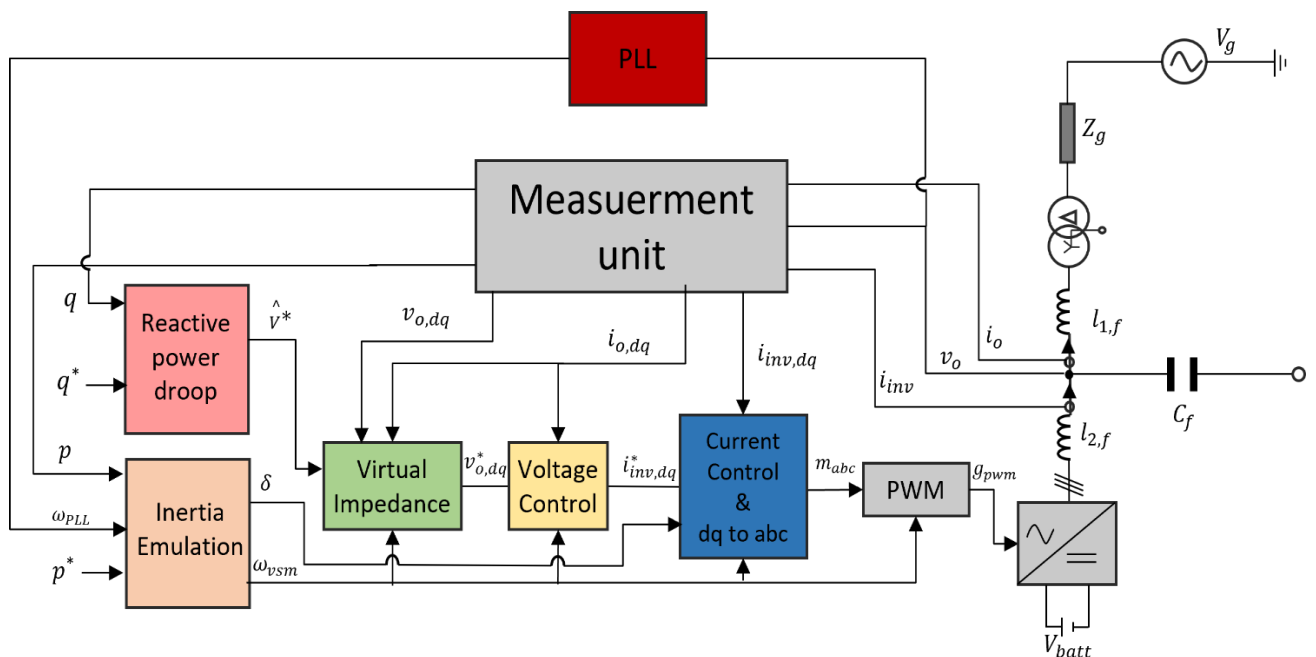

Figure 2.2. Complete control model for VSM

In this model, the inner current controller and outer voltage controller are applied as cascaded controllers. Using cascaded controllers ensures minimizing the effect of disturbances and allows for a better reference signal following. Because of the way a

grid-forming inverter behaves, offering support for the grid, the current value can increase drastically. This can be dangerous for the IGBTs used in the inverter and can damage them. Having cascaded controllers permits controlling the current, hence a current limiting strategy is applicable in this case. The current limitation will override the signal coming from the voltage controller, if they are higher than IGBT ratings, saturating this signal accordingly. After the saturation, the current controller works to control the physical current concerning the saturated signal, ensuring the saturation of the inverter current. The design of cascaded controllers is based on obtaining zero steady-state error, a high bandwidth, and a good dynamic response.

To design the controllers, it is essential to first model the physical circuit equations to identify the control variables, disturbances, and system transfer functions. The system equations can be derived from the line diagram of Figure 2.1 accordingly:

$$\bar{v}_{inv_{abc}} = \bar{v}_{o_{abc}} + \bar{\imath}_{inv_{abc}} \cdot r_{1,f} + \frac{l_{1,f}}{\omega_b} \cdot \frac{d\bar{\imath}_{inv_{abc}}}{dt}$$

$$\bar{v}_{o_{abc}} = \bar{v}_{g_{abc}} + \bar{\imath}_{o_{abc}} \cdot r_{2,f} + \frac{l_{2,f}}{\omega_b} \cdot \frac{d\bar{\imath}_{o_{abc}}}{dt} + r_T \cdot \bar{\imath}_{o_{abc}} + \frac{l_T}{\omega_b} \cdot \frac{d\bar{\imath}_{o_{abc}}}{dt} + r_g \cdot \bar{\imath}_{o_{abc}} + \frac{l_g}{\omega_b} \cdot \frac{d\bar{\imath}_{o_{abc}}}{dt}$$

$$\bar{\imath}_{inv_{abc}} = \bar{\imath}_{c_{abc}} + \bar{\imath}_{o_{abc}}$$

$$\bar{\imath}_{c_{abc}} = \frac{c_f}{\omega_b} \frac{d\bar{v}_{o_{abc}}}{dt}$$

(2.1)

These equations are written in the three-phase reference frame (abc frame) and in per unit since a transformer is present. For simplifying the control, the variables are referred to another reference frame:

- Constant reference frame: the alpha-beta reference frame is a constant frame, therefore variables referred to this reference frame are alternating. In other words, three-phase signals are viewed as AC signals from this reference frame point of view. This prohibits the usage of PI controllers since the reference signals will be continuously changing. PI controllers can only be utilized with a very high bandwidth in this matter. Hence, using PR controllers is more suitable for this reference frame.

- Rotating reference frame: the direct-quadrature reference frame is a reference frame that rotates with a specific frequency. This reference frame is designed to rotate with the same frequency as the three-phase signals. In that case, the three-phase signals can be viewed as constant signals from this reference frame point of view. This allows running PI controllers without any issues.

The reference frame chosen for this model is the dq frame. The system equations are rewritten in this frame as follows:

$$
\left.
\begin{aligned}
v_{inv_d} &= v_{o_d} + i_{inv_d} \cdot r_{1,f} + \frac{l_{1,f}}{\omega_b} \cdot \frac{di_{inv_d}}{dt} - \omega_{vsm} \cdot l_{1,f} \cdot i_{inv_q} \\[2mm]
v_{inv_q} &= v_{o_q} + i_{inv_q} \cdot r_{1,f} + \frac{l_{1,f}}{\omega_b} \cdot \frac{di_{inv_q}}{dt} + \omega_{vsm} \cdot l_{1,f} \cdot i_{inv_d}
\end{aligned}
\right\} \quad \text{Inverter Voltage} \qquad (2.2)
$$

$$
\left.
\begin{aligned}
v_{o_d} &= v_{g_d} + i_{o_d} \cdot r_{2,f} + \frac{l_{2,f}}{\omega_b} \cdot \frac{di_{o_d}}{dt} - \omega_{vsm} \cdot l_{2,f} \cdot i_{o_q} + i_{o_d} \cdot r_T + \frac{l_T}{\omega_b} \cdot \frac{di_{o_d}}{dt} - \omega_{vsm} \cdot l_T \cdot i_{o_q} \\[2mm]
&\quad + i_{o_d} \cdot r_g + \frac{l_g}{\omega_b} \cdot \frac{di_{o_d}}{dt} - \omega_{vsm} \cdot l_g \cdot i_{o_q} \\[3mm]
v_{o_q} &= v_{g_q} + i_{o_q} \cdot r_{2,f} + \frac{l_{2,f}}{\omega_b} \cdot \frac{di_{o_q}}{dt} + \omega_{vsm} \cdot l_{2,f} \cdot i_{o_d} + i_{o_q} \cdot r_T + \frac{l_T}{\omega_b} \cdot \frac{di_{o_q}}{dt} + \omega_{vsm} \cdot l_T \cdot i_{o_d} \\[2mm]
&\quad + i_{o_q} \cdot r_g + \frac{l_g}{\omega_b} \cdot \frac{di_{o_q}}{dt} + \omega_{vsm} \cdot l_g \cdot i_{o_d}
\end{aligned}
\right\}
\begin{aligned}
&\text{Capacitor} \\ &\text{Voltage} \\ &(2.3)
\end{aligned}
$$

$$
\left.
\begin{aligned}
i_{inv_d} &= i_{c_d} + i_{o_d} \\
i_{inv_q} &= i_{c_q} + i_{o_q}
\end{aligned}
\right\} \quad \text{Inverter Current} \qquad (2.4)
$$

$$
\left.
\begin{aligned}
i_{c_d} &= \frac{c_f}{\omega_b} \frac{dv_{o_d}}{dt} - \omega_{vsm} \cdot c_f \cdot v_{o_q} \\[2mm]
i_q &= \frac{c_f}{\omega_b} \frac{dv_{o_q}}{dt} + \omega_{vsm} \cdot c_f \cdot v_{o_d}
\end{aligned}
\right\} \quad \text{Capacitor Current} \qquad (2.5)
$$

The variable ω_{vsm} represents the angular speed coming from the inertia emulation block in per unit. The rest of the variables were already defined in Table 2-1 and Figure 2.1. It can be noticed that the dq reference frame introduces some sort of coupling between the direct and quadrature axis equations of inductance and capacitance. Details of transforming equations from three-phase reference frame to dq frame will be exploited during the design of controllers. For simplicity, the dq variables will just be denoted by one variable from now on. For example, capacitor voltage is represented by $v_{o_{dq}}$.

2.3. Virtual Synchronous Machine

In the next sections, the control loops will be designed and tuned, starting from the innermost current controller, then moving outwards to the voltage controller followed by virtual impedance, phase locked loop, and finalizing with inertia emulation and reactive power droop.

2.3.1. Current Controller

The implementation of a current controller is very important since, as mentioned in the previous section, it allows controlling the current when it is saturated. The closed-loop feedback path of the inverter current can be expressed by the block diagram in Figure 2.3. The block diagram mainly consists of three blocks representing the PI controller, PWM, and physical system.
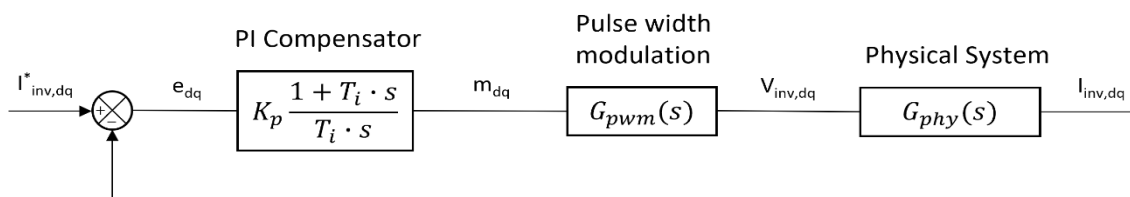

Figure 2.3. Simplified closed loop block diagram of current controller with PWM.

It is essential to identify the system's physical equations for proper identification of the control variables and disturbances. In some cases, a feedforward transfer function is inserted with the disturbance compensation to alleviate the impact of the disturbance on system design. This can only be decided when the detailed block diagram is drawn from the system equations. Moreover, these equations can obtain

the transfer function of the physical system, which is important for obtaining the theoretical current for feedback. The main equation used in the design of the current controller is Kirchoff's voltage law found in equation 2.1, with adapting SI units instead of per unit and the alpha-beta frame instead of three-phase frame.

$$\bar{V}_{inv_{\alpha\beta}} = \bar{V}_{o_{\alpha\beta}} + \bar{I}_{inv_{\alpha\beta}} \cdot R_{1,f} + L_{1,f} \cdot \frac{d\bar{I}_{inv_{\alpha\beta}}}{dt} \tag{2.6}$$

The equation can be referred to the dq rotating reference by transforming from alpha-beta reference frame to the dq frame. This can be done by referring to Figure 2.4. Figure 2.4 shows that for a phase vector V if the vector components are presented in the alpha-beta frame. Then, its components can be transformed from the alpha-beta reference frame through the angle δ, where δ is the angle between the alpha-axis and d-axis, into the dq reference frame as shown in (2.7)
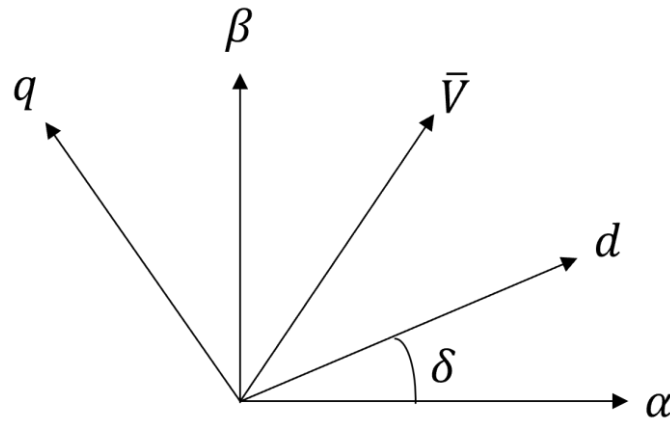
Figure 2.4. Vector diagram defining dq frame and alpha-beta frame.

$$\bar{V}_{\alpha\beta} \cdot e^{j\delta} = \bar{V}_{dq} \tag{2.7}$$

By using (2.7) the phasors of (2.6) that are in alpha-beta frame are substituted with their equivalent of dq frame to give the following

$$V_{inv_{dq}} \cdot e^{j\delta} = V_{o_{dq}} \cdot e^{j\delta} + I_{inv_{dq}} \cdot e^{j\delta} \cdot R_{1,f} + L_{1,f} \cdot \frac{d(I_{inv_{dq}} \cdot e^{j\delta})}{dt} \tag{2.8}$$

Solving the derivative of two multiplied variables with equating $\frac{d\delta}{dt} = w_{vsm}$ introduces the coupling between the direct and quadrature axes.

$$V_{inv_{dq}} = V_{o_{dq}} + I_{inv_{dq}} \cdot R_{1,f} + L_{1,f} \cdot \frac{dI_{inv_{dq}}}{dt} + j \cdot L_{1,f} \cdot W_{vsm} \cdot I_{inv_{dq}} \tag{2.9}$$

Dividing by per unit quantities $V_b = I_b R_b = I_b \omega_b L_b$ the equation can be rewritten in per unit quantities accordingly.

$$v_{inv_{dq}} = v_{o_{dq}} + i_{inv_{dq}} \cdot r_{1,f} + \frac{l_{1,f}}{\omega_b} \cdot \frac{di_{inv_{dq}}}{dt} + j \cdot l_{1,f} \cdot \omega_{vsm} \cdot i_{inv_{dq}} \qquad (2.10)$$

From (2.10), we can identify the state variable, control variable, and disturbances to obtain the physical system transfer function. $i_{inv_{dq}}$ is the state variable, $v_{inv_{dq}}$ is the control variable since it has the modulation index that drives the PWM, $v_{o_{dq}}$ is a disturbance, while the factor $j\omega_{vsm}$ introduces a coupling between the equations of the dq axis. To remove the coupling effect, the choice of the control variable u can be made to include the coupling terms as well as the disturbance terms.

$$u_{dq} = v_{inv_{dq}} - v_{o_{dq}} - j \cdot l_{1,f} \cdot \omega_{vsm} \cdot i_{inv_{dq}} \qquad (2.11)$$

Substituting (2.11) into (2.10), we get (2.12).

$$i_{inv_{dq}} \cdot r_{1,f} + \frac{l_{1,f}}{\omega_b} \cdot \frac{di_{inv_{dq}}}{dt} = u_{dq} \qquad (2.12)$$

Performing Laplace transformation

$$i_{inv_{dq}}(s) \cdot r_{1,f} + \frac{l_{1,f}}{\omega_b} \cdot i_{inv_{dq}}(s) \cdot s = u_{dq}(s) \qquad (2.13)$$

Taking current as a common factor, then rearranging the equation to get the physical system transfer function, relating the inverter current to the control variables u_{dq}.

$$G_{phy}(s) = \frac{i_{inv_{dq}}(s)}{u_{dq}(s)} = \frac{1}{r_{1,f}\left(\frac{l_{1,f}}{\omega_b \cdot r_{1,f}} \cdot s + 1\right)} \qquad (2.14)$$

A detailed block diagram for the current controller can be shown in Figure 2.5 representing the direct and quadrature axis modeling equations separated from each other. It can be noted that adding both coupling and disturbance terms in the control variable resulted in having compensated signals that can cancel out these terms and lead to a simplified block similar to the one obtained in Figure 2.3.
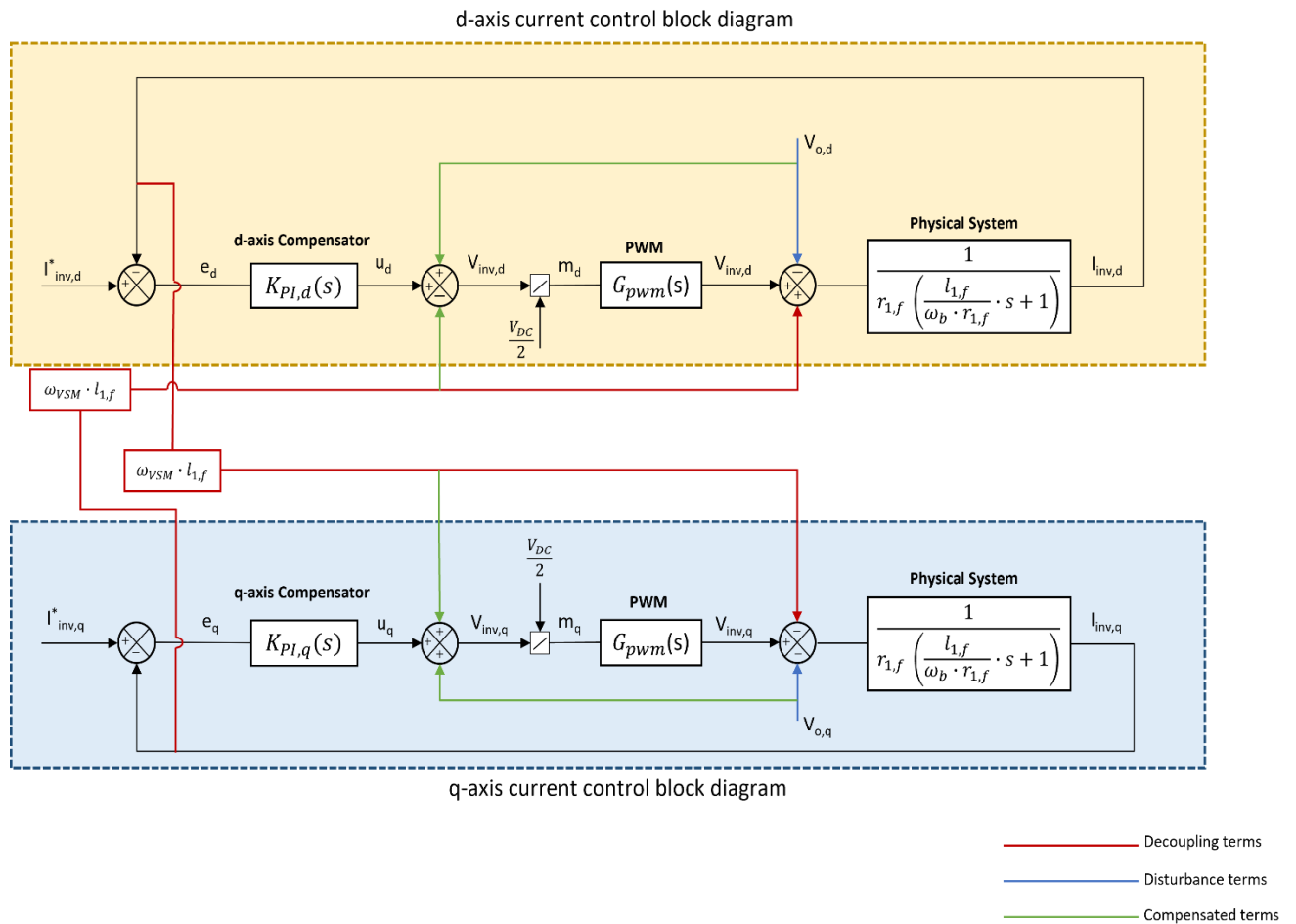
Figure 2.5 Detailed closed loop diagram of current controller with decoupling, disturbance and compensating terms.

From Figure 2.5, it can be seen that the compensated terms do not cancel out both disturbance and coupling signals completely due to the presence of the transfer function of the pulse width modulation ($G_{pwm}(s)$). The compensation terms are first multiplied by this transfer function before removing coupling and disturbances. The effect of the PWM transfer function is small and is usually neglected in the design process. In this thesis, the pulse width modulation transfer function will be assumed ideal, meaning the transfer function of the PWM itself will be neglected and will be represented by 1. Hence, the effect of this transfer function on the compensated terms is completely removed and these terms can be assumed to fully decouple the system and compensate disturbances.

In order to ensure the validity of this assumption, the bandwidth of the current controller must be 10 times lower than the bandwidth of pulse width modulation [15]. Thus, the current controller will be 10 times slower than PWM. In this case, the

dynamics of PWM do not interact much with the current controller and can be represented as an ideal block without any delay or effect on the current controller [16].

The bandwidth of the PWM is determined by its switching frequency. In [17], the transfer function of PWM was represented accordingly.

$$G_{pwm}(s) = \frac{1}{T_{pwm} \cdot s + 1} \qquad , T_{pwm} = \frac{1}{2 \cdot f_{sw}} \qquad (2.15)$$

f_{sw} is the switching frequency, and the bandwidth is the reciprocal of T_{pwm}, thus bandwidth can be denoted by $2 \cdot f_{sw}$. The switching frequency is 3 kHz as mentioned before in the definition of the case study.

Figure 2.3 can be further simplified according to the assumption of having an ideal PWM transfer function to obtain a simplified open loop representation of the current controller as shown in Figure 2.6.
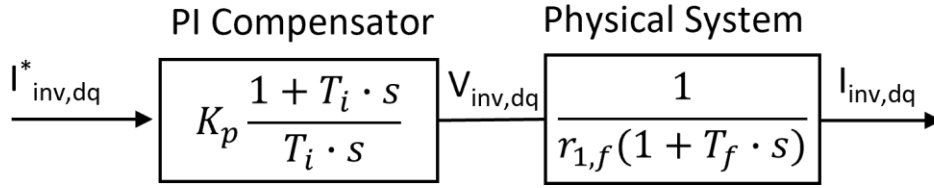
Figure 2.6. Simplified open loop block diagram of current controller without PWM.

where

$$T_{i,c} = \frac{K_{p,c}}{K_{i,c}} \qquad , T_{f,c} = \frac{l_{1,f}}{\omega_b \cdot r_{1,f}} \qquad (2.16)$$

K_P is the proportional gain of the PI controller, K_i is the integral gain of the PI controller, while other variables were defined before in Table 2-1.

The open loop transfer function of the current controller can be defined from Figure 2.6 as shown in (2.17).

$$H_{OL} = \frac{K_{p,c} \left(1 + T_{i,c} \cdot s \right)}{r_{1,f} \cdot T_{i,c} \cdot s \left(1 + T_{f,c} \cdot s \right)} \qquad (2.17)$$

The current controller in Figure 2.6 can be tuned by emulating the modulus optimum criteria by using the following criteria [20].

$$
\begin{cases}
\text{Pole \& zero cancelation :} & T_{i,c} = T_f \\
\\
\text{Time constant limit:} & T_c > 10 \cdot T_{pwm}
\end{cases}
$$

The first condition is set to remove the dynamics of the filter branch, while the second condition follows what we have proposed before in assuming an ideal transfer function for the pulse width modulation by placing a settling time for the current controller 10 times slower than the PWM.

By applying the first tuning criteria, $T_i = T_f$ eliminating the pole of the physical system with the zero of the PI controller, the open loop transfer function from (2.17) can be simplified according to (2.18).

$$
H_{OL} = \frac{K_{p,c}}{r_{1,f} \cdot T_{i,c} \cdot s} = \frac{K_{p,c}}{r_{1,f} \cdot T_{f,c} \cdot s} \tag{2.18}
$$

To define the time constant of the current controller, in tuning second criteria, the closed loop transfer function should be obtained first. By applying (2.19), defined by control theory.

$$
H_{CL} = \frac{H_{OL}}{1 + H_{OL} \cdot H_{feedback}} \tag{2.19}
$$

Where

$$
H_{feedback} = 1
$$

The closed loop transfer function can be defined as (2.20).

$$
H_{CL} = \frac{1}{\dfrac{r_{1,f} \cdot T_{f,c} \cdot s}{K_{p,c}} + 1} = \frac{1}{\dfrac{l_{1,f} \cdot s}{K_{p,c} \cdot \omega_b} + 1} \tag{2.20}
$$

The time constant can be obtained from (2.20) as follows.

$$T_c = \frac{l_{1,f}}{K_{p,c} \cdot \omega_b} \tag{2.21}$$

Applying (2.21) and (2.16), we can obtain the proportional and integral gains equations.

$$K_{p,c} = \frac{l_{1,f}}{T_c \cdot \omega_b} \qquad\qquad K_{i,c} = \frac{r_{1,f}}{T_c} \tag{2.22}$$

Both controller gains depend on our choice of time constant in this case. Choosing a suitable time constant depends on two factors:

1) Having a high bandwidth for the current controller to prevent the voltage controller from having a low bandwidth, thus interacting with the inertia emulation block [18].
2) The bandwidth of the current controller should be around 10 times smaller than the PWM bandwidth. The switching frequency for the PWM is assumed to be 10 kHz. The lower the value of this switching frequency, the lower the bandwidth of PWM becomes and the more risk on the stability of the system.

Based on these factors the time constant of the current controller was chosen to be around 0.2 ms and the bandwidth of current controller is 5000 rad/s. It should be noted that the bandwidth of the current controller in that case is not 10 times smaller than that of the PWM. This choice was made to increase the bandwidth of the voltage controller and prevent interference with the power block.
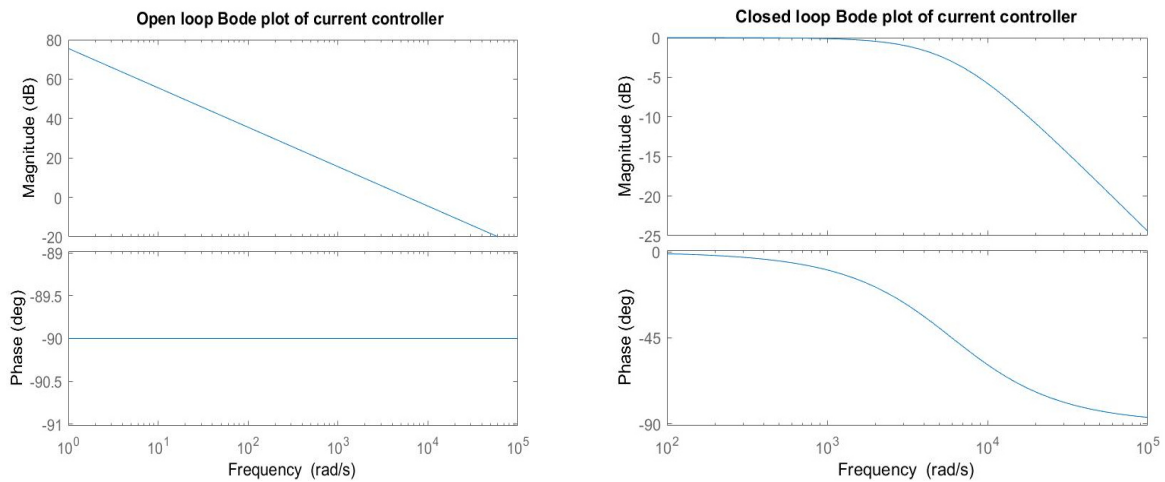
Figure 2.7. The Figure on the left is the Bode plot diagram for the open loop transfer function of current controller, while the one on right represents the bode diagram for the closed loop transfer function of current controller.

The bode plot for both the open loop transfer function and closed loop transfer function of the current controller, adapted from (2.17) and (2.20), is shown in Figure 2.7, representing the magnitude in decibels and phase in degrees. The bandwidth of the current controller can be estimated from the closed loop bode plot diagram, where the bandwidth is defined by the frequency at which the magnitude of the bode plot is equal to -3 decibels.

Moreover, the open loop bode plot of the current controller with the PWM transfer function considered is shown in Fig. 2.8 to make sure that the system is still stable even after considering a high bandwidth for the current controller. The phase margin is shown to be almost 50 degrees. This confirms that the assumption of neglecting the PWM transfer function is valid and does not affect the overall system stability even when choosing a bandwidth for the current controller that is not 10 times smaller than the bandwidth of the PWM.
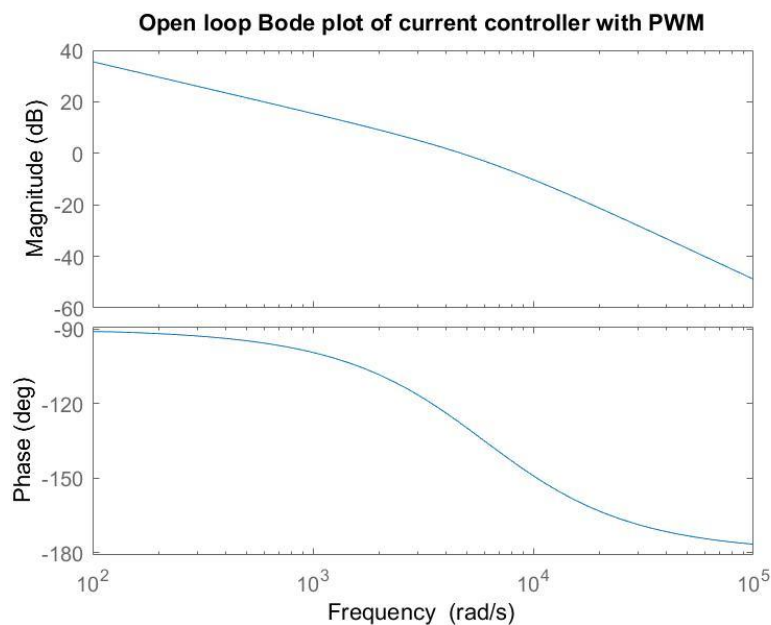
Figure 2.8 Bode diagram of the open loop of the current controller considering the PWM transfer function.

2.3.2. Voltage Controller

The voltage controller essentially follows the voltage reference signals sent by the reactive power droop and inertia emulation block. Having a voltage controller ensures that the grid-forming inverter reaches those references with zero steady-state error. The voltage controller is also responsible for sending current references to the current controller; thus, it is mandatory for implementing a current controller.

The block diagram in Figure 2.9 shows the closed-loop feedback representation of the voltage controller. The block diagram has three blocks represented by the PI compensator, the current controller, and the physical system.
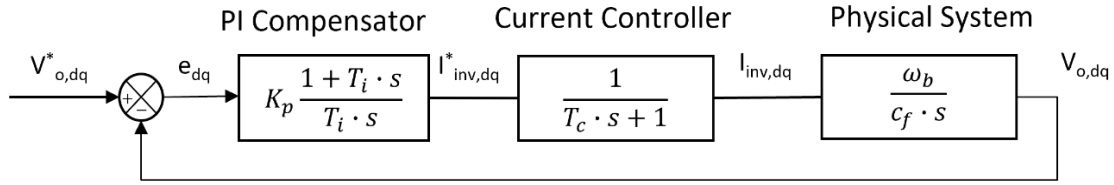
Figure 2.9. Closed loop block diagram of voltage controller

The current controller is represented by its closed-loop transfer function, which is a first-order due to neglecting the transfer function of the pulse width modulation. Because of that the current controller transfer function doesn't require any further approximations for the tuning of voltage controller.

The electrical system's physical equations will be modeled to identify the transfer function of the physical system, control variables, and disturbances as well as how to compensate for them. The physical system for voltage controller design can be represented by Kirchhoff's current law, which is found in equation 2.1, but in SI units and alpha-beta frame.

$$\bar{I}_{inv_{\alpha\beta}} = \bar{I}_{c_{\alpha\beta}} + \bar{I}_{o_{\alpha\beta}} \tag{2.23}$$

Substituting the capacitor current equation from 2.1, in SI units, into 2.23 to get.

$$\bar{I}_{inv_{\alpha\beta}} = C_f \frac{d\bar{V}_{o_{\alpha\beta}}}{dt} + \bar{I}_{o_{\alpha\beta}} \tag{2.24}$$

Referring (2.24) into the dq frame as performed in section 2.3.1 for the current controller to get.

$$I_{inv,dq} \cdot e^{j\delta} = C_f \frac{d(V_{o,dq} \cdot e^{j\delta})}{dt} + I_{o,dq} \cdot e^{j\delta} \tag{2.25}$$

Solving the differential of a product the equation expands accordingly.

$$I_{inv,dq} \cdot e^{j\delta} = C_f \frac{dV_{o,dq}}{dt} \cdot e^{j\delta} + j \cdot C_f \cdot V_{o,dq} \cdot e^{j\delta} \cdot \frac{d\delta}{dt} + I_{o,dq} \cdot e^{j\delta} \tag{2.26}$$

Eliminating the exponential and substituting $\frac{d\delta}{dt} = W_{vsm}$ into (2.26).

$$I_{inv,dq} = C_f \frac{dV_{o,dq}}{dt} + j \cdot C_f \cdot V_{o,dq} \cdot W_{vsm} + I_{o,dq} \tag{2.27}$$

The per unit representation can be obtained by dividing the equation with the base values $I_b = V_b C_b \omega_b$.

$$i_{inv,dq} = \frac{c_f}{\omega_b} \frac{dv_{o,dq}}{dt} + j \cdot c_f \cdot v_{o,dq} \cdot \omega_{vsm} + i_{o,dq} \tag{2.28}$$

Rearranging (2.28) to obtain

$$\frac{dv_{o,dq}}{dt} = i_{inv,dq} \frac{\omega_b}{c_f} - j \cdot v_{o,dq} \cdot \omega_{vsm} \cdot \omega_b - i_{o,dq} \frac{\omega_b}{c_f} \tag{2.29}$$

The d-axis equation and q-axis equation can be written separately to show the coupling terms in equation (2.30).

$$\frac{dv_{o,d}}{dt} = i_{inv,d} \frac{\omega_b}{c_f} + \cdot v_{o,q} \cdot \omega_{vsm} \cdot \omega_b - i_{o,d} \frac{\omega_b}{c_f}$$

$$\frac{dv_{o,q}}{dt} = i_{inv,d} \frac{\omega_b}{c_f} - v_{o,d} \cdot \omega_{vsm} \cdot \omega_b - i_{o,q} \frac{\omega_b}{c_f} \tag{2.30}$$

In (2.29), $v_{o,dq}$ is the state variable, $i_{inv,dq}$ is the control variable, $i_{o,dq}$ is a disturbance, while the term $j \cdot \omega_{vsm}$ presents a coupling between the dq frame equations. The coupling prevents representing the system as a single input single output making the tuning more difficult. Because of that, the choice of control variable u_{dq} is performed to have a decoupling terms and disturbance compensation.

$$u_{dq} = i_{inv,dq} - j \cdot v_{o,dq} \cdot \omega_{vsm} \cdot \omega_b \cdot \frac{c_f}{\omega_b} - i_{o,dq} \tag{2.31}$$

Substituting (2.31) into (2.29).

$$\frac{dv_{o,dq}}{dt} = \frac{\omega_b}{c_f} \cdot u_{dq} \tag{2.32}$$

Applying Laplace, the transfer function of the physical system in terms of the control variable u_{dq} can be written accordingly.

$$G_{phy,v}(s) = \frac{v_{o,dq}(s)}{u_{dq}(s)} = \frac{\omega_b}{c_f \cdot s} \tag{2.33}$$

A detailed block diagram of the voltage controller is shown in Figure 2.10, representing the dq axis diagrams separately and highlighting coupling, disturbance, and compensating terms. It is important to notice that Figure 2.9 is a simplified version of Figure 2.10, which is obtained after assuming full compensation of coupling and disturbance terms.
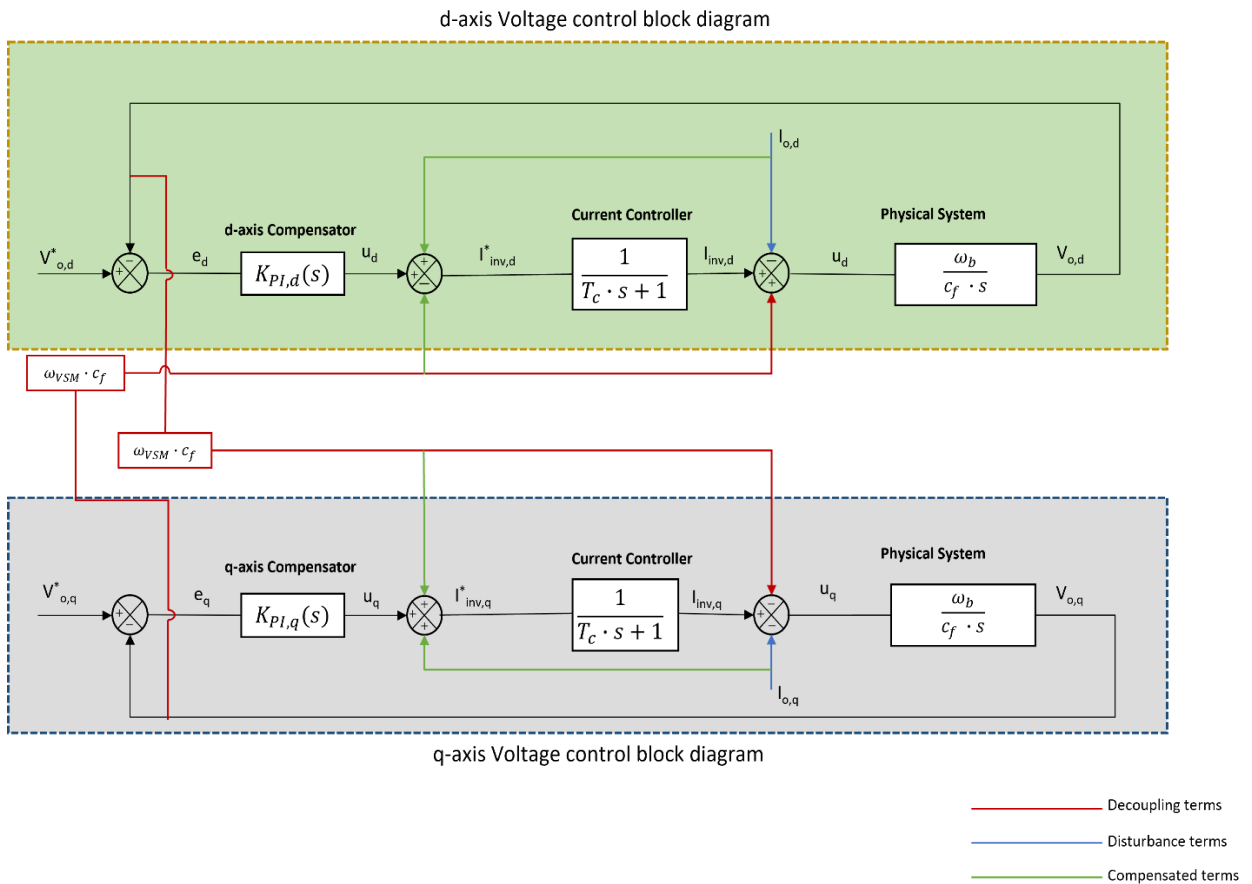
Figure 2.10 Detailed block diagram of voltage controller with decoupling, disturbance and compensating terms.

In Figure 2.10, the presence of the current controller affects the compensating terms from the controller. This effect can't be neglected anymore, like the case of PWM for the current controller, since we will have to also assume that the voltage controller bandwidth is 10 times smaller than the current controller bandwidth, which might lead to having a very low bandwidth for the voltage controller, leading to interacting

with the power control loop, resulting in an unstable system. In this case, the current controller transfer function is considered, and compensating terms don't completely remove the coupling and disturbance terms.

The effect of the coupling terms on the system can be neglected as it is small. However, the effect of the disturbance might affect the behavior of the system and should be mitigated.

One way to allow a complete compensation for the disturbance is to use a feedforward transfer function that removes the effect of the current controller, leading to a complete removal of the disturbance. Hence, the feedforward transfer function should be the inverse of the current controller transfer function. This is not possible to implement as the feedforward transfer function will be only a zero [19].

As a consequence, complete compensation for the disturbance is not possible even if it was assumed. This leads to having a transfer function that can relate the disturbance, which is grid current in that case, and the voltage we are trying to control. This transfer function will represent an impedance for the inverter, which might cause some issues.

The inverter system being controlled is assumed to be predominantly inductive. In fact, the virtual impedance design in the next section depends on making the system predominantly inductive to decouple the dynamics of active and reactive power. Having a self-impedance for the inverter, caused by the voltage controller, might affect the inductive behavior of the system [19].

However, it was proven by [19] that this self-impedance has an inductive behavior. Hence, it doesn't affect the overall performance of the system, but it still represents a problem for tuning the voltage controller since it can't be completely compensated.

A solution is to adopt the symmetrical optimum tuning method. Using this tuning methodology can allow the assumption of neglecting the disturbance since it tunes the system to have a high phase margin [18]. This ensures the stability of the system. Of course, the system is not expected to behave exactly according to our modeling and tuning since the disturbance will affect it. However, the main idea is to have a stable voltage controller even with the effect of this disturbance, which is why the symmetrical optimum is implemented in the first place.

The system open loop transfer function can be obtained from Figure 2.9 according to the following equation [20].

$$H_{OL} = \frac{K_{p,v}\left(1 + T_{i,v} \cdot s\right) \cdot \omega_b}{T_{i,v} \cdot s \left(1 + T_c \cdot s\right) \cdot c_f \cdot s} \tag{2.34}$$

The closed loop transfer function can then be identified by substituting (2.34) into (2.19).

The Symmetrical optimum criterion is applied to the open loop transfer function found in (2.34) to have the maximum phase at the crossover frequency. Based on this criterion, the parameters of the PI compensator and current controller are expressed in terms of a design parameter "a" that relates the tuning to the damping factor ζ according to (2.35) [20].

$$\omega_c = \frac{1}{a \cdot T_c}, \qquad\qquad T_{i,v} = a^2 \cdot T_c \tag{2.35}$$

$$a = 2\zeta + 1$$

The open loop transfer function in (2.34) is expressed in the frequency domain $s = j\omega$. Substituting the frequency with the crossover frequency from (2.35) and substituting the PI compensator T_i with its equation found in (2.35), the open loop transfer function can be written as defined in (2.36).

$$H_{OL}(j\omega_c) = \frac{K_{p,v}\left(1 + a^2 \cdot T_c \cdot j\dfrac{1}{a \cdot T_c}\right) \cdot \omega_b}{a^2 \cdot T_c \cdot j\dfrac{1}{a \cdot T_c}\left(1 + T_c \cdot j\dfrac{1}{a \cdot T_c}\right) \cdot c_f \cdot j\dfrac{1}{a \cdot T_c}} \tag{2.36}$$

Simplifying the terms of (2.36).

$$H_{OL}(j\omega_c) = \frac{K_{p,v}\left(1 + j\dfrac{1}{a}\right) \cdot \omega_b}{j \cdot a\left(1 + j\dfrac{1}{a}\right) \cdot c_f \cdot j\dfrac{1}{a \cdot T_c}} = \frac{K_{p,v} \cdot \omega_b\left(1 + j \cdot a\right)}{\left(a + j\right) \cdot -1 \cdot c_f \cdot \dfrac{1}{a \cdot T_c}} \tag{2.37}$$

Expressing (2.37) in terms of magnitude will allow the cancelation of $(1 + j \cdot a)$ with $(a + j)$ as well as removing the factor -1.

$$|H_{OL}(j\omega_c)| = \frac{K_{p,v} \cdot \omega_b}{c_f \cdot \dfrac{1}{a \cdot T_c}} \tag{2.38}$$

Since we are exploring the magnitude of the open loop transfer function at the crossover frequency, then this magnitude will be equal to one. The PI compensator

parameters fulfilling the symmetrical optimum criterion can then be expressed by (2.39).

$$K_{p,v} = \frac{c_f}{\omega_b \cdot a \cdot T_c}, \qquad K_{i,v} = \frac{K_{p,v}}{a^2 \cdot T_c} = \frac{c_f}{\omega_b \cdot a^3 \cdot T_c^2} \qquad (2.39)$$

The choice of design parameter (a) depends on achieving a suitable bandwidth and damping factor. Figure 2.11 shows the bandwidth along with the damping factor for different design parameter values ranging from 1 to 10. The goal is to have a damping factor corresponding to a low overshoot and a bandwidth corresponding to a fast response for the voltage controller. It must be noted that the bandwidth has to be lower than the bandwidth of the current controller and high enough to prevent interference with the power block.
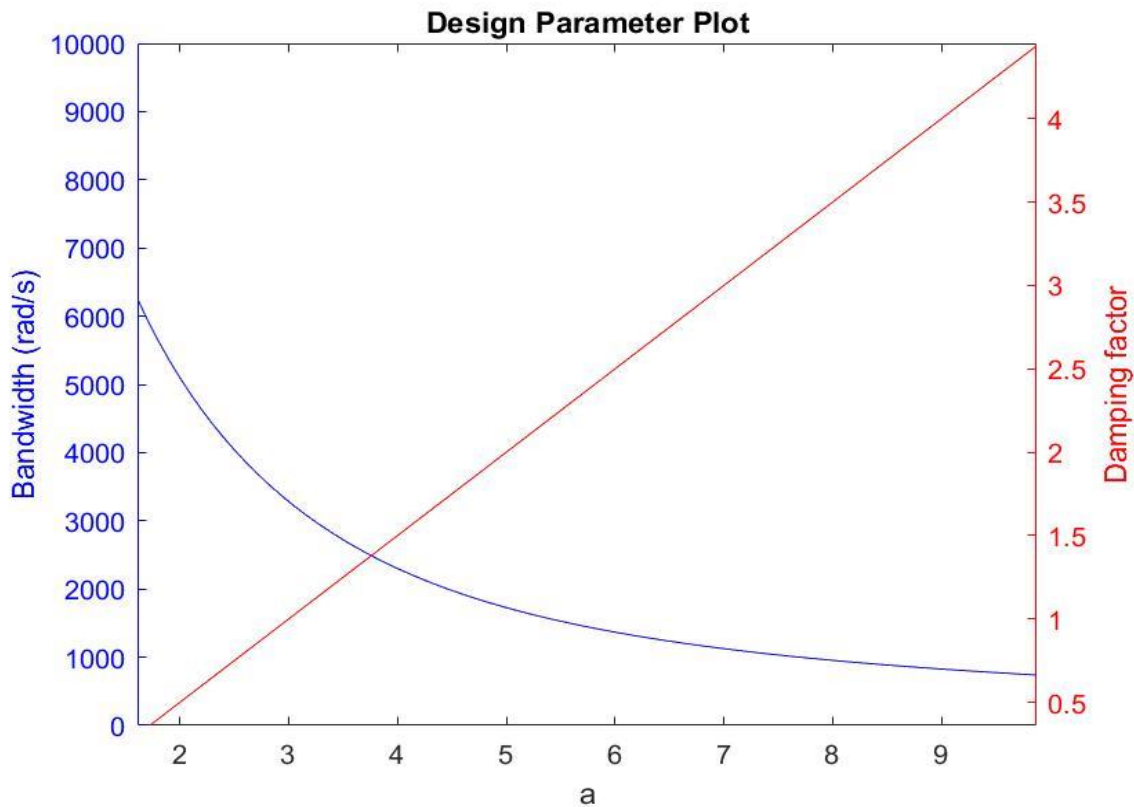
Figure 2.11. Bandwidth and Damping factor plot of voltage controller for different design parameter values

From Figure 2.11, a value less than two for the design parameter is not desired since it results in a damping factor less than 0.5, thus allowing a very high overshoot. Also, a value more than 5 is not beneficial because it reflects a low value of bandwidth less

than 2000 rad/s, risking interactions with the inertia emulation block. Hence, the values of design parameter, that achieve the mentioned objectives, range from 2 to 5. The voltage controller step response for this range of values is plotted in Figure 2.12 showing the exact overshoot and response speed for each value. The design parameter "a" is chosen to be of value 4 since it results in a low overshoot of about 20% and an adequately fast response of the voltage controller.
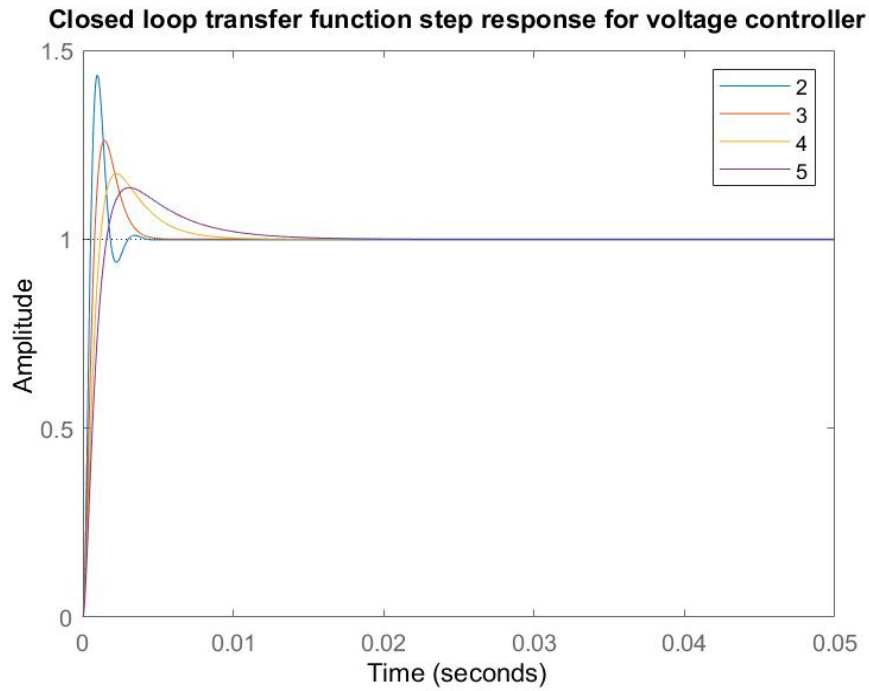
Figure 2.12. Step response for closed loop transfer function of voltage controller using different design parameters values.
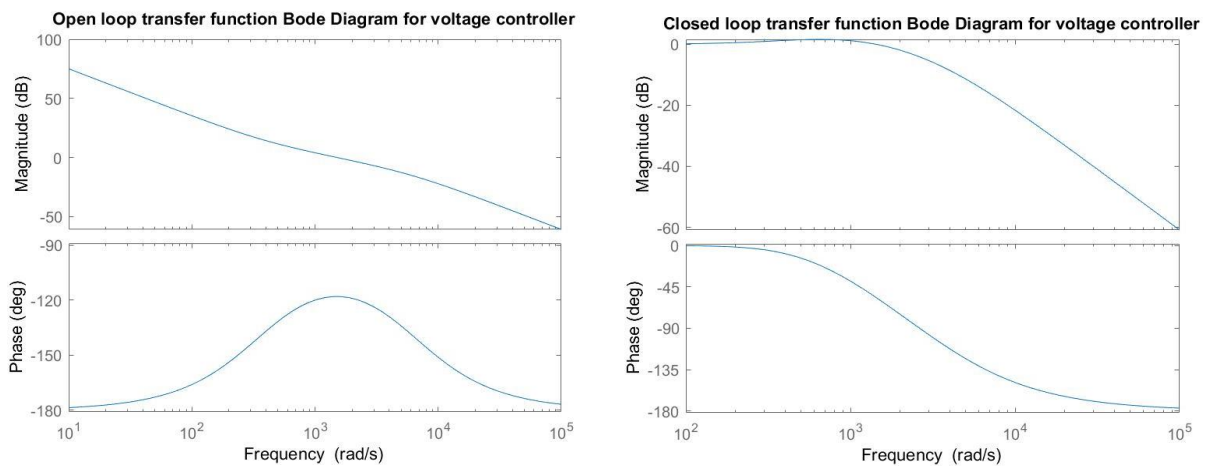
Figure 2.13. The Figure on the left is the Bode plot diagram for the open loop transfer function of voltage controller, while the one on right represents the bode diagram for the closed loop transfer function of voltage controller.

Figure 2.13 represents the bode plot for both the open loop and closed loop transfer functions of the voltage controller. The bode plot of the open loop transfer function confirms achieving a maximum phase margin of about 60 degrees, which is very suitable for stability purposes, while the bode plot of the closed loop transfer function shows a bandwidth of about 2300 rad/s that gives a relatively fast response.

2.3.3. Virtual Impedance

The virtual impedance design can be implemented for various objectives according to [21]. Virtual impedances can be classified with respect to their functions which are decoupling P/Q control, damping subsynchronous oscillation, harmonic reduction, and fault current limitation.

The virtual impedance in this thesis is based on achieving a decoupled active and reactive power flow. Having a decoupled power flow allows a separate control design for each of the active power and reactive power blocks. The active and reactive power flow between the grid and inverter can be expressed according to (2.40) by referring to Figure 2.1, assuming a short transmission line [22].

$$P = \frac{|V_{inv}|\,|V_g|}{|Z|}\cos(\theta - \delta) - \frac{|V_{inv}^2|}{|Z|}\cos\theta$$

$$Q = \frac{|V_{inv}|\,|V_g|}{|Z|}\sin(\theta - \delta) - \frac{|V_g^2|}{|Z|}\sin\theta$$

(2.40)

Where $Z = |Z|\angle\theta$ is the line impedance between the inverter and the grid, $V_{inv} = |V_{inv}|\angle\delta$ is the inverter voltage. The grid voltage is considered as a reference in that case; hence its angle is zero. By assuming an inductively dominant impedance $\theta \approx 90$, (2.40) can be further simplified as follows.

$$P = \frac{|V_{inv}|\,|V_g|}{|X|}\sin\delta$$

$$Q = \frac{|V_{inv}|\,|V_g|}{|X|}\cos\delta - \frac{|V_g^2|}{|X|}$$

(2.41)

Moreover, since angle δ is relatively small, a further simplification can be done accordingly.

$$P = \frac{|V_{inv}|\,|V_g|}{|X|}\delta$$

$$Q = \frac{|V_g|}{|X|}\left(|V_{inv}| - |V_g|\right)$$

(2.42)

It can be concluded from (2.42) that the active power flow is proportional to the inverter angle, while the reactive power flow is proportional to the voltage difference between the inverter and the grid. Hence, it is possible to decouple the active and reactive power flow equations, relating active power to the inverter voltage angle and reactive power to the inverter voltage magnitude. This way the design of active power block and reactive power droop can be implemented separately.

The objective of virtual impedance is to ensure the predominant inductive behavior of the system, meaning having a high $\frac{X}{R}$ ratio. This ensures the validity of the assumption performed to get (2.41).

The virtual impedance is not physically present in the system rather it is virtually implemented by varying the voltage references sent to the voltage controller. The general circuit line diagram between the inverter and the grid is represented in Figure 2.14.
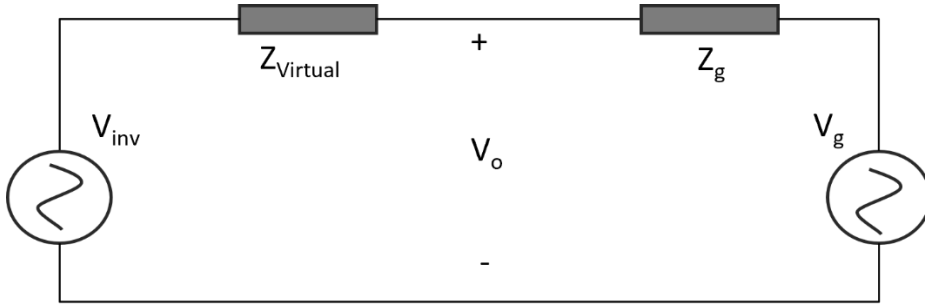
Figure 2.14. Circuit line diagram of the inverter with a virtual impedance

V_{inv} is the inverter voltage in phasor form, V_o is the voltage at the point of common coupling, V_g is the grid voltage, Z_g is the grid impedance, while $Z_{Virtual}$ is the virtual impedance. It can be noted that the value of this virtual impedance will correspond to a voltage drop and a phase shift to the voltage at point of common coupling, varying the references sent to the voltage controller. (2.43) shows the effect of virtual impedance on references sent to voltage controller.

$$V_{o,dq}^* = \widehat{V^r} - (r_v + j \cdot l_v \cdot \omega_{vsm}) \cdot i_{o,dq}$$

(2.43)

$\widehat{V^r}$ refers to the old voltage references without the influence of virtual impedance, $V^*_{o,dq}$ is the new voltage references after applying virtual impedance, r_v is the virtual resistance, while l_v is the virtual inductance.

The implementation of the control loop block is defined by Figure 2.15, which is adapted from (2.43). The tuning of the virtual impedance parameters is based on ensuring a high $\frac{X}{R}$ ratio as well as power-angle transient stability.

Based on these requirements, the virtual resistance is tuned to be zero, while the virtual inductance is tuned to a value of 0.2 pu. These values should correspond to a complete decoupling of active and reactive power control blocks, improve the transient stability in terms of small signal disturbances, and enhance the dynamic behavior of the inverter by limiting the power overshoot.
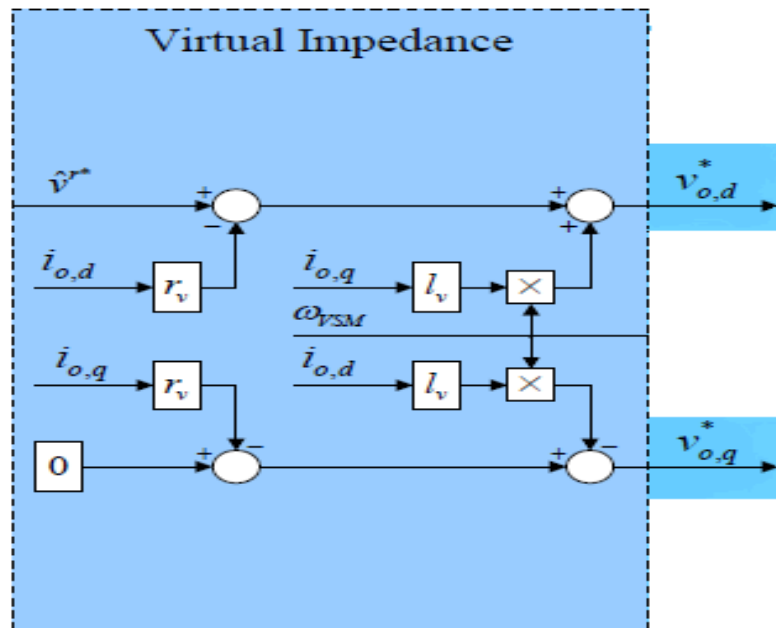
Figure 2.15. Control block implementation of virtual impedance.

2.3.4. Phase Locked Loop

The phase locked loop is used in the control topology for the estimation of grid frequency. Having an estimated frequency is essential to remove the droop characteristic restriction on drag coefficient and tune it independently without any constraints. The phase locked loop measures the frequency of the capacitor voltage. Hence, the dq axis components of the capacitor voltage measured by the PLL can be defined by (2.44) [16].

$$V_{o,d} = \widehat{V_o} \cos(\omega_o t + \theta_o - \rho)$$

$$V_{o,q} = \widehat{V_o} \sin(\omega_o t + \theta_o - \rho)$$

(2.44)

Based on (2.44), a value of $\rho(t) = \omega_o t + \theta_o$ will correspond to $V_{o,q} = 0$. Therefore, the control mechanism is devised to regulate $V_{o,q}$ to zero. This can be done accordingly in per unit.

$$\omega(t) = K(s) \cdot v_{o,q}(t)$$

(2.45)

$$\frac{d\rho}{dt} = K(s) \cdot \omega_b \cdot v_{o,q}(t) = K(s) \cdot \omega_b \cdot \sin(\omega_o t + \theta_o - \rho)$$

ρ represents the phase locked loop angle, $\omega(t)$ is the reference rotating speed of the phase locked loop, while ω_o and θ_o are the speed and phase shift of the capacitor voltage.

According to (2.45), the PLL might fall into a limit cycle if not initiated properly because of the sinusoidal function. This will prevent the PLL angle from tracking the capacitor voltage angle. To avoid this issue, suitable initial conditions are defined by (2.46) [16].

$$\omega(0) = \omega_o , \quad \omega_{min} \leq \omega \leq \omega_{max}$$

(2.46)

The initial condition will allow the PLL to track the term $\omega_o t + \theta_o$ with less error. Because of that the term $\omega_o t + \theta_o - \rho$ is assumed to be close to zero and (2.45) can be further simplified as follows.

$$\frac{d\rho}{dt} \cong K(s) \cdot \omega_b \cdot (\omega_o t + \theta_o - \rho) \cong K(s) \cdot \omega_b \cdot v_{o,q}(t)$$

(2.47)

As mentioned before, the control is based on achieving a quadrature component of capacitor voltage equivalent to zero. Hence, the state variable of the control loop will be $v_{o,q}(t)$. One of the problems that need to be considered in the design is the unbalanced or harmonic distortion of the three phase voltages that will affect the measurement of $v_{o,q}(t)$. A filter is manifested to get rid of this issue, which is presented by (2.48) [16].

$$G_{filter,PLL} = \frac{\omega_{cutoff,PLL}}{\omega_{cutoff,PLL} + s}$$

(2.48)

The filter design is a low pass filter that should have a cutoff frequency eliminating the harmonics as well as avoiding phase shift of PLL angle.

The negative sequence component will result in harmonic components with the lowest order harmonic corresponding to a frequency of $2\omega_o$, while the fifth order harmonic is the lowest harmonic order of positive sequence harmonics since the third order harmonic does not appear as it is a zero-sequence component. The negative sequence component is more important since it results in a frequency much lower than the positive sequence harmonics and during faults its magnitude can be significantly larger [16]. As a result, the bandwidth of the filter will be limited by the negative sequence component. So, a bandwidth of 200π is expected to remove all unbalanced and harmonic distortion components.

To get rid of the harmonic components and avoid phase misalignment. The filter design will be implemented with a bandwidth of 600 rad/s.

The open loop block diagram can be implemented by integrating the filter transfer function (2.48) with (2.47) as shown in Figure 2.16 [20].
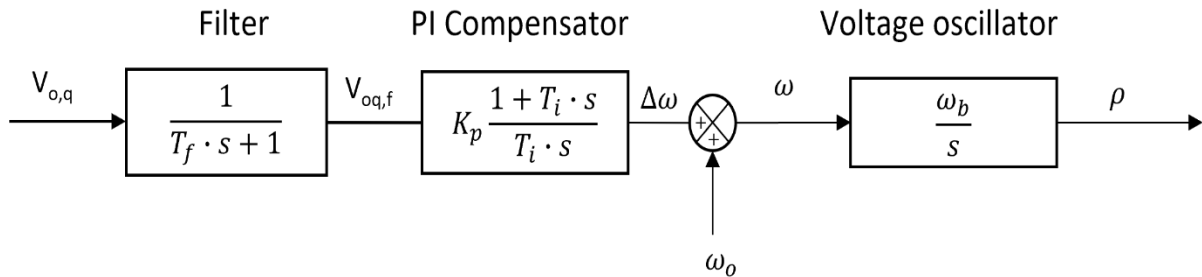
Figure 2.16. Open Loop block diagram of Phase Lock Loop

From Figure 2.16, the open loop transfer function is written in (2.49).

$$H_{OL} = \frac{K_{p,PLL}\left(1 + T_{i,PLL} \cdot s\right) \cdot \omega_b}{T_{i,PLL} \cdot s \left(1 + T_{f,PLL} \cdot s\right) \cdot s} \tag{2.49}$$

The PLL can also be tuned using the symmetrical optimum criterion as voltage controller according to [23]. In that case, the same procedure will be adopted, and the PI compensator coefficients can also be written in terms of a design factor "a" according to (2.50).

$$K_{p,PLL} = \frac{1}{\omega_b \cdot a \cdot T_{f,PLL}}, \qquad K_{i,PLL} = \frac{K_{p,PLL}}{a^2 \cdot T_{f,PLL}} = \frac{1}{\omega_b \cdot a^3 \cdot T_{f,PLL}^2} \tag{2.50}$$

Similarly, the graph relating design factor with damping ration and bandwidth of the closed loop system is shown in Figure 2.17.
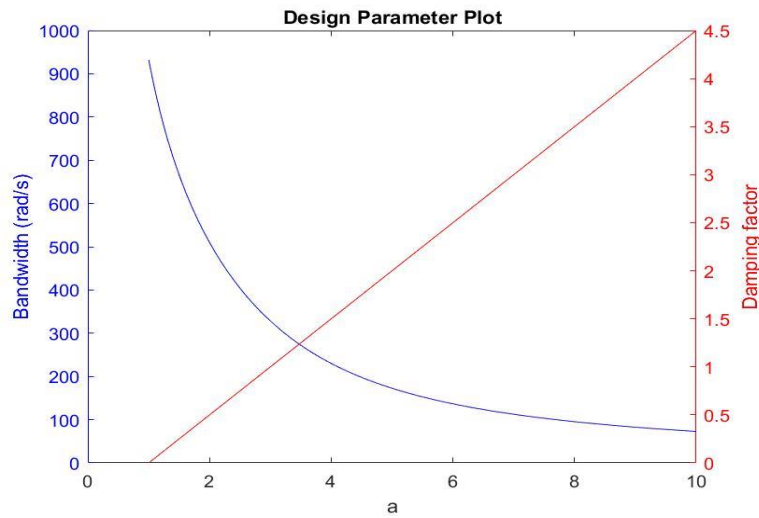
Figure 2.17. Bandwidth and damping factor of PLL for different design parameters values

It can be noted that higher values of design parameter can lead to a very low bandwidth. The bandwidth corresponding to a damping factor of 1 is about 300 rad/s, which will result in a slow response of the PLL relative to the model implemented. For this reason, the damping factor chosen for the design is the critical damping of value $\frac{1}{\sqrt{2}}$. Hence, the design parameter "a" value will be around 2.4.
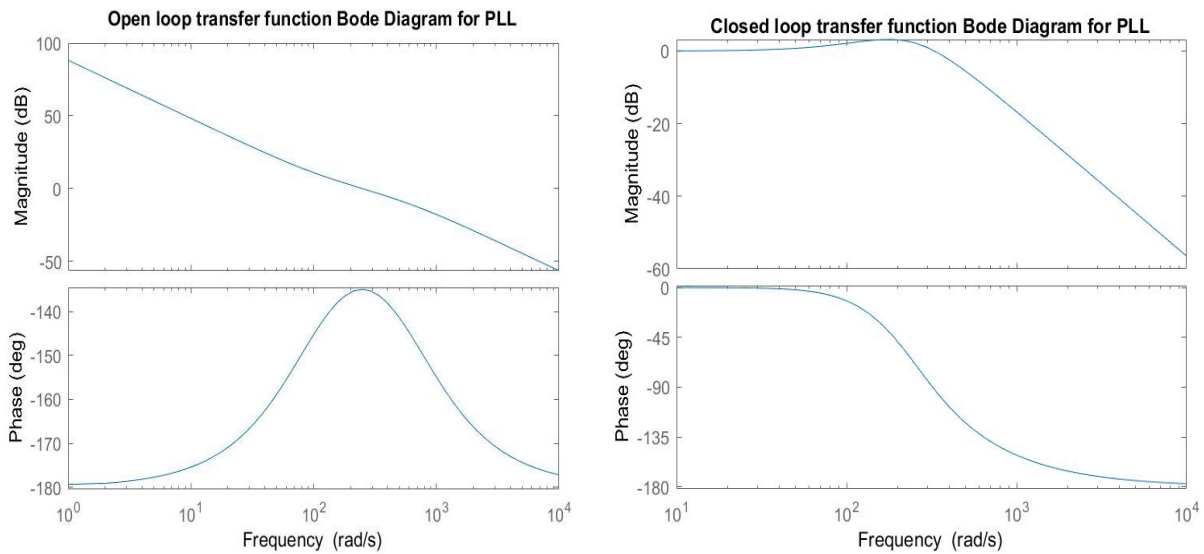
Figure 2.18. The Figure on the left is the Bode plot diagram for the open loop transfer function of phase locked loop, while the one on right represents the bode diagram for the closed loop transfer function of phase locked loop.

The bode plot in Figure 2.18 represents the bode diagram for both the open loop and closed loop transfer functions of the phase locked loop. The magnitude is expressed in decibels and the phase in degrees. The maximum phase is achieved at the crossover frequency, hence maximizing the phase margin, and improving the system stability.

Moreover, the bandwidth of the closed loop for the phase locked loop is about 400 rad/s, which results in a response speed that is relatively fast. It is observed that the bandwidth of the phase locked loop is much lower than that of the voltage and current controller. However, this is not an issue since the phase locked loop is used for the estimation of the grid frequency. This means that the PLL is used in the power block itself and does not require a bandwidth that is much higher than this power block.

Nevertheless, it will be seen in the next sections that the PLL dynamics are interacting with the active power control block, resulting in a behavior slightly different from the one that is achieved by tuning the power block.

2.3.5. Reactive Power Controller

The reactive power block is set to control the capacitor voltage magnitude. Assuming a predominant inductive system, (2.42) can be used to describe the active and reactive power flow. In that case, the inverter voltage magnitude or the capacitor voltage magnitude is directly related to the reactive power flow.

The reactive power control block implemented in the model is the droop-based method shown in Figure 1.10. From this reactive power droop control, the following set of equations can be derived.

$$(q^* - q_m) \cdot k_q = -(v^* - v) \tag{2.51}$$

$$\frac{q_m(s)}{q} = \frac{\omega_c}{\omega_c + s} = \frac{1}{T_p \cdot s + 1} \tag{2.52}$$

q^* corresponds to reactive power setpoint, q_m is the measured reactive power after being filtered, q is the measured reactive power before filtering, v^* is the reference voltage magnitude, v is the output voltage magnitude to be implemented by the voltage controller, while ω_c is the filter cut-off frequency.

The characteristic behavior of the reactive power droop control can be explained in Figure 2.19. Increasing the voltage magnitude across the inverter corresponds to a decrease in the reactive power measurement, while a decrease in the voltage magnitude corresponds to an increase in the reactive power supplied by the inverter.
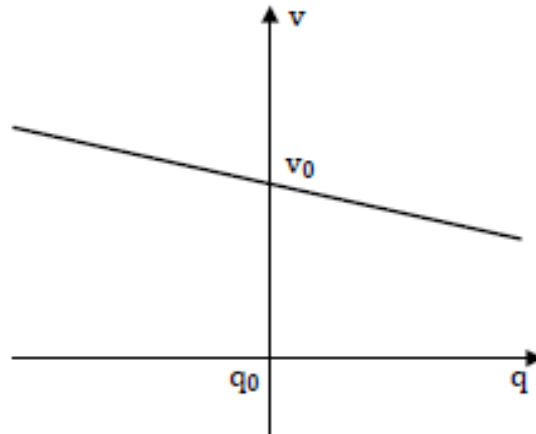
Figure 2.19. Reactive power droop diagram

For tuning the reactive power controller, the filter is mainly used to filter the harmonics from the measured reactive power. The value of the cut-off frequency is 100, thus T_p is 10 ms [19].

The value of the droop coefficient is tuned based on two requirements. The first requirement corresponds to the maximum allowable voltage variation at the capacitor node. Then, the second requirement is to set the amount of reactive power to counter this maximum variation. The values for the maximum voltage variation and reactive power countering this variation are set to 10% and inverter rated reactive power, which is 1 per unit, respectively.

Based on these requirements, the value of the reactive power droop coefficient can be calculated by using (2.51) to give the following.

$$k_q = 0.1 \ pu \tag{2.53}$$

2.3.6. Active Power Controller

The active power controller or the inertia emulation block is the main control block for the virtual synchronous machine. It is responsible for the synchronization with the grid, damping frequency oscillations, and providing inertia response.

The active power controller of the VSM is designed to emulate the swing equation of a synchronous generator to achieve the inertia and damping properties of a synchronous machine. The swing equation can be presented as in (2.54) [13].

$$J\frac{dW_{vsm}}{dt} = T_o - T_e - D(W_{vsm} - W_g) \qquad (2.54)$$

J is the rotor inertia, ω_{vsm} is the angular frequency of the machine, ω_g is the angular frequency of the grid, which shall be presented by a PLL, T_o is the mechanical torque, T_e is the electromagnetic torque, and D is the damping torque associated with damper windings.

The swing equation in (2.54) can be expressed in terms of power by multiplying the terms of (2.54) by W_{vsm}. Then, the equation can be expressed in per unit, introducing the time constant instead of rotor inertia [13].

$$T_a\frac{d\omega_{vsm}}{dt} = p_o - p_e - K_d(\omega_{vsm} - \omega_g) \qquad (2.55)$$

T_a is the time constant, p_o is the mechanical power in per unit, p_e is the electrical power in per unit, and K_d is the damping constant.

The dynamic behavior of the virtual synchronous machine is determined by the active power controller, while the outer voltage controller and inner current controller are designed to provide fast damped response to prevent interference with the active power controller dynamics and ensure the overall stability of the system.

The active power controller for the virtual synchronous machine was shown before in chapter one in Figure 1.15. It is important to note that this Figure represents the open loop diagram of the VSM active power controller, while the closed-loop control block for the VSM active power controller can be described in Figure 2.20. Both Figures are adapted from the swing equation of (2.55) to represent their block diagram.

VSM Active power controller
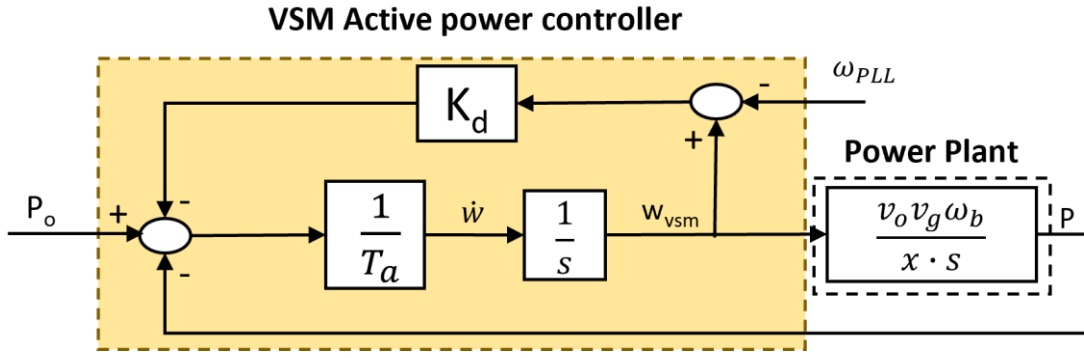
Figure 2.20. Closed loop block diagram of active power controller

P_o is the power setpoint, P is the electric power measured, and x is the reactance between the capacitor and the grid. The left part of Figure 2.20 shows the VSM active power controller. This proposed controller has two variables namely active damping and time constant, represented by k_d and T_a respectively. These two variables delineate the transient and inertial response of the active power controller, thus the virtual synchronous machine. The tuning of the active power controller variables will be defined in the next sections. The right part of Figure 2.20 describes the power plant transfer function, relating the virtual frequency of the VSM to the electric power delivered to the grid. This transfer function is defined starting from (2.42) in per unit.

$$P = \frac{|v_o|\,|v_g|}{|x|}\delta \tag{2.56}$$

The variables of (2.56) were defined before in previous sections. However, it is important to note that the angle resulting from the active power controller can be considered as the capacitor voltage angle since this angle is used to transform capacitor voltage measurements into dq rotating frame and the quadrature voltage reference is set to zero. This angle can be expressed by (2.57).

$$\frac{d\delta}{dt} = \omega_b \cdot \omega_{vsm} \tag{2.57}$$

Performing Laplace transformation for both (2.56) and (2.57), then substituting (2.57) into (2.56).

$$P(s) = \frac{|v_o|\,|v_g|}{|x|}\frac{\omega_b \cdot \omega_{vsm}(s)}{s} \tag{2.58}$$

The transfer function can be obtained as follows.

$$G_{plant}(s) = \frac{P(s)}{\omega_{vsm}(s)} = \frac{v_o \cdot v_g \cdot \omega_b}{x \cdot s} = \frac{k_g}{s} \tag{2.59}$$

It shall be mentioned that the reactance in (2.59) is calculated based on two components. The first component is defined by the grid reactance, while the second component is established by the virtual impedance reactance. The virtual impedance reactance introduces a change for the voltage references sent to the voltage controller in the dq frame. Accordingly, this change in dq voltage references will introduce a phase shift effect on the capacitor voltage.

2.3.6.1. Time Constant

The inertial behavior of the virtual synchronous machine is determined by the time constant. Nowadays, according to regulations, a grid-forming inverter should provide a constant inertial response for a given rate of change of frequency. Also, this inertial response should be predetermined and specified in the grid-forming inverter description. Hence, the time constant should be tuned to achieve a certain amount of inertial power during a specific ROCOF.

It can be derived from the swing equation a relationship linking time constant, rate of change of frequency, and change in electrical power (inertial power) by assuming the estimated frequency by PLL and virtual frequency of VSM are equal, thus cancelling the drag power term. This relationship is presented in (2.60),

$$\Delta p = T_a \frac{d\omega}{dt} \tag{2.60}$$

In this thesis, the VSM shall provide an inertial power of 0.125 pu for a ROCOF of 1 Hz/s. In other words, for every change in frequency that corresponds to 1 Hz/s, a change of 0.125 per unit will be applied to the electric power delivered to the grid. Whether this power change is incremental or decremental depends on the sign of ROCOF. Meaning, the electric power is expected to decrease if ROCOF is positive (grid accelerating), while it is supposed to increase if ROCOF is negative (grid decelerating). According to the previous specification, the time constant of the VSM can be computed.

$$0.125 = T_a \cdot \frac{1}{50}$$

$$T_a = 6.25 \ s \tag{2.61}$$

2.3.6.2. Drag coefficient

The first variable of the VSM, the time constant, was tuned to achieve the desired inertial response. The second variable, the drag coefficient, will be tuned to provide a good transient response. The objective is to have a dynamic response that almost settles in less than a second with a very low overshoot. In general, the overshoot is not desired in the virtual synchronous machine since it might result in exceeding the converter limitations.

To study the dynamic behavior of VSM, the transfer function of the closed-loop system with a VSM controller should be derived, adapting Figure 2.20 and referring the transfer function of the power plant of Figure 2.20 to (2.59).

$$G_{cl,vsm}(s) = \frac{P(s)}{P_o(s)} = \frac{\dfrac{k_g}{T_a}}{s^2 + \dfrac{k_d}{T_a}s + \dfrac{k_g}{T_a}} \tag{2.62}$$

The transfer function in (2.62) is a second order system with a natural frequency and damping ratio defined by (2.63).

$$\omega_n = \sqrt{\frac{k_g}{T_a}} \ , \qquad \zeta = \sqrt{\frac{k_d^2}{4 \cdot T_a \cdot k_g}} \tag{2.63}$$

The drag coefficient is defined to achieve a maximum overshoot of 10% at the maximum short circuit ratio. SCR is used to evaluate the system strength and is defined as the ratio between the short circuit capacity at the point of connection of inverter with the grid to the MW rating of the inverter. In terms of the written equations, the SCR basically affects the grid impedance, thus it changes the reactance between the inverter and the grid, found in the power plant transfer function of (2.59), where SCR is inversely proportional to grid reactance. In that case, SCR is directly proportional to k_g. Hence, from (2.63), the maximum SCR will result in the lowest damping ratio and the tuning should be implemented according to the maximum SCR. Accordingly, the drag coefficient is tuned as follows.

$$k_{d,min} = \sqrt{4 \cdot T_a \cdot k_{g,max} \cdot \zeta_{10\%}^2} = 111.74 \ pu \tag{2.64}$$

In that case, the drag coefficient is tuned according to the transfer function of (2.62). This transfer function assumes that the estimated frequency by PLL is constant during a change in power reference. However, this is not exactly true. Changing the reference power will cause a change in the output angle from the active power controller. This change in the output angle will present an error to the PLL, which will drive the working of the PLL to get rid of this error, resulting in the introduction of PLL dynamics and the variation of the estimated grid frequency.

In that case, the electric power can be represented in terms of both power and frequency references with their respective transfer functions according to (2.65).

$$\Delta P(s) = \frac{\frac{k_g}{T_a}}{s^2 + \frac{k_d}{T_a}s + \frac{k_g}{T_a}} \Delta P_o(s) + \frac{\frac{k_g}{T_a}k_d}{s^2 + \frac{k_d}{T_a}s + \frac{k_g}{T_a}} \Delta\omega_{PLL} \tag{2.65}$$

It can be noted that by assuming a constant PLL frequency during power reference change, (2.62) is obtained.

To achieve the exact transfer function relating electric power delivered with the power reference $\frac{\Delta P(s)}{\Delta P_o(s)}$, the transfer function $\frac{\Delta\omega_{PLL}}{\Delta P_o(s)}$ should be calculated. Achieving such a transfer function is complex. Moreover, it will result in a very high order transfer function for $\frac{\Delta P(s)}{\Delta P_o(s)}$ that is difficult to tune theoretically. Alternatively, the Simulink model implemented will be taken as a reference for the exact model. For comparison, the response of both the simplified model and the exact model, implemented in Simulink, are presented in Figure 2.21.
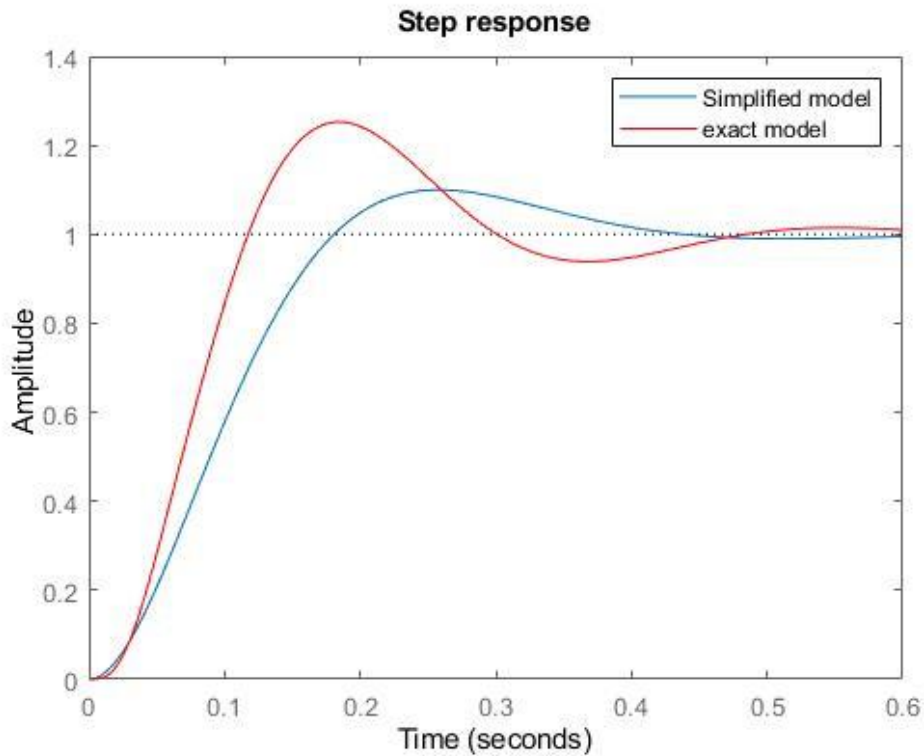
Figure 2.21. Step response of active power controller Simplified model from transfer function and exact model from Simulink

It is very clear that the two models are characterized by different responses. In fact, the overshoot in the exact model is around 17% more than the simplified one. For this reason, the drag coefficient, tuned using the simplified model, is not expected to follow the requirements defined for its tuning.

Instead, the drag coefficient obtained from tuning will be operated as a starting reference for the exact model. Then, the value of the drag coefficient will be increased gradually, until the requirements are followed. Furthermore, a slight change in the definition of requirements is obligatory, where a maximum overshoot of 10% will be required for the minimum SCR instead. The reason is that the PLL dynamics are the highest at the minimum SCR, thus resulting in the maximum overshoot during minimum SCR.

The drag coefficient, experimentally tuned in the Simulink model, is defined by (2.66), achieving an overshoot of around 10% at minimum SCR, which corresponds to 1.5.

$$k_d = 300 \ pu \tag{2.66}$$

This value of drag coefficient is the minimum value of drag that could be used for the VSM as it exactly reaches the maximum defined overshoot. The drag coefficient can be set to be more than 300, decreasing the overshoot more. However, this results in a slower response. Hence, the drag coefficient value that will be used is the one defined by (2.64) since it achieves the required overshoot with the fastest response.
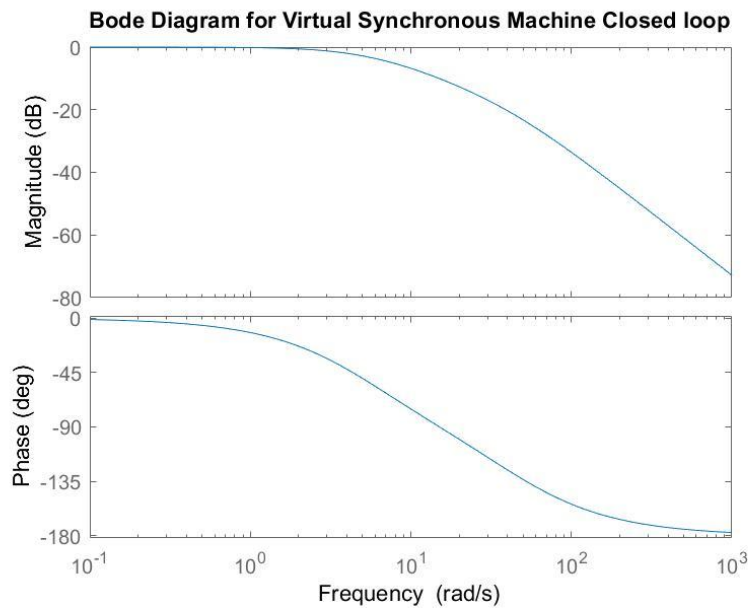
Figure 2.22. Bode plot of the active power controller closed loop

The bode plot of the active power controller closed loop is shown in Figure 2.22. This bode diagram is obtained from the simplified model using the tuned drag coefficient and time constant achieved in (2.66) and (2.61) respectively. The bandwidth of the VSM is around 5 rad/s. However, this bandwidth is for the simplified model without introducing PLL dynamics. In that case, the bandwidth of the exact model is estimated to be around 10 rad/s. Accuracy here is not the problem, but the objective is to point out how small the bandwidth of the active power controller of the VSM is compared to voltage and current controllers. Having that huge difference ensures that the dynamics of these controllers will not interact with the main controller (active power controller). This effect is essential to obtain fast settling time, lower overshoot, and a stable system.

2.3.7. Summary of Parameters

In the following Table 2-2, a summary of parameters obtained for the tuning of each controller in the virtual synchronous machine is listed. Also, the values of the base quantities used in the tuning will be listed in the same table.

Table 2-2. parameters values for all controllers used in VSM.

Parameters	Values	Parameters	Values
Base Primary Voltage [V_b]	690 [V]	V.C Proportional gain [$K_{p,v}$]	0.6427 [pu]
Base Primary Current [I_b]	1.674 [kA]	V.C Integral gain [$K_{i,v}$]	241.0256 [pu]
Base Primary Impedance [Z_b]	0.2381 [pu]	V.C design parameter [a]	4
Base angular frequency [ω_b]	314.16 [rad/s]	PLL proportional gain [$K_{p,PLL}$]	0.791 [pu]
Filter resistance [$r_{1,f}$]	0.0132 [pu]	PLL integral gain [$K_{i,PLL}$]	81.44 [pu]
Filter inductance 1 [$l_{1,f}$]	1.32 [pu]	PLL filter [$T_{f,PLL}$]	1.667 [ms]
Filter inductance 2 [$l_{2,f}$]	0.0053 [pu]	PLL design parameter [a]	2.41
Filter capacitance [c_f]	0.0718 [pu]	Reactive power filter [T_p]	10 [ms]
C.C proportional gain [$K_{p,c}$]	25.205 [pu]	Reactive power droop [m_q]	0.1 [pu]
C.C integral gain [$K_{i,c}$]	79.18 [pu]	VSM Time Constant [T_a]	6.25 [pu]
C.C Time Constant [T_C]	0.2 [ms]	VSM Active Damping [K_d]	300 [pu]
Virtual Inductance [l_v]	0.2 [pu]	Virtual Resistance [r_v]	0

3 Dynamic Simulations for Virtual Synchronous Machine

This Chapter introduces the dynamic simulations performed on MATLAB Simulink. The simulations are divided into three main tests, which are step change in load, step change in frequency, and a constant rate of change of frequency for inertial response test. These tests will be carried out under the same short circuit ratio and same tuned parameters.

At the beginning of the chapter, the model implementation will be presented, followed by the results achieved from running the simulation. Finally, the effect of changing the short circuit ratio on the system transient response is clarified.

3.1. Simulink Model

The Simulink Model implemented for dynamic simulations models the physical system found in Fig. 3.1, which is adapted from Fig. 2.1. The model is mainly composed of three blocks. The first block, Firmware, includes the control representation of the inverter. It has all the controllers including inner current controller, outer voltage controller, phase locked loop, virtual impedance, reactive power controller, active power controller. The general scheme of firmware is exactly similar to Figure 2.2, which was introduced before, where the inertia emulation block from Figure 2.2 is described by the virtual synchronous machine diagram of Figure 1.15.

The second block, physical system, is composed of the average model of the inverter and the circuit schematic that is presented in Figure 3.1. Figure 3.2 shows the average model used for the inverter representation for a single phase. The third block, the grid, is just implemented as an ideal three phase voltage source with nominal frequency

along with grid resistance and inductance, which depends on the short circuit ratio of the grid.
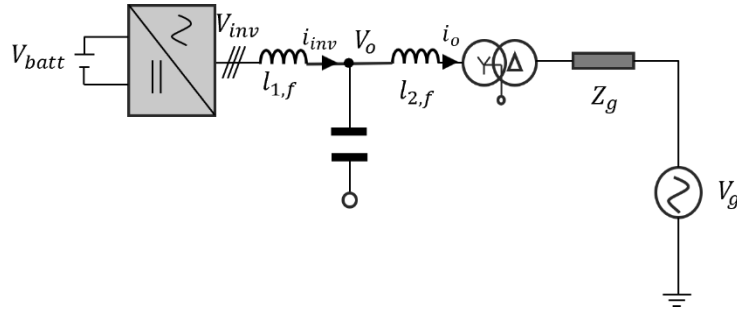
Figure 3.1. Physical System implemented for simulation in Simulink.
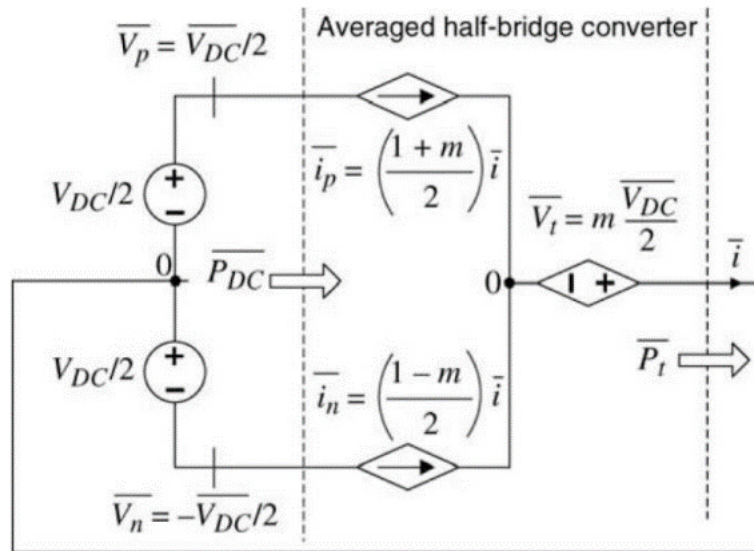
Figure 3.2. Average model of the inverter

In Figure 3.2, V_{DC} represents the battery voltage, V_t is the inverter terminal voltage, while m is the modulation index.

The summary of parameters used for the circuit schematic of the inverter topology block as well as the parameters of the grid block are shown in the following table.

Table 3-1. Values of parameters used in circuit schematic of inverter topology in Simulink.

Parameters	Values	Parameters	Values
Battery Voltage [V_{batt}]	1300 [V]	Filter Resistance 2 [R_{2f}]	$12.56*10^{-6}$ [ohm]
Nominal Frequency [f_n]	50 [Hz]	Filter Capacitance [C_f]	$960*10^{-6}$ [F]
Grid Voltage [V_g]	15 [kV]	Inverter Rated Power [S_n]	1 [MVA]
Short circuit ratio	10	Transformer Rated Power [S_T]	1 [MVA]
Grid Resistance [R_g]	0.0356 [ohm]	Transformer primary Voltage [V_n]	690 [V]
Grid Inductance [L_g]	1.119 [H]	Transformer Secondary Voltage [V_s]	15 [kV]
Grid Initial Phase [θ_g]	30 [deg]	Transformer reactance [X_T]	0.06 [pu]
Filter Inductance 1 [L_{1f}]	$1000*10^{-6}$ [H]	Transformer resistance	0.003 [pu]
Filter Inductance 2 [L_{2f}]	$4*10^{-6}$ [H]	Transformer connection	$Y - \Delta$
Filter Resistance 1 [R_{1f}]	0.0031 [ohm]		

3.2.   Dynamic Behavior for a change in Power Setpoint

The first test performed on the virtual synchronous machine is changing the power setpoint of the VSM. The objective is to test how fast the electric power follows that setpoint change along with the overshoot. The change in power setpoint is defined by the following standards:

- The power setpoint is defined by a step change from 0 to 1 per unit.
- The step change will be performed after 1 second of simulation time, while the total simulation time is 3 seconds.
- The frequency of the grid is kept constant at nominal value, corresponding to 50 Hz, which is equivalent to 1 per unit.
- The Voltage of the grid is kept constant at the rated value 15 kV, defined in table 3-1.
- The short circuit ratio is constant and defined to be of a value of 10.

These standards are designated to solely investigate the electric power response to a step change in setpoint. Any other perturbations in terms of frequency or voltage will affect the dynamic behavior of power, hence it is not possible to accurately test the tuned parameters.

The first outcome is achieved in Figure 3.3 showing the transient response of electric power towards a step change in power setpoint. The power reaches its settling value of 1 per unit in around 0.5 second without any overshoot or steady-state error, meaning the response is overdamped with a short circuit ratio of 10. This is somehow expected since the tuning is supposed to achieve a 10% overshoot around the minimum short circuit ratio, which corresponds to 1.5. Hence, increasing the short circuit ratio will decrease the overshoot until the response will be overdamped at high short circuit levels.
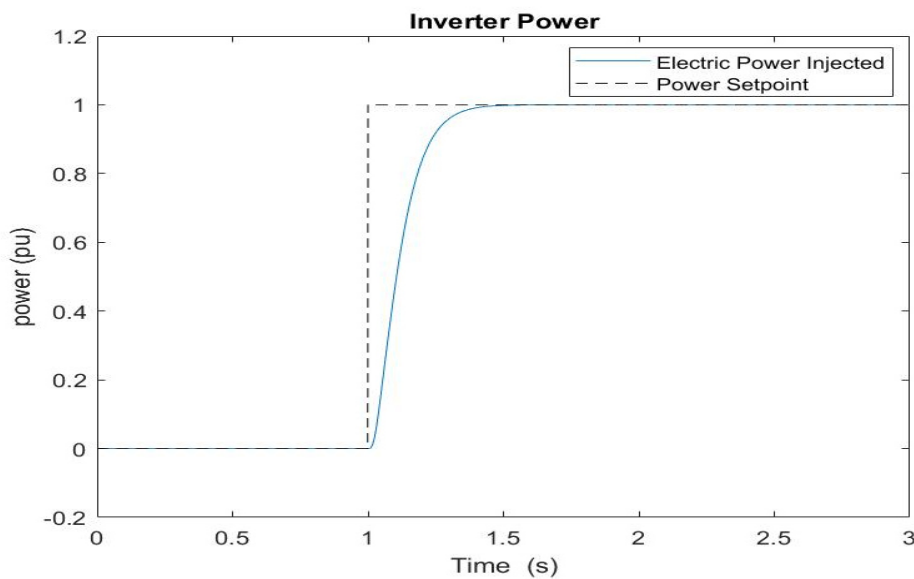
Figure 3.3. VSM injected power during a step change in power setpoint.

That increasing change in electric power is caused by the acceleration of the virtual synchronous machine. The difference between electric power and power setpoint stimulates the increase of virtual speed of the virtual synchronous machine, allowing the increase of electric power injected to the grid by increasing the angle difference between the inverter and the grid as shown before in (2.42). Thus, the virtual speed response is shown in Figure 3.4.
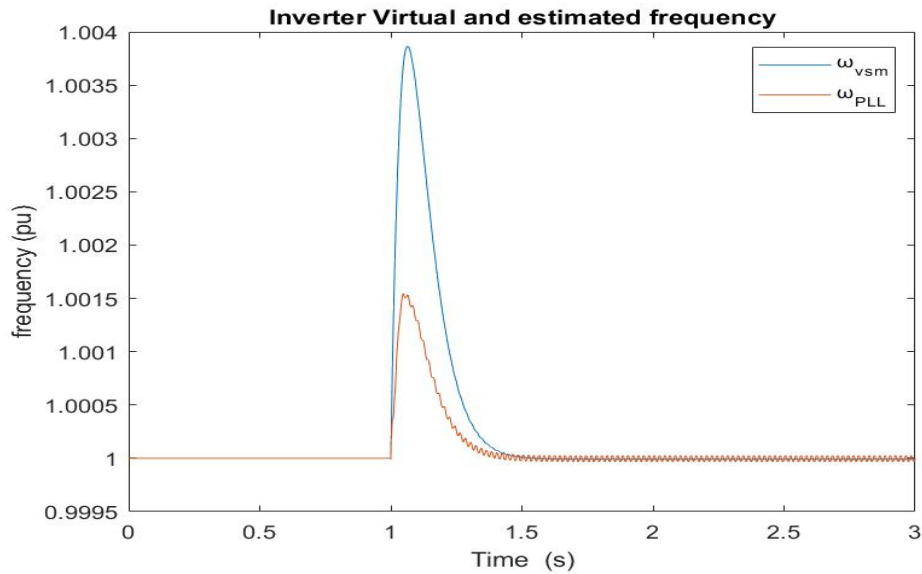
Figure 3.4. VSM virtual and estimated frequency during a step change in power setpoint.

The increase in virtual speed of VSM is very low as described in Figure 3.4 due to having a large drag coefficient that contributes to decreasing the acceleration or declaration of the virtual synchronous machine. Obviously, the frequency reaches its nominal value by the time the active power reaches the power setpoint. Moreover, the estimated frequency by the PLL was also shown in Figure 3.4. It can be seen that also the estimated frequency shows a rise during the step power setpoint change. Hence, a change in power setpoint can actually drive the reference frequency to also change. This is the phenomenon that was pointed out in section 2.3.6 during the tuning of drag coefficient. Because of that, during the tuning of drag coefficient, it was not possible to assume the reference frequency is constant, thus the tuning was achieved experimentally.

It can be observed that having an increase in the frequency measured by the PLL during power setpoint step will decrease the difference between the virtual and estimated frequency. As a result, the drag power term will also decrease (refer to Fig. 2.20). This can be considered as a minimization of the drag coefficient effect instead. In other words, it is as if the drag coefficient, not the difference between grid and VSM frequencies, decreased, leading to the same reduction in damping power. Hence, the effect of PLL dynamics will result in a reduced drag coefficient, which is why the tuned drag coefficient in section 2.3.6 was increased experimentally to cancel that effect.

The current and voltage controllers' response is shown in Figures 3.5 and 3.6. The voltage references are affected by the virtual impedance block, which is a function of grid current. It should be noted that the voltage graph in direct axis and current graph in quadrature axis are similar, while the voltage graph in quadrature axis and current graph in direct axis are opposite. This is caused mainly by the coupling terms in the current controller. Moreover, both controllers react fast in following their references compared to the active power controller, resulting in decoupled dynamics and a stable response.
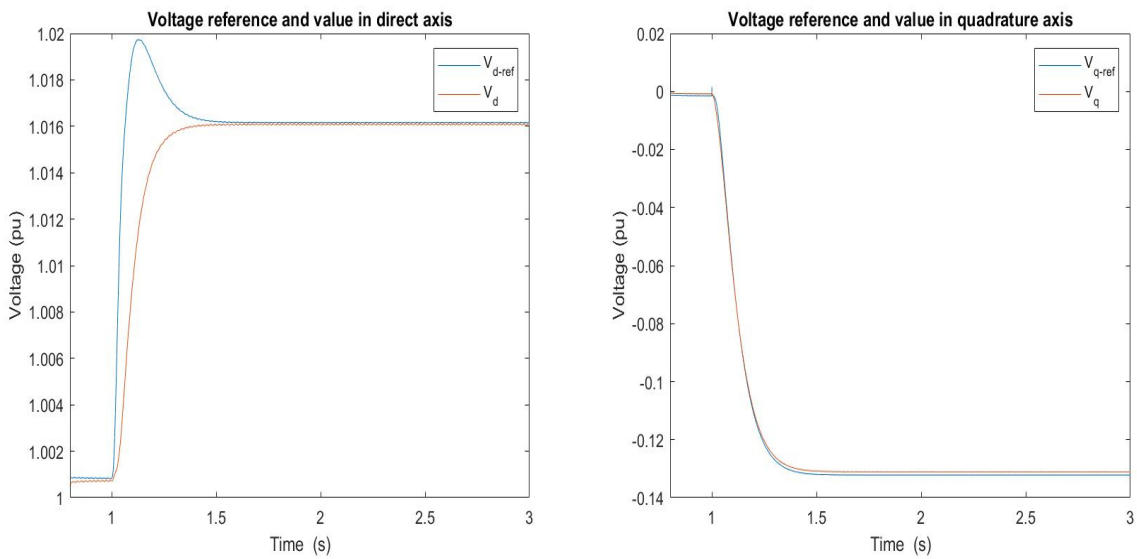
Figure 3.5. Voltage reference and measured values in direct and quadrature axis during power setpoint step change.
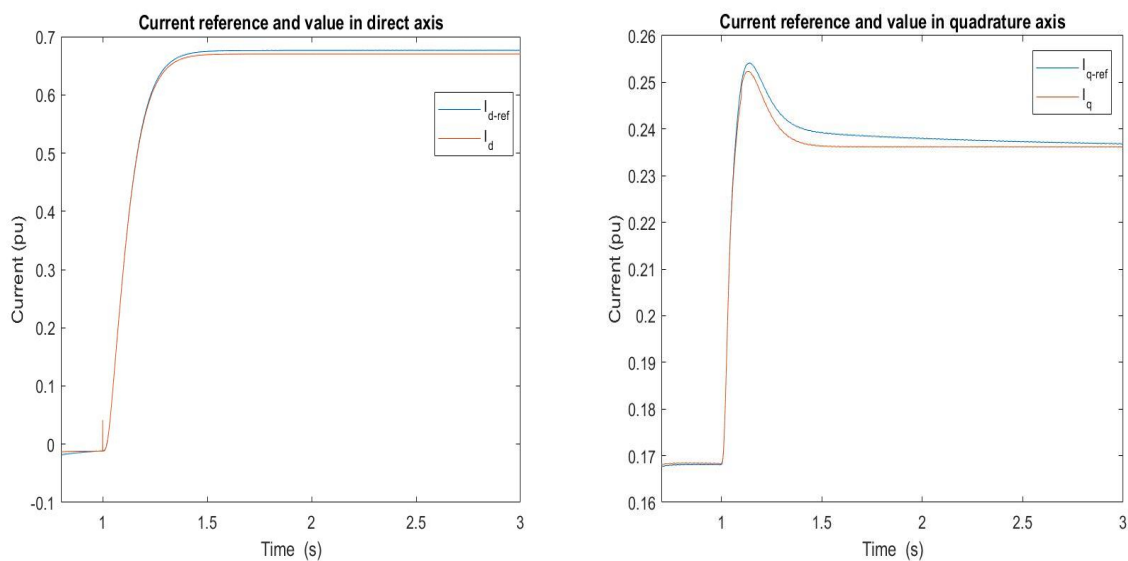
Figure 3.6. Current reference and measured values in direct and quadrature axis during power setpoint step change.

3.3. Dynamic Behavior for a change in Frequency

The second phase of testing is concerned with the frequency of the grid. The goal is to find out if the inverter keeps its synchronization with the grid. This frequency test is described accordingly:

- The frequency of the grid will follow a step change from 1 per unit to 0.98 per unit after 1 second of simulation.
- The power setpoint during the frequency test is set to 0.
- The short circuit ratio is constant, and its value corresponds to 10.
- The voltage of the grid is kept constant at 15 kV.

After applying the previous criterion, the results concerning the frequency of the virtual synchronous machine are obtained in Figure 3.7. The inverter successfully follows the grid frequency in about 0.5 seconds, which is very similar to the settling value of power since both variables are correlated, where a change in frequency causes a change in power and vice versa, so both of these variables must settle together. Also, the frequency response develops an overshoot of around 12.5% because of the fast inertial response achieved and the PLL dynamics, which is shown in Figure 3.8. The faster the response the higher that overshoot should be.
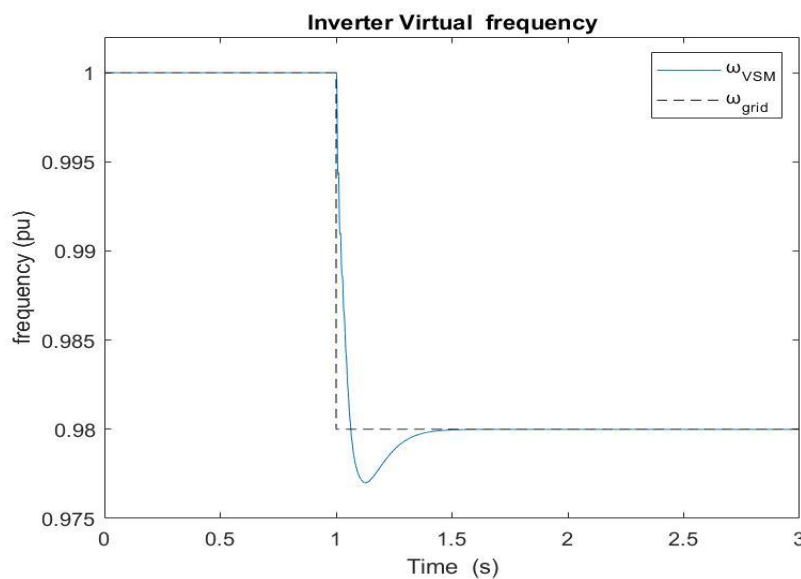
Figure 3.7. VSM virtual frequency during a step change in grid frequency.

It shall be noted that the overshoot in frequency is essential for reaching stability as the power will keep rising until the frequency is reduced to be less than the grid frequency. In that case, the grid starts pulling the virtual machine back to the correct value by reducing the electrical power until acceleration of the machine occurs again with the help of drag power. In the end, the virtual machine accelerates to the grid frequency, following the power setpoint and in synchronization with the grid.
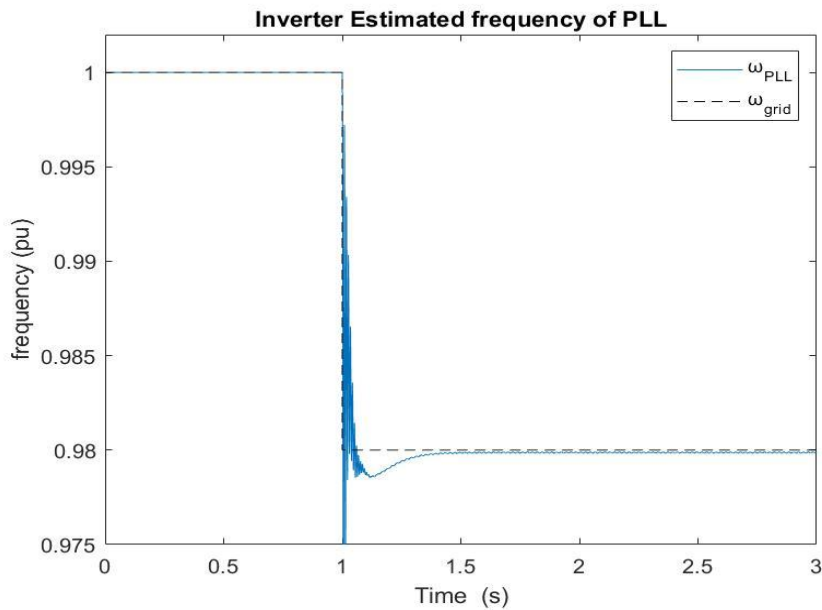
Figure 3.8. VSM estimated frequency during a step change in grid frequency

As a consequence of having a large time constant, the virtual synchronous machine participates with a relatively large amount of inertial power during the grid frequency change with the aim to decrease the ROCOF and frequency nadir of the system. This shows the grid support capability of the VSM inverter and how it can support the grid frequency with its virtual inertia like a synchronous generator. However, unlike a synchronous generator, the time constant needs to be tuned carefully to avoid reaching the current saturation of the inverter. Also, it can be noticed as stated before that this inertial response settles after 0.5 seconds when the inverter is perfectly synchronized with the grid.

Moreover, in Figure 3.9, the maximum power reached because of the virtual synchronous machine inertia is around 0.8 per unit. This value is reached in less than 0.1 seconds. Thus, it can be concluded that a step frequency change drives the power to change much faster than the setpoint step.
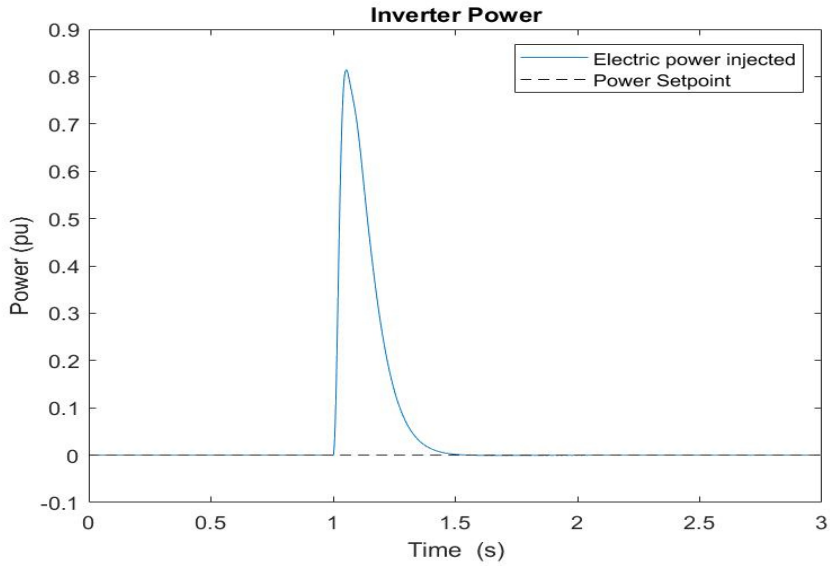
Figure 3.9. VSM injected power during a step change in grid frequency

The current and voltage responses are then described by Figures 3.10 and 3.11. These graphs inherit the same features described before, where the voltage in d-axis is similar to current in q-axis, while voltage in q-axis is opposite to current in d-axis. It can be noted that both the direct and quadrature components of the voltage come back to the same value before the frequency disturbance meaning that the angle at the capacitor voltage is restored to its previous value, which reflects the injection of no power into the grid.
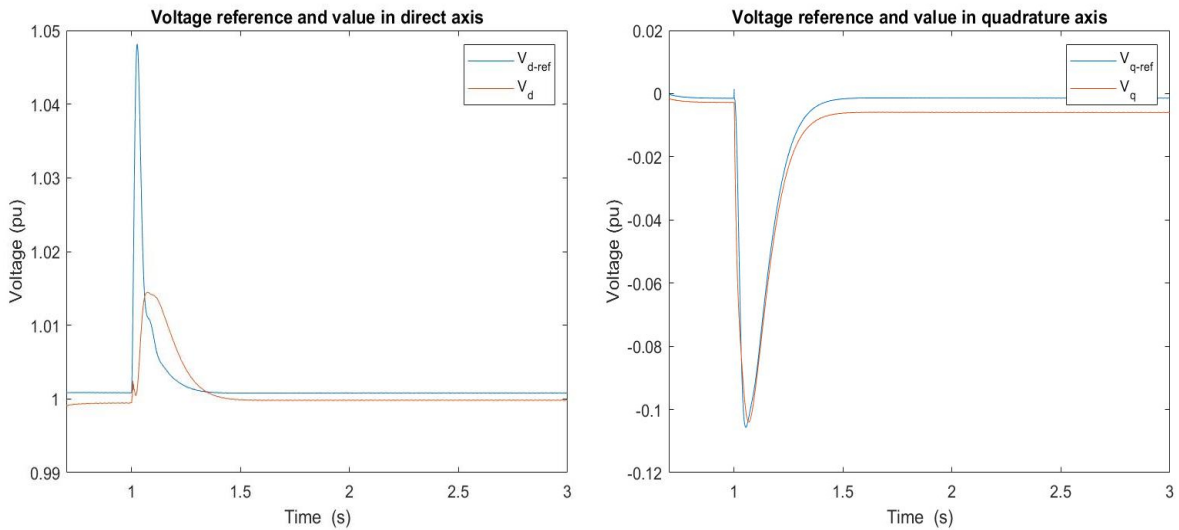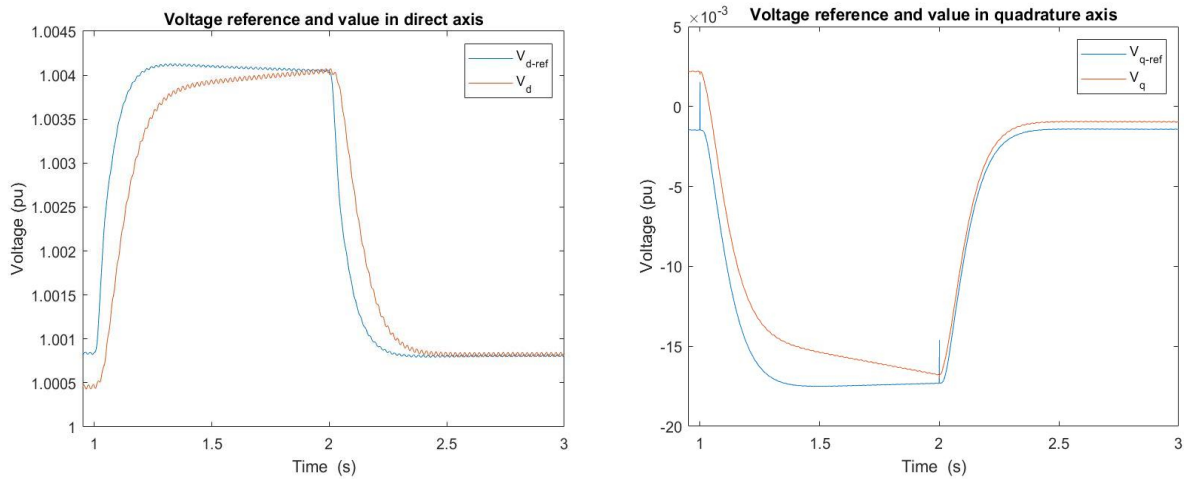

Figure 3.10. Voltage reference and measured values in direct and quadrature axis during grid frequency step change.
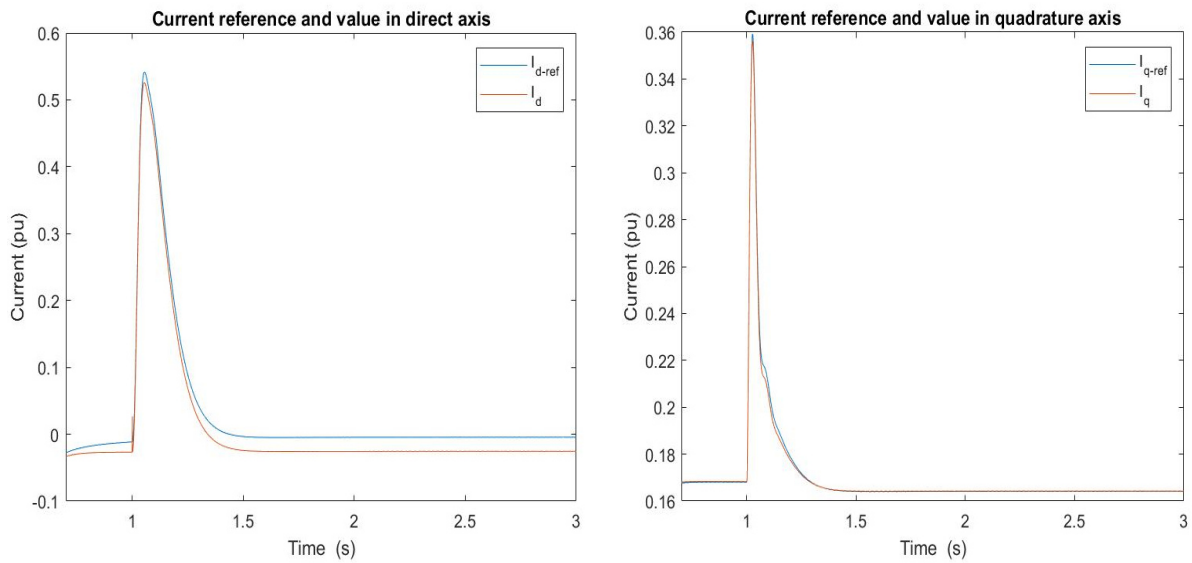
Figure 3.11. Current reference and measured values in direct and quadrature axis during grid frequency step change.

3.4. Inertial response for a ROCOF event

This section is focused on testing the inertial response of the virtual synchronous machine. The VSM was tuned in section 2.3.6 with a time constant following a required inertial response. The virtual machine is supposed to provide a change in electric power corresponding to 0.125 per unit for each change in frequency of 1 Hz/s. To validate such behavior, the virtual synchronous machine is simulated on MATLAB with the following conditions:

- The frequency of the grid is ramped down with a rate of -1 Hz/s after one second of simulation.
- The frequency is saturated after 1 second of ramping, meaning the ramping is stopped at second 2 of simulation and the frequency remained constant at a value of 0.98 per unit.
- The power setpoint is set to zero throughout the whole simulation.
- Both short circuit ratio and grid voltage are constant with the same value as previous tests.

The model was simulated with the previous requirements and the inverter power is shown in Figure 3.12. The inverter successfully provided the amount of inertial power required with a transient response almost identical to the power setpoint step test.

This is mainly because the test is focused on having a power change, inertia, like the step power setpoint test, while the frequency is being changed very slightly with the ramp behavior, thus its effect on the dynamic response is not significant. Unlike the step frequency test, the step change in frequency causes the power to rise very fast, allowing the power response to rise more quickly than the step power and ROCOF tests.

This can be explained more from (2.65), which is recalled in (3.1).

$$\Delta P(s) = \frac{\frac{k_g}{T_a}}{s^2 + \frac{k_d}{T_a}s + \frac{k_g}{T_a}}\Delta P_o(s) \; + \frac{\frac{k_g}{T_a}k_d}{s^2 + \frac{k_d}{T_a}s + \frac{k_g}{T_a}}\Delta\omega_{PLL} \tag{3.1}$$

The transfer functions of electric power with respect to PLL frequency and power setpoint are almost identical. The only difference is that the PLL frequency transfer function is multiplied by drag coefficient. As a result, changes in frequency and power have the same dynamics due to having same poles. However, according to final value theorem in control theory, the power will settle at a value equal to drag coefficient for a step frequency change as shown in (3.2), while it will settle at 1 for a step power change as shown in (3.3), with exactly same dynamic behavior.

$$\lim_{s\to 0} G(s)_{\Delta P(s),\Delta\omega_{PLL}} = \lim_{s\to 0} \frac{\frac{k_g}{T_a}k_d}{s^2 + \frac{k_d}{T_a}s + \frac{k_g}{T_a}} = \frac{\frac{k_g}{T_a}k_d}{\frac{k_g}{T_a}} = k_d \tag{3.2}$$

$$\lim_{s\to 0} G(s)_{\Delta P(s),\Delta P_o(s)} = \lim_{s\to 0} \frac{\frac{k_g}{T_a}}{s^2 + \frac{k_d}{T_a}s + \frac{k_g}{T_a}} = \frac{\frac{k_g}{T_a}}{\frac{k_g}{T_a}} = 1 \tag{3.3}$$

As a consequence, the power will change with much higher values in case of a step frequency perturbation compared to a step power setpoint one. Of course, the step frequency change in that case is not equal to one per unit. However, it is equivalent to 0.02 per unit. Still, the electric power change corresponding to such a step has higher values than the step power change, leading to a faster change in electric power. It should be noted that the change in electric power due to a step frequency change does not exceed the inverter limits because of the grid synchronization that helps in limiting that power change, which cannot be observed from the transfer function modeling.
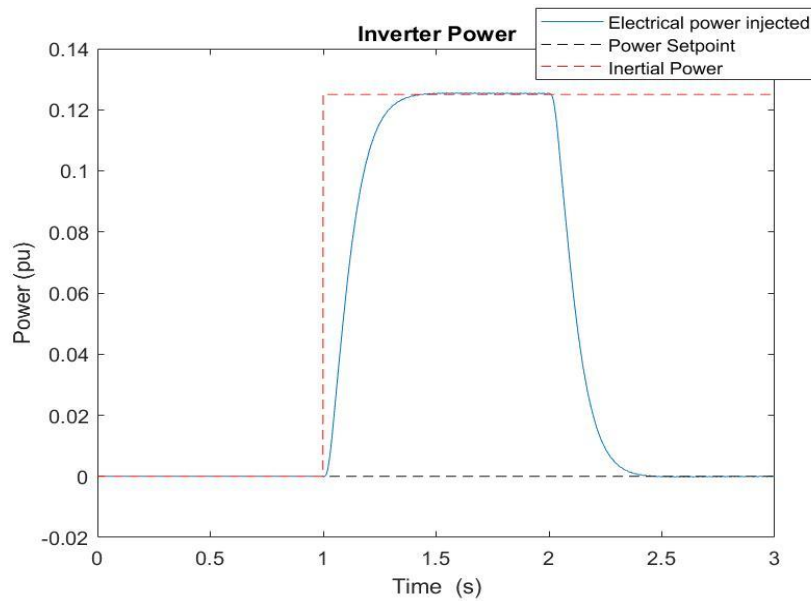
Figure 3.12. VSM injected power during a ROCOF event

The PLL estimated frequency and the virtual frequency can be observed following the grid frequency in Figure 3.13. The PLL doesn't exactly reach the grid frequency at 0.98 per unit after saturating the frequency since the integrators are not working properly in the Simulink model, where continuous integrators were implemented for a discrete time simulation. In this case, the steady-state error does not reach exactly zero.
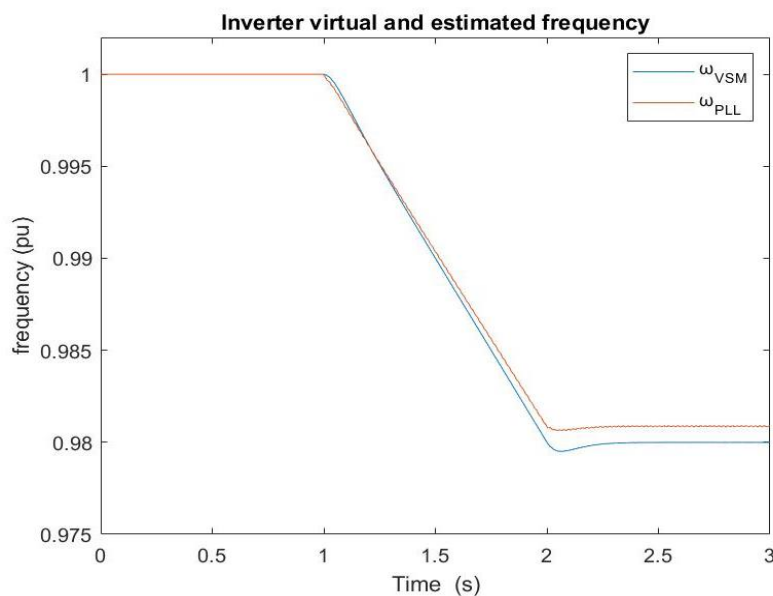
Figure 3.13. VSM virtual and estimated frequencies during a ROCOF event.

In Figures 3.14 and 3.15, the dynamic responses of the voltage and current controllers are observed. Both controllers have the same characteristics as in the previous tests.

The voltage controller is acting very slow in following the references during the ROCOF test, but it tends to act faster after the saturation was implemented. On the other hand, the current responds very fast to any changes to its reference values during the whole test because it inherits a large bandwidth. In both cases, the steady-state errors are not exactly zero since this is a discrete simulation as mentioned before and the values along the y-axis are very small.

Figure 3.14. Voltage reference and measured values in direct and quadrature axis during ROCOF event.
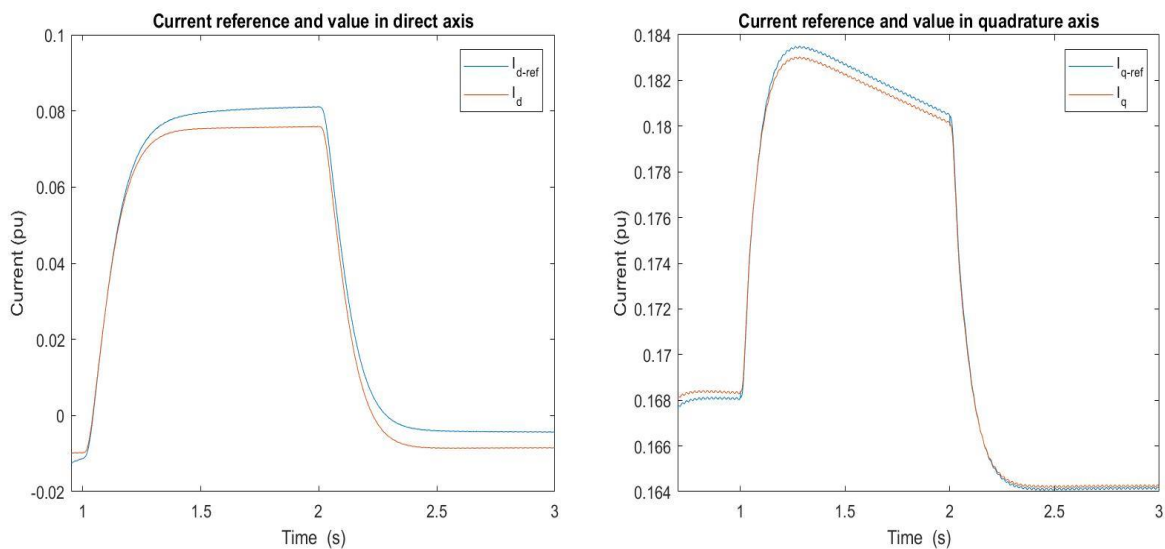
Figure 3.15. Current reference and measured values in direct and quadrature axis during ROCOF event.

3.5.   Short Circuit Ratio effect on response dynamics

In the previous sections, it was clearly stated during each test criteria that the short circuit ratio is constant. Furthermore, during the tuning of drag coefficient, it was mentioned that the maximum short circuit ratio is considered for the tuning. The short circuit ratio affects the dynamic response of the virtual synchronous machine; thus, it was important to keep it constant during previous tests to properly investigate the impact of other variables on the dynamics.

The short circuit ratio determines the grid inductance and resistance. The relationship between them is inversely proportional, so a low short circuit ratio will correspond to a high value of inductance and resistance. Then, the factor k_g that was introduced in (2.59) is directly proportional to the short circuit ratio.

The short circuit ratio is essential in determining the dynamic response of the VSM since it is included in the active power controller transfer function in (2.65). Thus, changing such a variable can lead to a different response in terms of speed and overshoot. Ideally, it is expected that an increase in SCR should lead to a faster response with a higher overshoot. However, it should be mentioned that the SCR is also effective over the PLL. The dynamics of PLL tend to increase as it works in lower short circuit levels, impacting the effect of drag power more. As explained before, this can be seen as having less drag coefficient.

As a consequence, the virtual synchronous machine model is simulated under the effect of different short circuit ratios to precisely observe its influence on the transient behavior. The test standards are defined as follows:

- The Short circuit ratio will be varied during the defined three tests in previous sections, which are step power setpoint, step frequency of the grid, and ROCOF even.
- The short circuit ratio values selected for tests performing are 1.5, 3, 10, 20, and 50.
- The step power test is defined similar to section 3.2. However, the test starts after 2 seconds of simulation and total time of simulation is 4. Of course, the short circuit in that case is not constant and will be varied according to value of defined range.
- The step frequency test standards are the same as section 3.3. The only difference is that the test starts after 2 seconds of simulation and total simulation time is 5.

- The ROCOF test is similar to section 3.3. But the test begins at the second 2 of simulation and the frequency is saturated after three seconds, hence saturation happens at time equals to 5 in simulation. The frequency in that case is saturated at 0.94 per unit, and the total simulation time is 7 seconds.

According to the previous requirements, the step power setpoint test was reperformed using the simulation time and short circuit levels defined to obtain Figure 3.16, showing different electric power dynamic responses along with virtual frequency of the virtual synchronous machine for a step power setpoint change at various short circuit ratios.
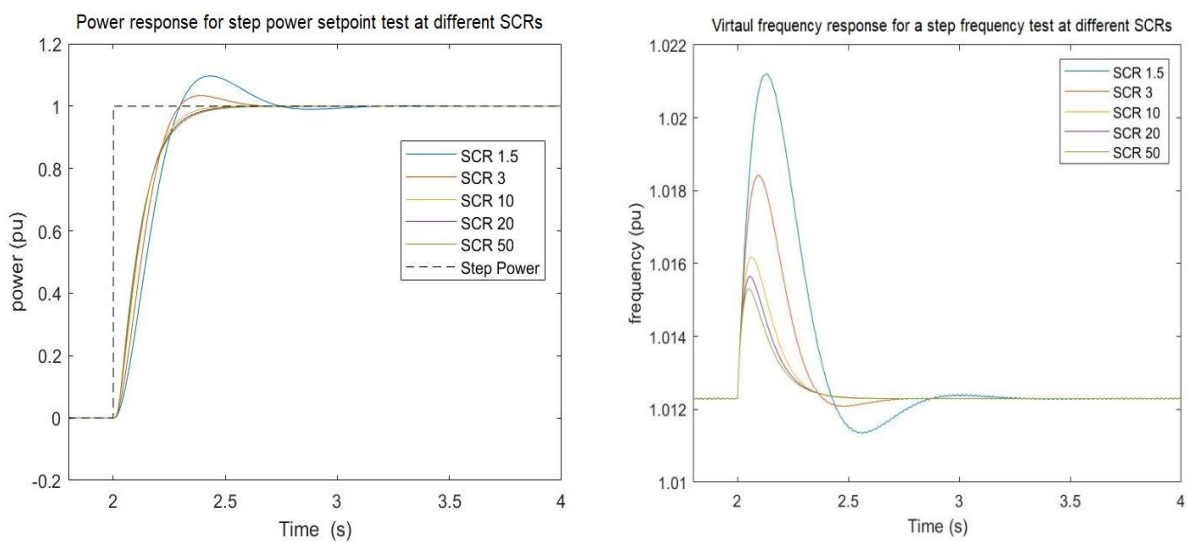
Figure 3.16. The Figure on left describes the power injected by VSM during a step power setpoint change under different short circuit ratio values, while the Figure on the right describes the virtual frequency of VSM for power setpoint step change under various SCRs.

During low values of short circuit ratios, the dynamic response of electric power acts slower, taking more time to rise and settle. The difference between the rise time for different short circuit values is not much and can be neglected. However, the main issue rises as the amount of overshoot increases as the short circuit value decreases, exhibiting an inversely proportional relationship between them. As explained before, this means that the PLL dynamics are also affected by the variation of short circuit value causing the system to overshoot. However, more clarification is needed to explain why the system is not responding faster when the overshoot is increased as in that case the PLL dynamics should have reduced the effectiveness of the drag power allowing for a faster response. For a further investigation, the estimated frequency measured by PLL is plotted as shown in Figure 3.17.
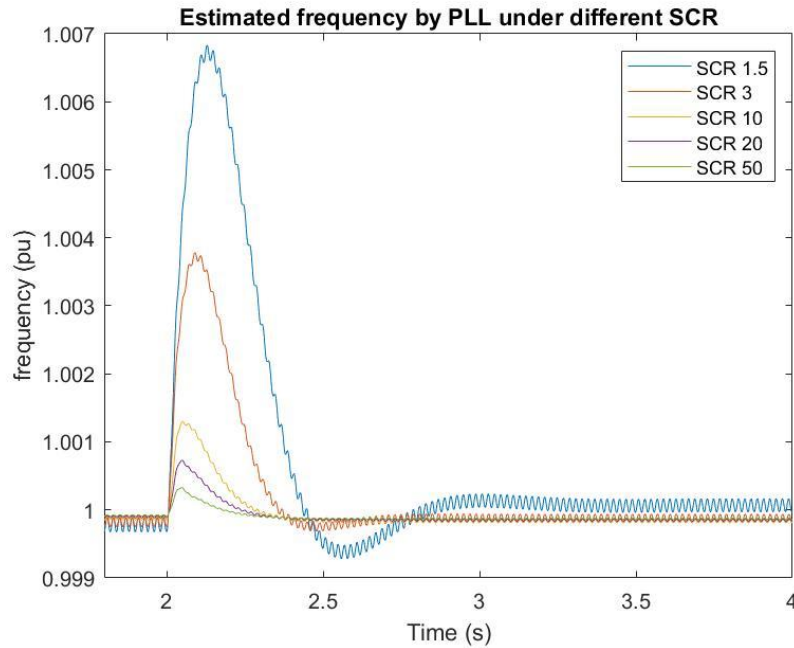
Figure 3.17. Estimated frequency by PLL during step power setpoint test for different SCR.

The PLL obtained in Figure 3.17 shows that the dynamics are getting slower with more overshoot as the short circuit value is reduced. This explains the transient behavior of inverter power. At the beginning of simulation, the PLL frequencies at different SCRs are close in values because of the slower response effect of decreasing the SCR. Hence, the grid in this case dominates the response forcing the power to change slowly with low SCR. Then, after some time, the estimated frequencies start reaching their overshoot values and the PLL starts affecting the response more than the grid by reducing the drag power effect, allowing power to change faster, and causing a higher overshoot.

The step frequency and ROCOF test were also reanalyzed under different short circuit ratios. The dynamic behavior is described in Figures 3.18 and 3.19 respectively. In Figure 3.18, The power participating in the inertial response showing a declining behavior as the SCR value is dropped since the response is faster with high short circuit ratios. Following that, the power reaches the setpoint value with an overshoot in low SCR values as a consequence of the affected PLL dynamics.

The ROCOF test in Figure 3.19 shows exactly the same change in dynamic behavior, caused by varying SCR, as the step power setpoint test. The inverter is able to provide the required inertial power, specified in the tuning according to regulations, through all short circuit levels.
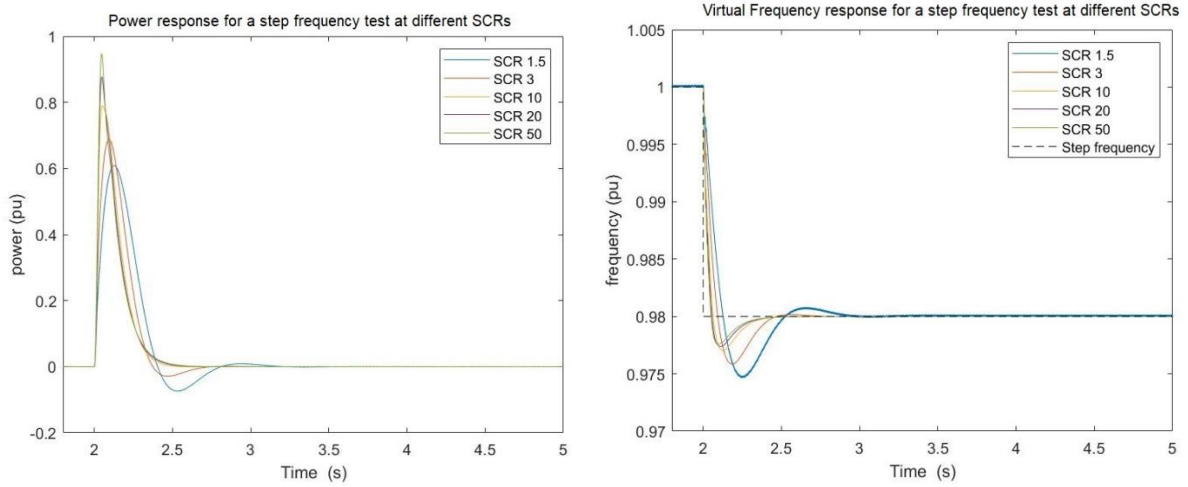
Figure 3.18. The Figure on left describes the power injected by VSM during a step grid frequency change under different short circuit ratio values, while the Figure on the right describes the virtual frequency of VSM for grid frequency step change under various SCRs.
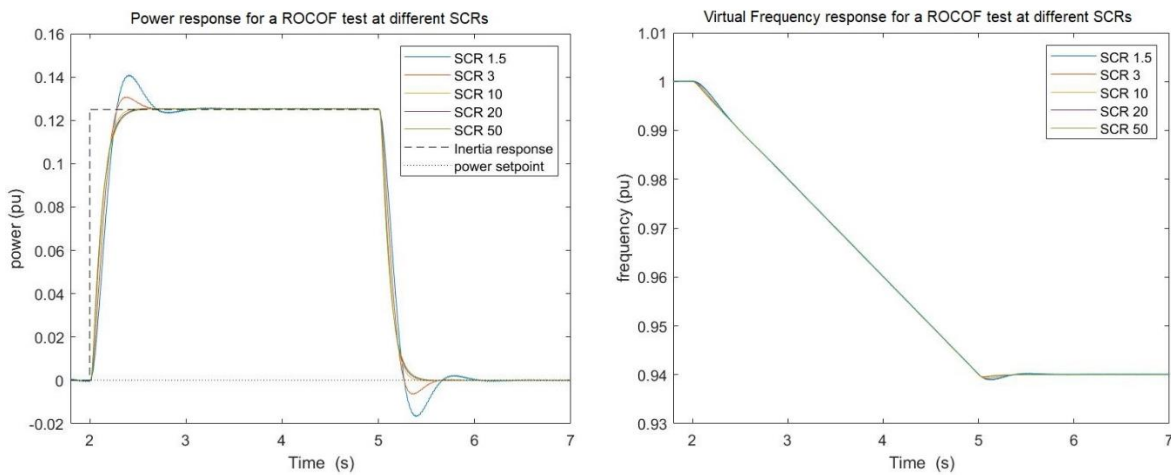
Figure 3.19. Figure 3.20. The Figure on left describes the power injected by VSM during ROCOF event under different short circuit ratio values, while the Figure on the right describes the virtual frequency of VSM for ROCOF event under various SCR values.

4 Generalized Virtual Synchronous Generator

This chapter introduces a new control topology, derived from the virtual synchronous machine. The new control method is called Generalized Virtual Synchronous Generator (GVSM), presented to enhance the transient response of the VSM. The chapter explains the control schematic used for the GVSG followed by the tuning criteria. Different tunings will be investigated to achieve the best dynamic behavior for the inverter.

The Chapter concludes with presenting another control methodology, developed from GVSG, called compensated generalized virtual synchronous machine, along with its schematic and tuning basis.

4.1. Converter Control Schematic

The same case study used for VSM will be adapted for GVSG, so the line diagram for the inverter can still be represented by Figure 2.1. The complete control structure for GVSG is defined by Figure 4.1. The control structure is very similar to the one presented for VSM in Figure 2.2. The main difference between the two control methods is the implementation of the active power controller (inertia emulation block). The block diagram of the active power controller for GVSG is presented by Figure 4.2, while the VSM one was shown previously in Figure 1.15. It can be observed that the representation of the active power controller for GVSG is very similar to the VSM. An extra zero and pole are added with the time constant coefficient described by coefficients a and b respectively. The time constant is presented by variable c in that case instead of T_a.

Moreover, another difference between the two control methods is that a PLL is not necessary for GVSG since the transient behavior can be controlled by the extra zero and pole added with the active power controller. Instead, a constant reference

frequency is used, thus the droop coefficient D_P (refer to Figure 4.2) is presented rather than drag coefficient k_d.
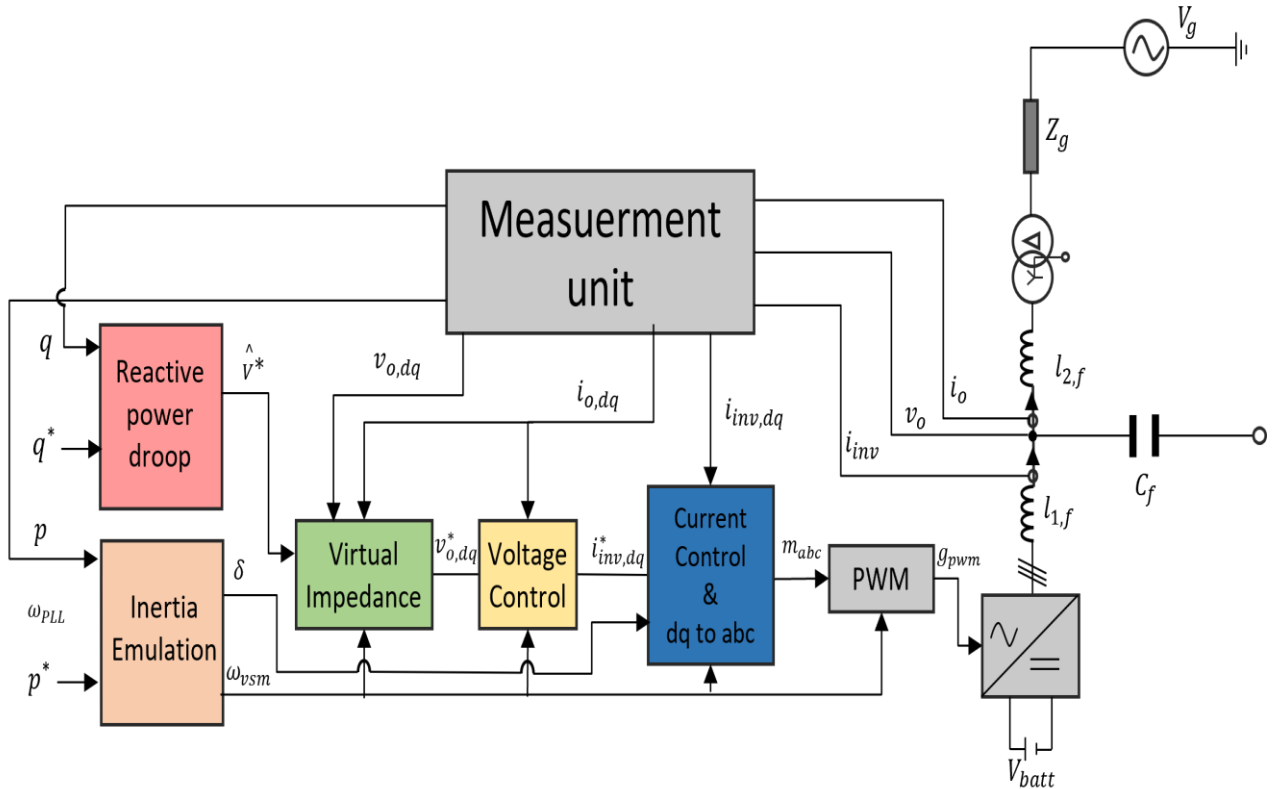
Figure 4.1. Complete control model schematic for GVSG and CGVSG
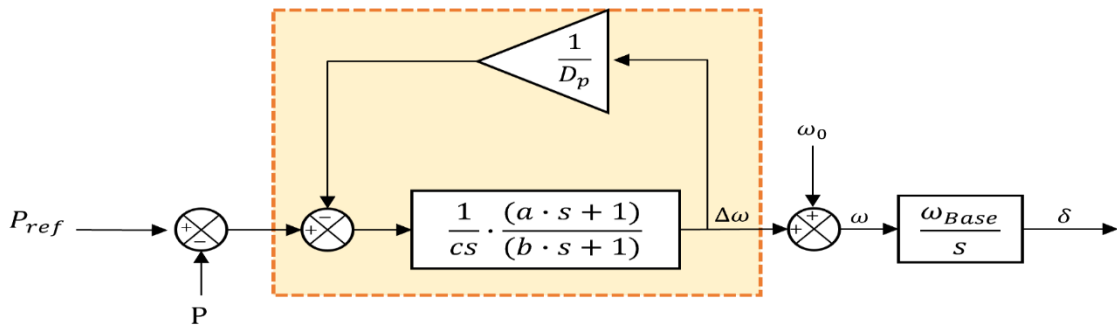
Figure 4.2. Inertia emulation block representation for GVSG

The GVSG has the same controllers used for the VSM and applied to the same case study with circuit line diagram represented in Figure 2.1. For this reason, the tuned parameters achieved in the VSM control section for the inner current controller, outer

voltage controller, virtual impedance, and reactive power controller will also be used for GVSG. Only the tuning of active power controller will be investigated.

4.2. Active Power Controller Tuning

As mentioned in the previous section, the tuning analyzed is concerned with the active power controller only. The closed loop diagram of the active power controller for the GVSG can be represented according to Figure 4.3 [4]. Obviously, it is also similar to Figure 2.20 of VSM with an extra zero and pole added with the time constant (coefficient c).
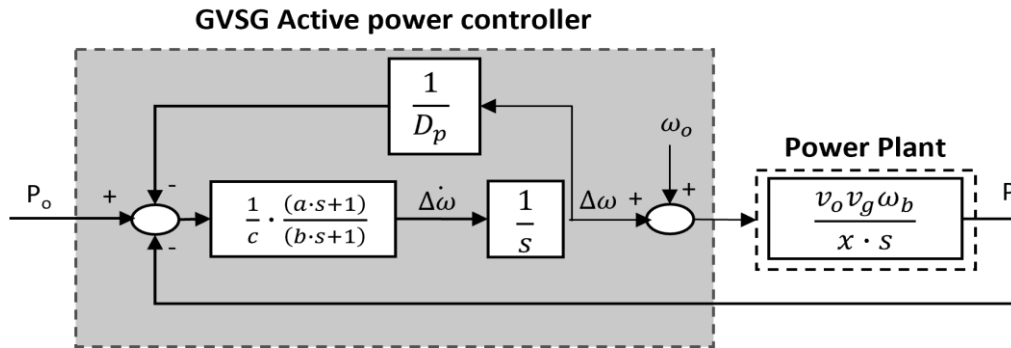
Figure 4.3. Closed loop block diagram of active power controller of GVSG.

The objective of the tuning of GVSG coefficients can be summarized as follows:

- Preserving the constant inertial response obtained by VSM (refer to section 2.3.6.1).
- Obtaining a transient response that is fast and accompanied by low or no overshoot.

4.2.1. Tuning of Inertial response

The GVSG is composed of mainly three coefficients a, b and c. The variable c is similar to the time constant of the VSM; thus, it participates in the inertial response. Further analysis is needed to determine if the existence of pole and zero affects that inertial response.

It is required to obtain a constant inertial response similar to the one defined by section 2.3.6.1 for the VSM. Hence, the GVSG is required to provide a change in its output power equivalent to 0.125 per unit for a ROCOF of 1 Hz/s. The inertial response for the GVSG can be presented from Figure 4.3 according to the following equation.

$$ROCOF = \frac{(a.s + 1)}{c \cdot (b.s + 1)} \cdot \left(P_o - P - \frac{\Delta\omega}{D_p}\right) \tag{4.1}$$

P_o represents the power setpoint, P is the electric power output of the inverter, and the term $\frac{\Delta\omega}{D_p}$ represents the droop response. The droop response is basically used for primary frequency regulation. It is not considered part of the inertial response; besides it is not constant during a ROCOF event. The inertial response in this case describes the change of electrical power apart from the power setpoint and the droop response. Thus, (4.1) can be reformulated accordingly.

$$ROCOF = \frac{(a.s + 1)}{c \cdot (b.s + 1)} \cdot (\Delta P)$$

$$\Delta P = (P_o - \frac{\Delta\omega}{D_p}) - P$$

(4.2)

It is required to supply a change in power of 0.125 per unit at a ROCOF of 1 Hz/s at steady state. The steady state value for (4.2) can be derived as

$$ROCOF_{Steady-State} = \lim_{s \to 0} \frac{(a.s + 1)}{c \cdot (b.s + 1)} \cdot (\Delta P)$$

(4.3)

Solving the previous formula will obtain the expression of ROCOF at steady state in terms of change in electric power as follows.

$$\frac{d\Delta\omega}{dt}\bigg|_{Steady-State} = \frac{1}{c} \cdot (\Delta P)$$

(4.4)

This expression looks exactly the same as (2.60), which was used to describe the inertial response of VSM. In that matter, at steady state, the coefficients a and b do not really affect the inertial response of the inverter, and it just depends on variable c. Hence, the same value of time constant obtained in the tuning of VSM can be applied to c, allowing an inertial response complying with the requirements defined.

$$c = 6.25 \ s$$

(4.5)

4.2.2. Active Power Droop Coefficient

The implementation of a constant reference frequency instead of an estimated frequency measured by the PLL causes an emulation of the drag coefficient to the droop. In this case, tuning of drag coefficient will be limited by the droop characteristics and cannot be freely tuned to any value.

In section 2.3.5, the reactive power droop was implemented to regulate the voltage variations across the point of common coupling (capacitor). The active power droop is responsible for regulating frequency changes in the grid as shown in Figure 4.4. This is possible due to having a decoupled power dynamics by using virtual impedance as described in section 2.3.3. The active power droop equation can be written as following.

$$(P_o - P) \cdot D_p = -(\omega_o - \omega_{vsm}) \tag{4.6}$$
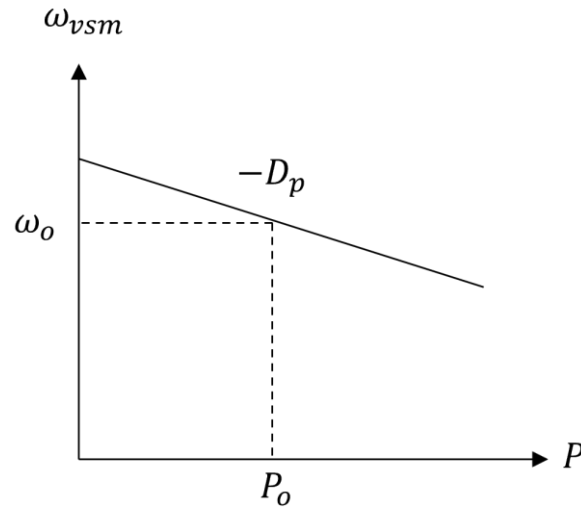
Figure 4.4. Active power droop response diagram.

The active power droop can be calculated based on the same requirements stated for the reactive power droop but for the frequency in that case. So, two requirements need to be satisfied. First is to set a maximum frequency variation for the VSM and second is to determine the active power that counters such variation [20]. The maximum variation allowed for the frequency is 4%, while the power responsible to counter the perturbations is the inverter rated power that corresponds to one per unit. Hence, the droop coefficient can be calculated accordingly.

$$D_p = 0.04 \; pu \tag{4.7}$$

4.2.3. Tuning of Transient Response

The identification of the GVSG dynamic respond can be obtained through the transfer function of the closed loop of active power controller represented in Figure 4.3. A more simplified representation of the block diagram is shown in Figure 4.5.
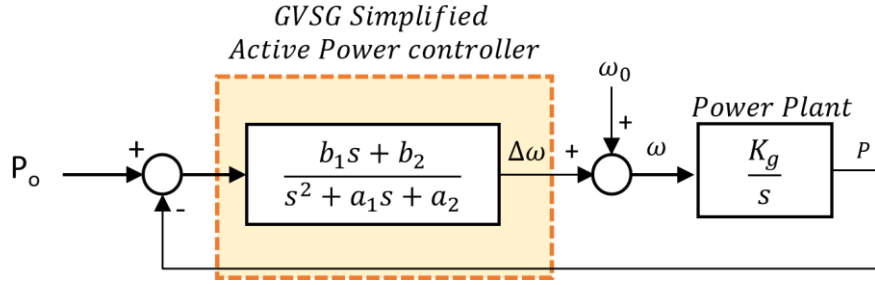
Figure 4.5. Closed loop diagram of GVSG active power controller after simplification.

The new coefficients used to represent the GVSG active power controller in Figure 4.5 can be defined in terms of the old ones from Figure 4.3 accordingly [11].

$$a_1 = \frac{c + D \cdot a}{b \cdot c} \quad , \qquad a_2 = \frac{D}{b \cdot c}$$

$$b_1 = \frac{a}{b \cdot c} \quad , \qquad b_2 = \frac{1}{b \cdot c} \tag{4.8}$$

$$D = \frac{1}{D_p}$$

The power plant transfer function is presented in terms of coefficient K_g for simplification as described previously in the VSM section with a SCR of 10. The closed loop transfer function of GVSG active power controller can be obtained from Figure 4.5 as described in (4.9) [11].

$$G_{cl,GVSG} = \frac{K_g(b_1 s + b_2)}{s^3 + a_1 s^2 + (a_2 + K_g \cdot b_1) s + K_g \cdot b_2} \tag{4.9}$$

The closed loop transfer function of GVSG consists of a 3rd order system in the denominator representing three poles and a zero in the nominator. Identifying the dynamic characteristics of this transfer function is quite difficult. Hence, the approach adapted for tuning this transfer function will depend on enforcing some inequality constraints that ensures the stability of the controller as well as a good transient response. It should be noted that the droop coefficient and coefficient c are already

tuned to achieve the desired inertial and droop response as defined in previous sections. The objective of this section is to define some inequality constraints. Then, using these constraints, a range of values can be obtained for coefficients a and b that abides by the constraints defined.

To avoid confusion, the equations of the inequality constraints will all be written in terms of the new coefficients of GVSG a_1, a_2, b_1, and b_2 from now on since it is easier and more convenient. However, the goal in the end is to find a range of values for the old coefficients of GVSG a and b as c and D_P are already calculated, thus only two coefficients are required to be tuned instead of four.

To ensure the stability of the active power controller, Routh-Hurwitz criterion is applied [11]. The Routh-Hurwitz criterion states that a third order polynomial $P(s) = s^3 + m_2 s^2 + m_1 s + m_o$ has all its roots in the left half-plane of the s-plane only if m_2, m_1, and m_o are positive and $m_2 m_1 > m_o$. Applying this criterion to the denominator of the transfer function of (4.9), ensuring all poles are in the left half-plane for stability, the following inequality constraints can be defined.

$$
\begin{cases}
a_1 > 0 \\
a_2 + K_g \cdot b_1 > 0 \\
K_g \cdot b_2 > 0 \\
a_1 \cdot (a_2 + K_g \cdot b_1) > K_g \cdot b_2
\end{cases}
\tag{4.10}
$$

After ensuring the stability of the system, the next constraints will be concerned with the dynamics of the system. To determine the dynamic response of the GVSG, the denominator of the transfer function of (4.9) can be considered as a second order multiplied by a first order system as shown in (4.11) [24].

$$
s^3 + a_1 s^2 + (a_2 + K_g \cdot b_1) s + K_g \cdot b_2 = (s + p)(s^2 + 2\zeta\omega_n s + \omega_n^2) \tag{4.11}
$$

Using this equation, various assumptions can be made to obtain different tunings for the GVSG. In this thesis, mainly the approach implemented to tune the GVSG system assumes that the second order system in (4.11) is underdamped, having complex poles.

This approach will be further analyzed, detailing the assumptions and inequality constraints accompanied by it to ensure a good dynamic response for the GVSG system.

The solution of the characteristic equation of the third order system determines whether the second order system poles are real (overdamped) or complex (underdamped). Hence, to ensure that the second order system has complex poles, the discriminant of the third order system is driven in (4.12) [25].

$$\Delta = (\frac{de}{6c^2} - \frac{d^3}{27c^3} - \frac{f}{2c})^2 + (\frac{e}{3c} - \frac{d^2}{9c^2})^3 \tag{4.12}$$

Where coefficients of (4.12) are defined accordingly

$$\begin{cases} c = 1 \\ d = a_1 \\ e = (a_2 + K_g b_1) \\ f = K_g b_2 \end{cases} \tag{4.13}$$

An underdamped response is desired to obtain a fast dynamic response for the GVSG. For obtaining an underdamped response, the following constraint is imposed.

$$\Delta < 0 \tag{4.14}$$

After ensuring that the second order poles of the third order system are complex, another constraint can be imposed on the damping coefficient of the second order system, found in (4.11), as defined by (4.15)

$$\zeta > \zeta_{critical} \tag{4.15}$$

The critical damping ratio in this case is chosen to be 0.8. Details of how to obtain the damping ratio and the dynamic characteristics of the second order polynomial of the third order system is explained in Appendix A.

Finally, it should be noted that the dynamic response of the system does not necessarily follow the dynamic characteristics of the complex poles of the underdamped second order polynomial. The reason is that there exists another real pole in the solution of the third order system. In this case, the pole might affect the second order response depending on its value and how close it is to the origin. In fact,

the system might react very differently from the second order system that we are trying to restrict its dynamic response characteristics through constraints (4.15) and (4.14).

Hence, another constraint needs to be defined that ensures that the third order system has a dominant second order system, meaning that this third order system can be assumed to be a second order one neglecting the pole effect. For this reason, the real part of the complex poles is constrained to be at least 5 times smaller than the real pole, enabling the complex poles to have a more dominant effect on the third order system. From (4.11), (4.16) can be defined accordingly.

$$5\omega_n\zeta < p \tag{4.16}$$

Also, it is expected that the zero present in the transfer function of the GVSG will affect the response expected from the inequality constraint. However, this is not really an issue since the zero will result in increasing the speed of the response more.

A MATLAB script was developed to solve the system of equations and inequality constraints defined in this section to obtain a range of values for GVSG coefficients and b. The script basically works by defining a range of values for a and b. Then, it finds which of the values inside this range follows the inequality constraints defined by (4.10), (4.14), (4.15), and (4.16). Following that, a new range of setpoints is formed for a and b that abides by the inequality constraints and a setpoint is chosen as a conclusion of the tuning. The values of GVSG coefficients are summarized in table 4-1.

Table 4-1. Design Parameters value of GVSG active power controller.

GVSG Coefficients	Values
a	0.126
b	0.019
c	6.25 [s]
D_p	0.04 [pu]

Using the tuned coefficients of table 4-1, the expected step response from the transfer function of (4.9) is drawn in Figure 4.6. In this Figure, the step response of the full transfer function is shown along with the step response of a simplified version of the transfer function. The simplification is implemented by assuming that the third order system is a second order one, neglecting the pole. The objective here is to show that this pole does not affect the dynamic response almost at all. The pole only affects the system by a small delay and small reduction of overshoot that can be ignored. Thus, the constraint defined in (4.16) is successful in making the third order system in the denominator of (4.9) to be a second order dominant.

Moreover, the overshoot expected only from the complex poles should be about 2% according to (4.15). However, the overshoot shown in Figure 4.6 is about 18%. This means that the zero of the GVSG transfer function has a noticeable effect on system behavior, meaning it is near the origin of s-plane with respect to the complex poles, allowing the GVSG to have a faster dynamic response but with a more overshoot.
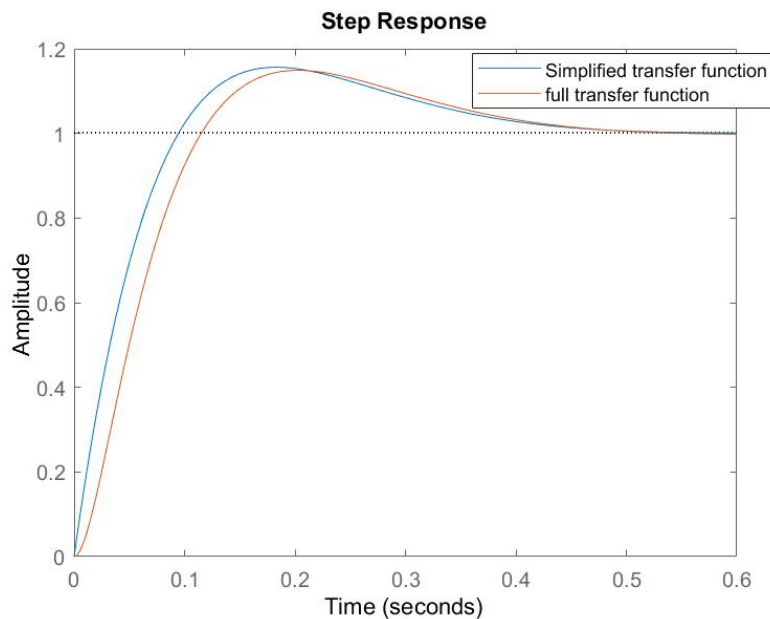
Figure 4.6. Step power response of GVSG active power controller transfer function for full and simplified versions of the transfer function.
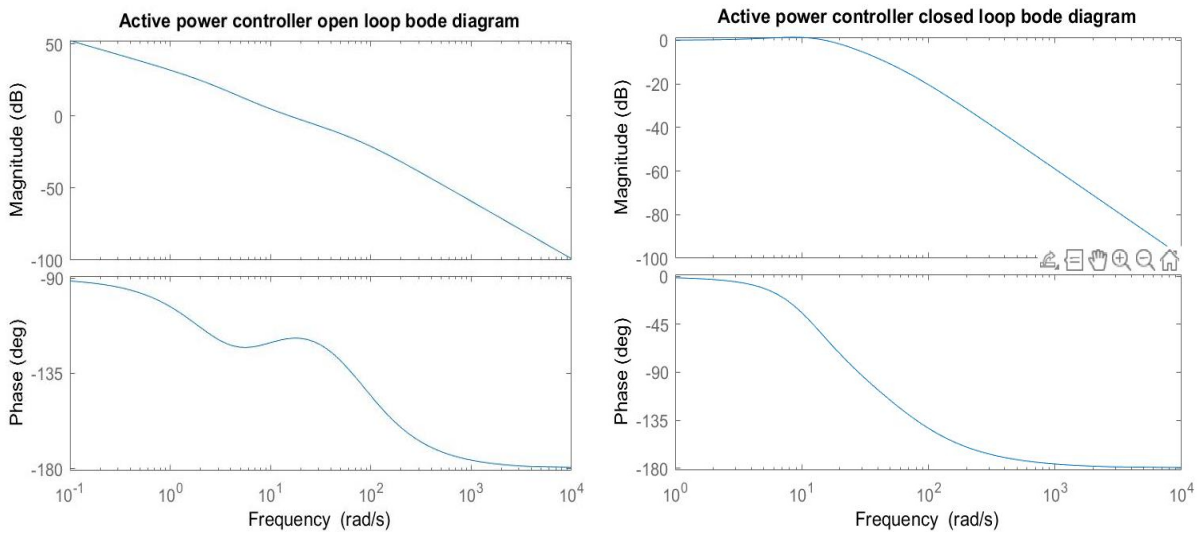
Figure 4.7. The Figure on left describes the open loop bode plot of GVSG active power controller, while the Figure on the right describes the closed loop bode plot of GVSG active power controller.

The bode diagram of the closed and open loop of the active power controller for the GVSG is plotted in Figure 4.7. It is important to notice that these bode diagrams describe the full transfer function. The simplified transfer function was only implemented for the sake of comparing the responses of both transfer functions, ensuring the validity of inequality constraints defined and the possibility to draw some expectations on the dynamic behavior of the GVSG system.

The phase margin of the system can be obtained from the open loop bode diagram of Figure 4.7, which is around 60 degrees, while the bandwidth is achieved from the closed loop bode diagram. The bandwidth of the active power controller of GVSG corresponds to 23.3 rad/s. The bandwidth of the active power controller is much smaller compared with the inner and outer controllers, thus ensuring no interactions happen between these controllers.

4.3. Compensated generalized virtual synchronous generator

The step response shown in Figure 4.6 for the GVSG control topology was characterized by a big overshoot, considering the objective of the thesis is to have a maximum overshoot of about 10% across all SCR ranges.

Therefore, the proposed GVSG can be further developed by adding a compensator. The GVSG with a compensator is referred to as CGVSG (compensated generalized virtual synchronous generator). As mentioned before, the zero of the closed loop transfer function of GVSG results in a faster response but an increase in the overshoot of the dynamic response. A damping correction loop is added to further damp the response of the GVSG. The damping correction loop is basically the derivative of the measured electric power injected into the grid in addition to the typical error in power. This can be implemented by moving the zero of the GVSG to the feedback path of measured power as shown in Figure 4.8 with the coefficients of the transfer function written in terms of the old variables a, b and c.
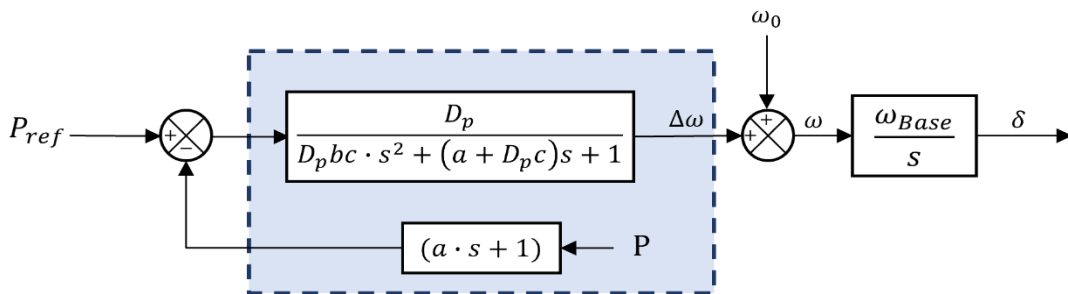
Figure 4.8. Inertia emulation block representation of CGVSG.

The structure of CGVSG shown in Figure 4.8 is difficult to implement because of the zero present in the power feedback path. As a result, the block diagram is changed to a more suitable structure for implementation, which is described by Figure 4.9.
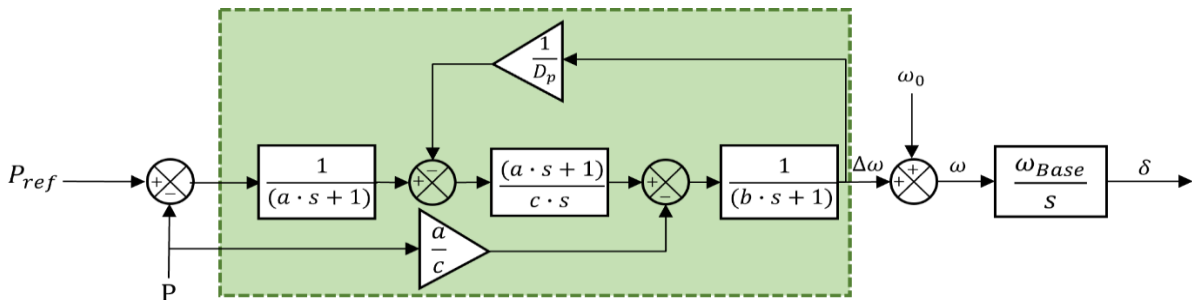
Figure 4.9. Control block diagram of CGVSG for implementation.

The closed loop transfer function of the active power controller of CGVSG can be described using Figure 4.8. Figure 4.8 shows the open loop diagram of CGVSG. To get the closed loop block diagram, the power plant transfer function should be added to this open loop diagram. The power plant transfer function adopted is the same as the one found in Figure 4.5. Then, the closed loop transfer function can be computed accordingly [4].

$$G_{cl,CGVSG} = \frac{K_g D_p}{D_p b c s^3 + (a + D_p c) s^2 + (1 + K_g D_p a)\, s + K_g D_p} \qquad (4.17)$$

This transfer function has the same denominator as the transfer function of GVSG with the zero removed from the nominator because of the compensator. Hence, the same tuning criteria can be applied to the CGVSG and the same value of coefficients from table 4-1 can be chosen.
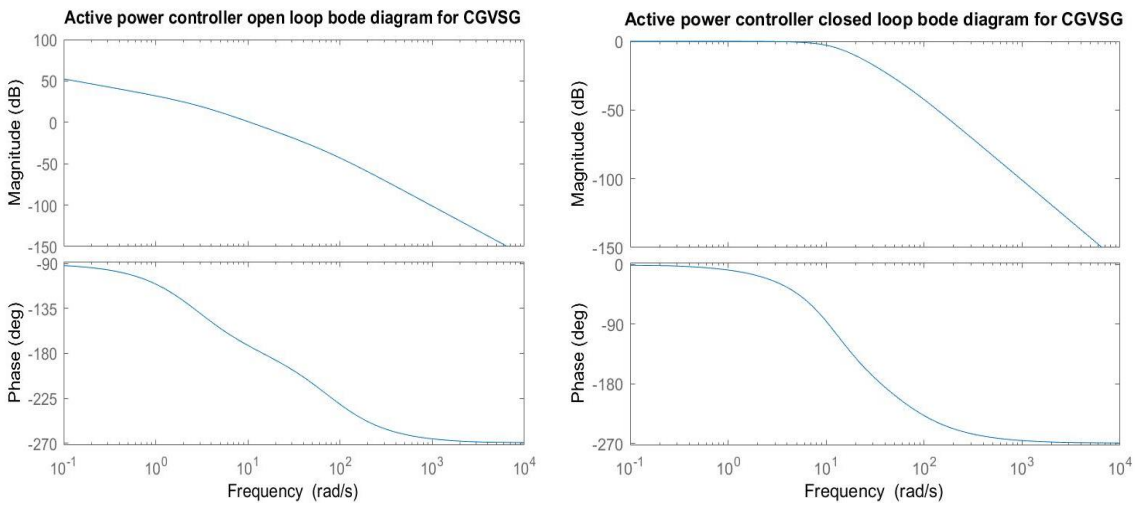
Figure 4.10. The Figure on the left describes the open loop bode plot of CGVSG active power controller, while the Figure on the right describes the closed loop bode plot of CGVSG active power controller.

The bode diagram of the closed and open loop for the active power controller of GVSG is shown in Figure 4.10. The phase margin can be obtained from the open loop diagram, which corresponds to about 10 degrees. The phase margin is quite low, but the system is still stable with such a margin. The bandwidth of the controller is around 10.3 rad/s. This means that the CGVSG is expected to behave slower than the GVSG, which is expected as the zero was removed and the system is further damped.

5   Dynamic Simulations for GVSG and CGVSG.

This chapter focuses on the testing of GVSG and CGVSG throughout the same tests performed for the VSM using the same Simulink model, but with some changes in the firmware block to implement the control structure of GVSG and CGVSG instead of the VSM. The chapter starts with the step power setpoint change followed by the step frequency change, then the ROCOF event. A final section is dedicated to compare the dynamic response of VSM, GVSG, and CGVSG to find the best grid-forming methodology in terms of inertial and transient behavior.

The model used for the simulation is the same used for VSM shown in Figure 3.1. The average model of the inverter and the parameters of the physical system are also described by Figure 3.2 and 3.3 respectively.

5.1.   Dynamic behavior for a change in Power Setpoint

The step power change test is defined with the same standards as section 3.2 for the VSM. The results for the GVSG and CGVSG will be shown together to be able to compare the results and observe the effect of adding a compensator in the CGVSG. Figure 5.1 shows the dynamic response of injected power for both control methodologies.

The transient behavior of the GVSG is observed to be fast since it is tuned in section 4.2.3 to have complex poles along with a zero that makes it faster. Moreover, the response is very similar to the one obtained by the step response of transfer function of (4.9) as shown in Figure 4.6. This is mainly because of the small bandwidth obtained by the active power controller leading to a negligible effect of the outer voltage controller and inner current controller on the dynamic response as they have a much larger bandwidth.

Adding a compensator in the CGVSG model leads to a more damped response as shown in Figure 5.1. The power response is overdamped with no overshoot, which is desired in the inverter to avoid saturation. However, having an overdamped response causes a slower dynamic and the rise time of CGVSG is almost twice that of the GVSG.
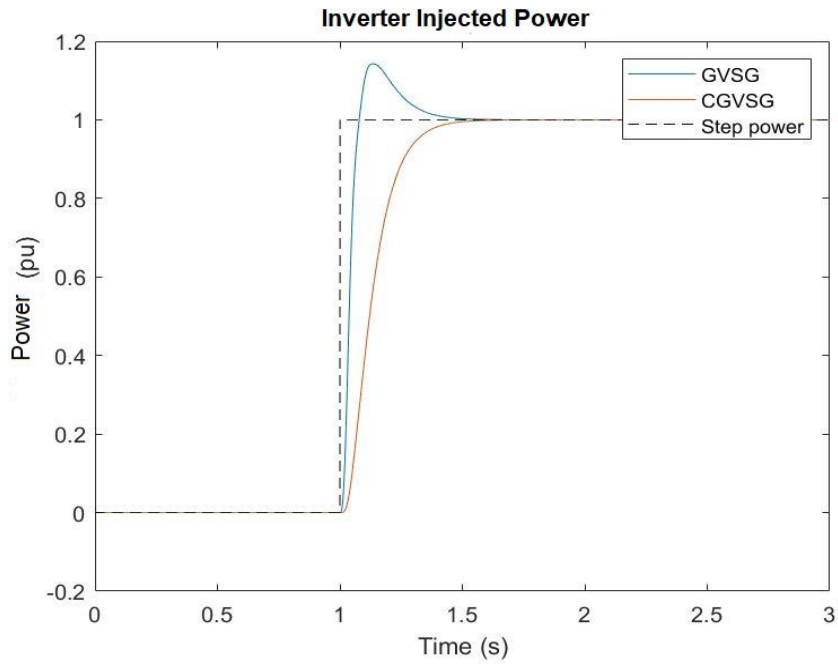
Figure 5.1. CGVSG and GVSG injected powers during a step change in power setpoint
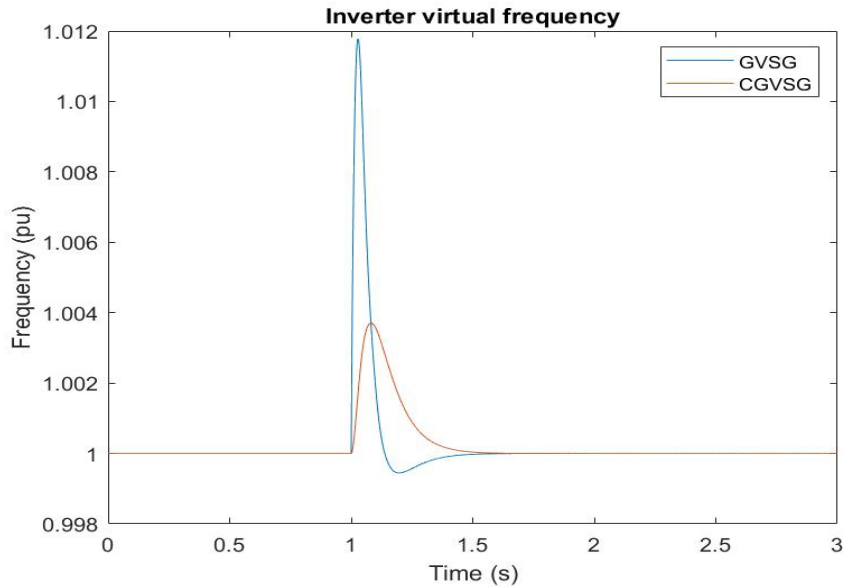
Figure 5.2. CGVSG and GVSG virtual frequencies during a step change in power setpoint

The frequency behavior during the step power setpoint change is characterized by a larger ROCOF and frequency nadir for the GVSG virtual frequency compared with the CGVSG virtual frequency as shown in Figure 5.2. This is expected since the electric power of the GVSG has a higher overshoot as well as a faster response because of its high ROCOF.

Also, the overshoot in the power response of GVSG leads to a deceleration of the virtual frequency causing it to go lower than one per unit before coming back to one per unit with the help of the grid synchronization and droop response.

5.2. Dynamic behavior for a change in Grid Frequency

The step change in the grid frequency is defined as in section 3.3, which can be also observed in Figure 5.3. The step frequency test is shown by the black dotted line in Figure 5.3, where the frequency is changed from 1 per unit to 0.98 per unit corresponding to a decrease in frequency of 1 Hz. It should be noted that the virtual frequency transient behavior of both GVSG and CGVSG is exactly the same, which is why only one line is shown in Figure 5.3.

The main reason for such similarity in response is that the CGVSG is obtained just by moving the zero from the transfer function of GVSG to the feedback of active power as explained in section 4.3, which is equivalent to just removing the zero from the power setpoint but maintaining it with the measured electric power. This will only affect the transfer function of power with respect to the power setpoint. However, if we try to model the transfer function of power to the grid frequency, it will be exactly the same in both control topologies leading to having the exact same response for any change in the grid frequency.
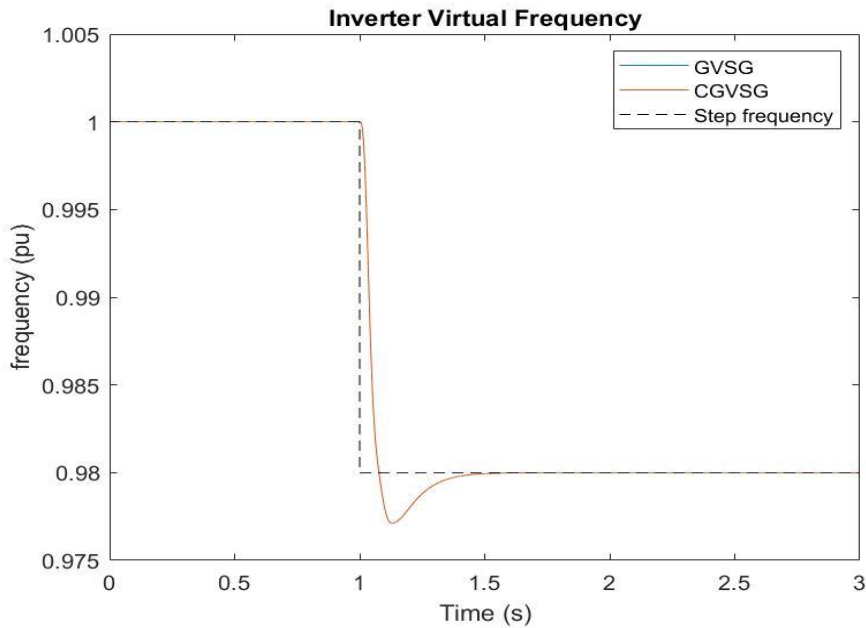
Figure 5.3. CGVSG and GVSG virtual frequencies during a step change in grid frequency.

The power dynamic behavior is described in Figure 5.4. Similar to the case of virtual frequency, the power dynamic response of both GVSG and CGVSG are similar. It can be noticed that the power response reaches a high spike at the beginning of the step frequency test. This is mainly because the response in this case is not composed of only the inertial response, but it is integrated with the droop response.

Implementing a constant reference frequency instead of a measured one will cause a droop response. This is why the drag coefficient becomes equivalent to the droop and it cannot be freely tuned any more as it can lead to enormous changes in the injected power. After the settling of inertial response, the Inverter power reaches a steady state at 0.5 per unit all supplied by the droop since the power setpoint is zero. Having the droop implemented directly in the control method can have some drawbacks as it will limit the inertial response of the inverter to avoid injecting power more than the ratings of the inverter.
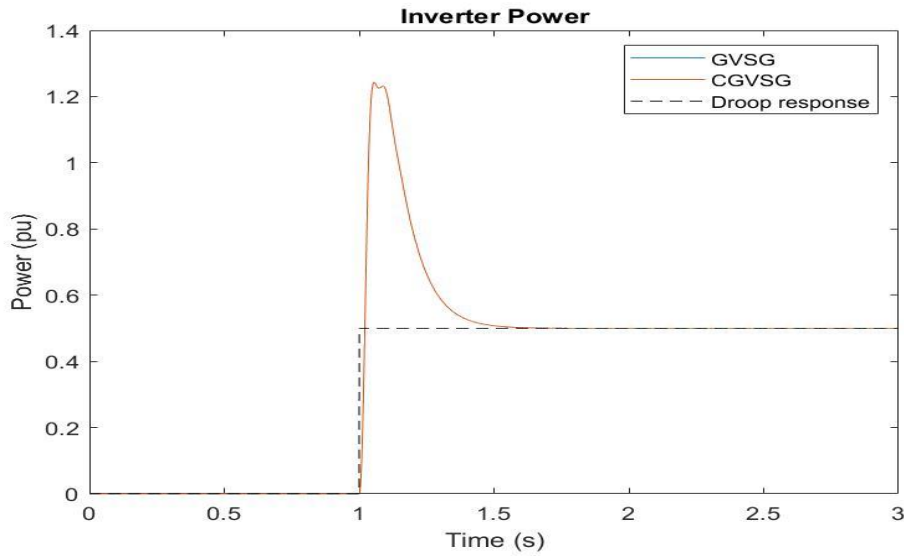
Figure 5.4. CGVSG and GVSG injected powers during a step change in grid frequency.

5.3.   Inertial Response for a ROCOF Event

Similar to previous cases, this test is defined as section 3.4 which was implemented for the testing of VSM. The ROCOF event can be shown in Figure 5.5, which is observed to have the same dynamic response of the virtual frequencies of GVSG and CGVSG. This is expected since this test is also characterized by a change in grid frequency, and it was mentioned in the previous section that the transfer function of the injected power with respect to the grid frequency is the same in both cases.

In Figure 5.5, the virtual frequency follows a slope that is equivalent to -0.02 per unit for every second, then the grid frequency is saturated at 0.98 per unit, and the virtual frequencies of both inverters synchronize with the grid in a very short interval with a negligible frequency nadir.
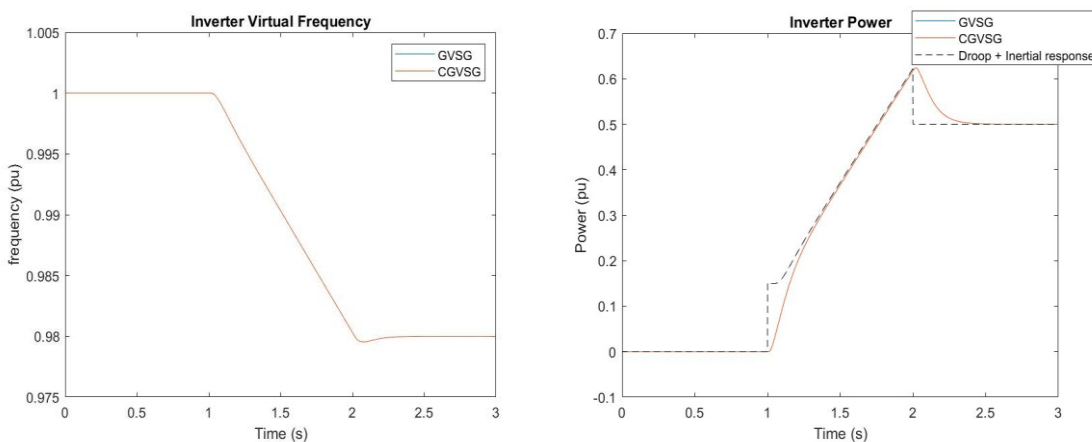
Figure 5.5 Figure on the left represents CGVSG and GVSG virtual frequency during a ROCOF event, while figure on the right represents CGVSG and GVSG power injected during a ROCOF event.

In Figure 5.5, the output power from both inverters is observed with the same dynamic behavior that can be explained as follows. The black dotted line of Figure 5.5 explains the ideal trajectory that the output power should follow according to the droop and inertial response.

At the start of the ROCOF event, the inverter should output an inertial response equivalent to 0.125 per unit. Then, the power keeps increasing with a slope due to the droop response. Because of the inertial response dynamics, the inverter takes time to reach the desired inertia and it matches the ideal trajectory after about 0.4 seconds. Following that, the output power matches the required response as only the droop response is changing. Since the droop response is ramped not a step change, the inverter can follow such trajectory without any errors.

After stopping the ROCOF event with a frequency saturation, the inertial response is omitted and only the droop response remains, which corresponds to 0.5 per unit as in the previous section since frequency value is the same in both cases with a value of 0.98 per unit. A dynamic response is initiated after removing the inertial response since this is equivalent to a step change and the injected power settles at 0.5 per unit in about 0.4 seconds.

5.4. Short Circuit Ratio Effect on Response Dynamics

In this section, the effect of changing the short circuit ratio is investigated on the dynamic response of GVSG and CGVSG. The SCR will be changed for the three tests implemented in the previous sections step power, step frequency, and ROCOF event. The standards for those tests can be described by section 3.5 similar to the SCR tests performed for the VSM.

The first results are shown in Figures 5.6 and 5.7 for varying the SCR during the step power setpoint test. Figure 5.6 describes the response of GVSG, while Figure 5.7 shows the behavior of CGVSG. Both control methods show a slower response with a higher overshoot as the short circuit ratio is decreased.

Similarly, the virtual frequency reaches a higher nadir with a slower rate. The overshoot in the GVSG crosses the maximum allowed value of 10%, while the CGVSG has a maximum overshoot of around 8%. Overall, the dynamics of the CGVSG are not

affected much by changing the SCR. Moreover, the GVSG is shown to have a strange response during high values of short circuit ratios. This is because the bandwidth of the controller increases with the SCR causing interference with the voltage controller dynamics.

The CGVSG response is better in maintaining its characteristics than the GVSG for different SCR, where the latter has a big change in the response speed, but not much in the overshoot, while CGVSG has the dynamic change mostly in the overshoot instead. However, the CGVSG manages to stay under the maximum allowed overshoot anyway, thus it is not an issue to change the overshoot.
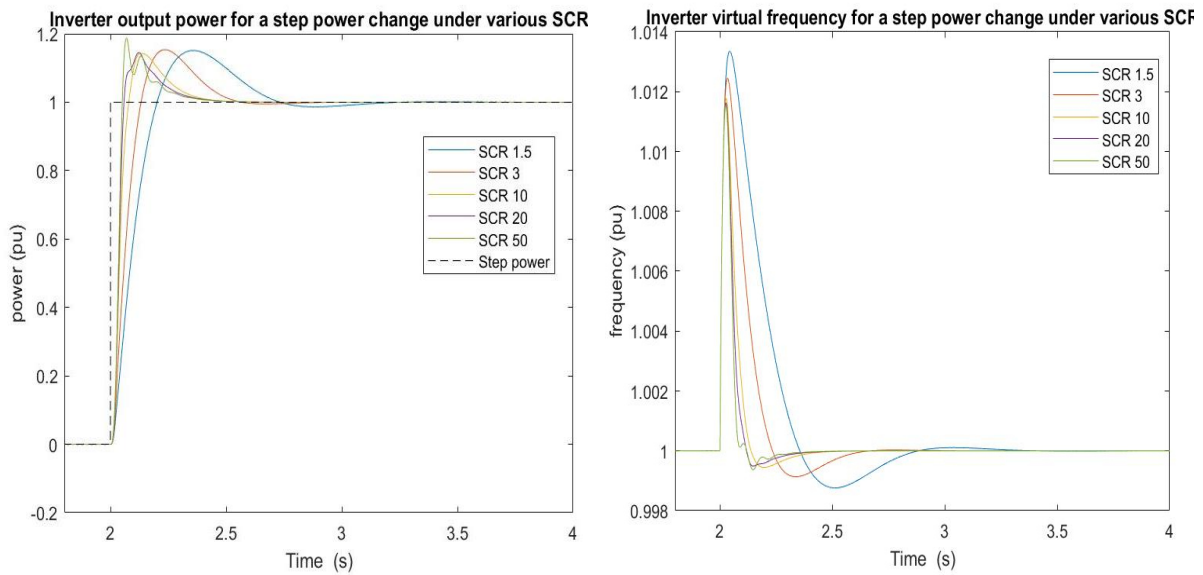
Figure 5.6. GVSG Injected power and virtual frequency under a step change in power setpoint for different short circuit values.
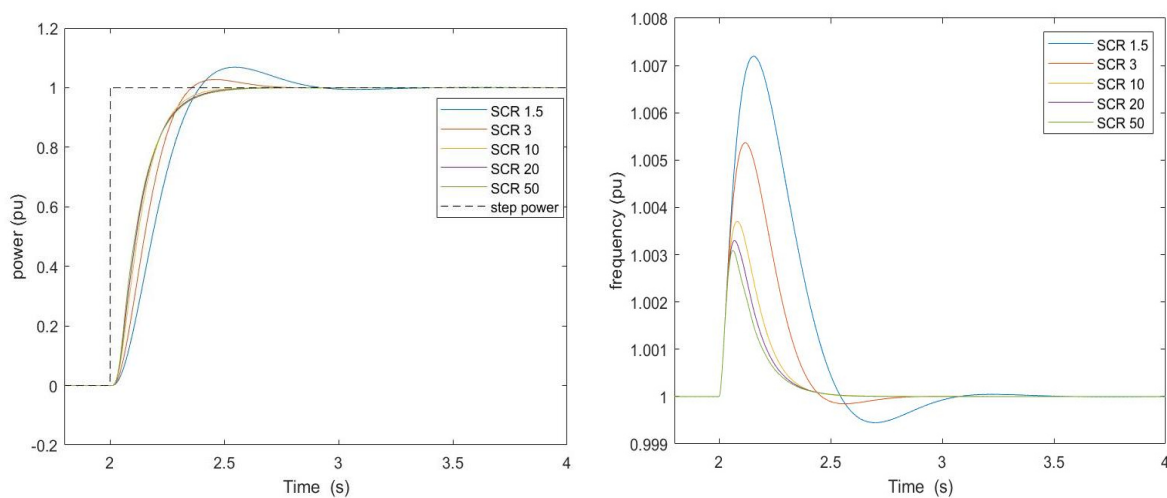
Figure 5.7. GVSG Injected power and virtual frequency under a step change in power setpoint for different short circuit values.

The step power results are followed by the frequency perturbation outcomes in Figures 5.8, 5.9, 5.10, and 5.11. Figures 5.8 and 5.10 describe the dynamic behavior of GVSG during step frequency and ROCOF event respectively, while in Figures 5.9 and 5.11 the transient behavior of CGVSG is observed for a step frequency and ROCOF event respectively.

The dynamic behavior of both topologies during the SCR change is identical since, as explained before, both structures behave the same during grid frequency perturbations.

For high SCR, more inertia is given to the system during the step frequency change, accompanied by a faster change in frequency and a faster power dynamic. Following that, the power settles back to the droop response, which is equivalent to 0.5 per unit. The smallest SCR has the slowest power response since the SCR affects the speed of power response.
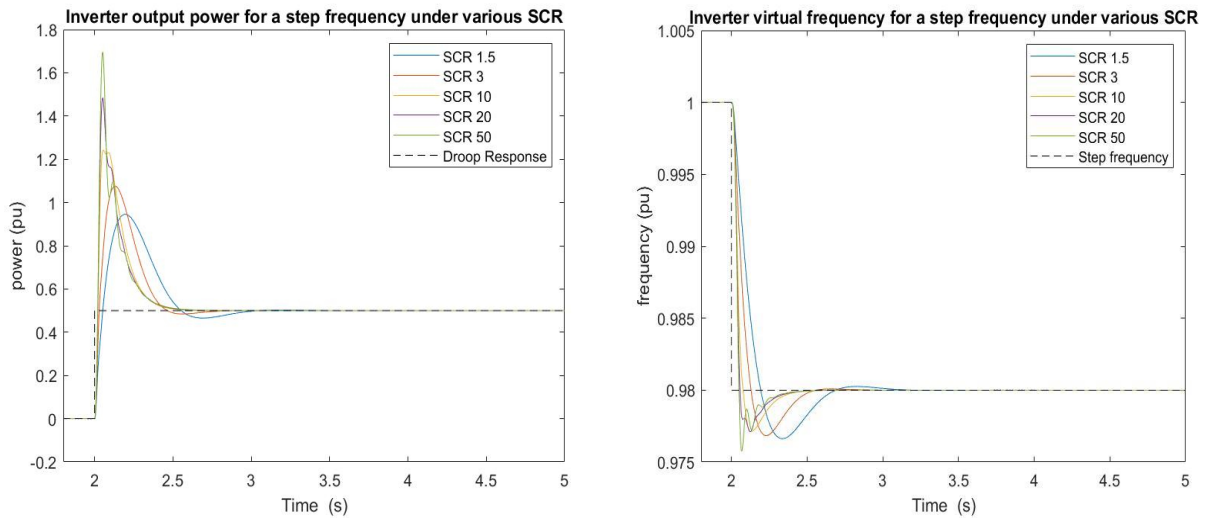
Figure 5.8. GVSG Injected power and virtual frequency under a step change in grid frequency for different short circuit values.
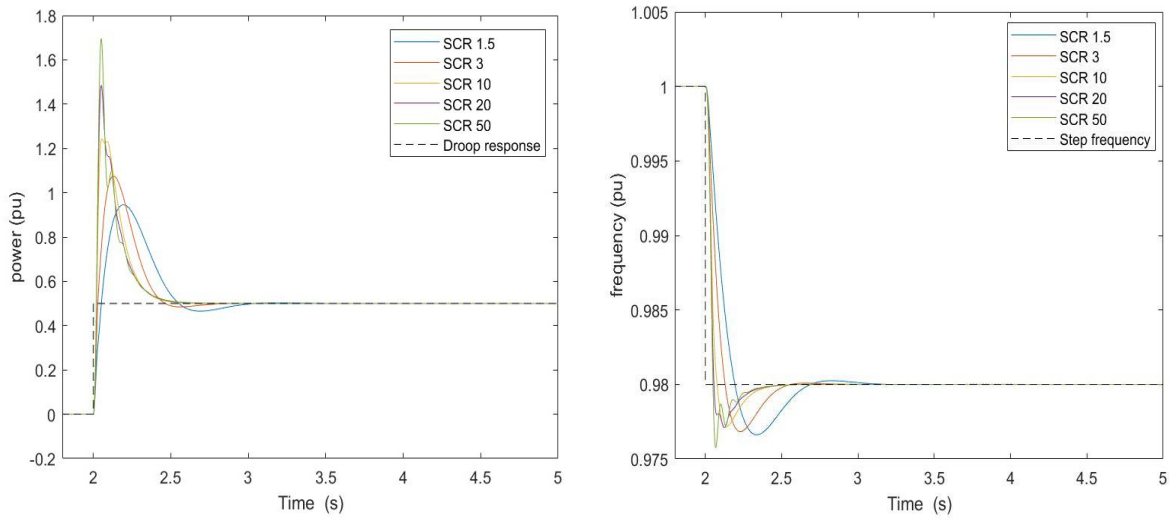
Figure 5.9. CGVSG Injected power and virtual frequency under a step change in grid frequency for different short circuit values.

It can be a problem to provide inertial power to the system during a high value of SCR since it can cause a very high spike in the power behavior leading to damaging the inverter.
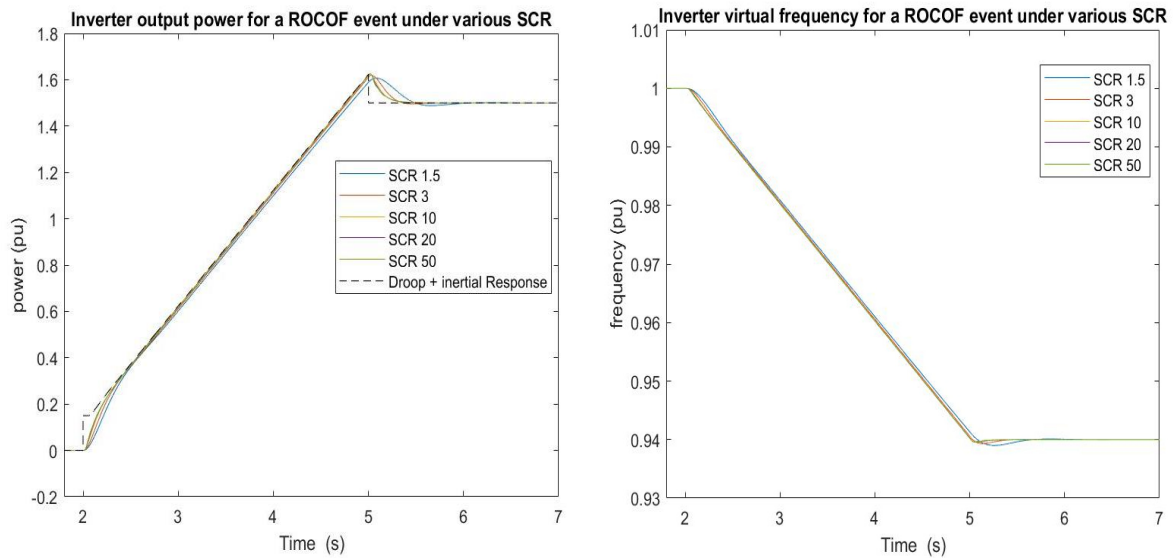
Figure 5.10. GVSG Injected power and virtual frequency under a ROCOF event for different short circuit values.

The ROCOF dynamic behavior shown in Figure 5.10 and 5.11 can be considered almost the same across all SCRs since the frequency is ramped, thus no large perturbations are applied on the system and the difference between the dynamics of various SCR are negligible.

The expected trajectory of the ouput power during the ROCOF event was explained in section 5.3, showing that the inverter should provide both inertial and droop response due to maintaining a constant ROCOF.
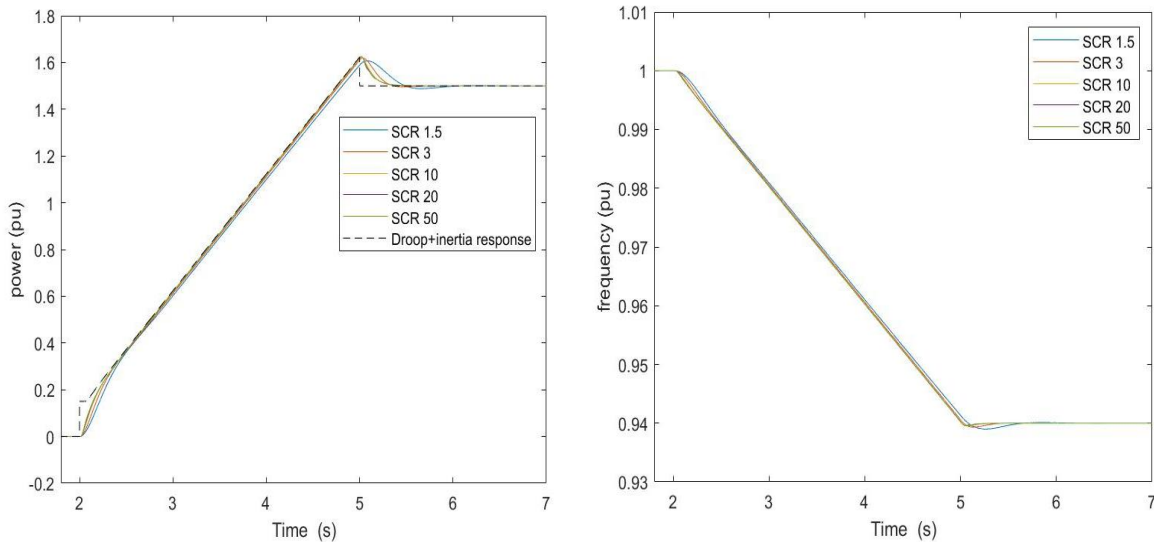
Figure 5.11. GVSG Injected power and virtual frequency under a ROCOF event for different short circuit values.

5.5. Comparison between Grid-forming Control Methods

This thesis focused on the design and testing of three control methods classified under the grid-forming control, which are VSM, GVSG, and CGVSG. In this section, a comparison between these methods is developed along with two other structures. The first structure will be the VSM but with a constant reference frequency, meaning a droop coefficient is used instead of the drag coefficient.

The second method is the GVSG with a PLL and an overdamped tuning implemented instead of the underdamped as explained in section 4.2.3. The overdamped tuning focuses on having three real poles and a zero in transfer function of (4.9). Moreover, the zero will be canceled out with one of the poles, removing the pole that causes the system to behave slowly, leading to a very fast response. Because of the very fast response of the overdamped GVSG, the PLL is added to slow down the dynamics and eliminate interactions with voltage controller.

The control topologies mentioned will be compared using the step power setpoint test and the ROCOF test. There is no need to include the step frequency test since the same conclusions can be obtained from the ROCOF test.

The step power dynamic response for different grid-forming technologies is observed in Figure 5.12 with the virtual frequency shown in Figure 5.13. The SCR used for this test is 10.
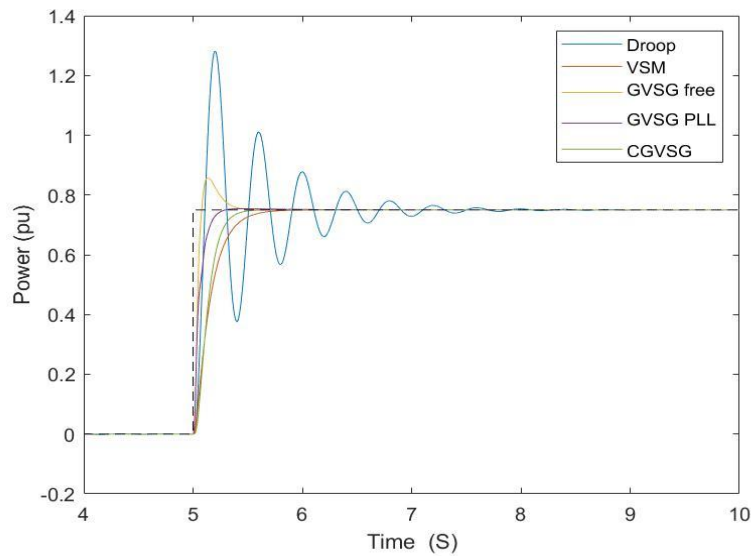
Figure 5.12. Power injected by various grid-forming control methods under step change in power setpoint.
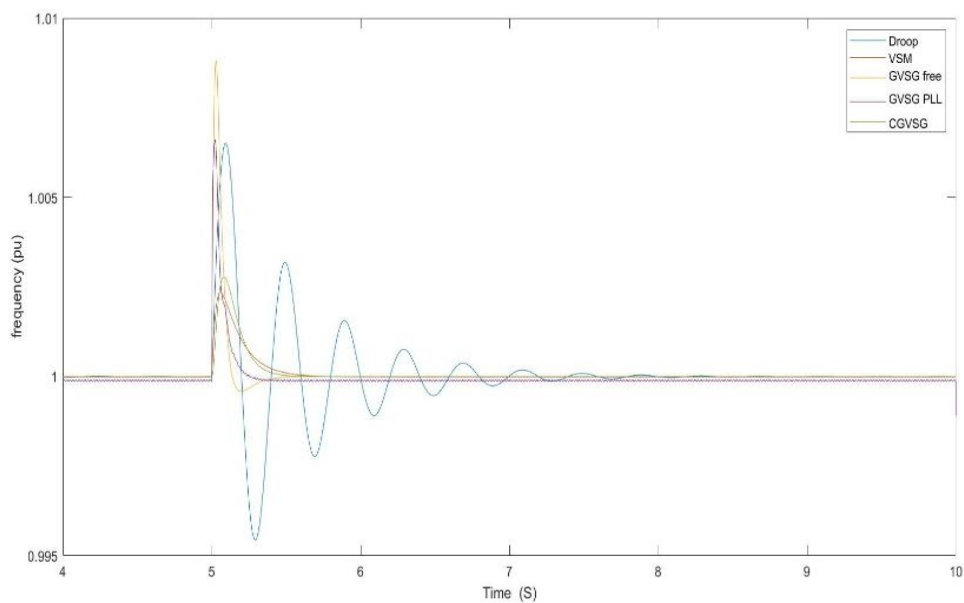
Figure 5.13Virtual frequency of various grid-forming control methods under step change in power setpoint.

From Figure 5.12, It can be observed that the VSM with droop coefficient is characterized by a very high overshoot because of the droop implementation. This is not desired in the dynamic response because of the inverter ratings. Then, the GVSG is also characterized by oscillations but lower than the VSM one. This is mainly due to the extra pole and zero added to the GVSG, which causes the system to reach a little faster with lower oscillations.

The VSM response with the drag coefficient shows a transient behavior that is slower than other technologies but having no overshoot. This response is very similar to the CGVSG and both methods show a desired response according to the thesis objective.

Furthermore, the GVSG with PLL implemented instead of the droop is observed to have the best dynamic behavior having no overshoot and a so fast response that is almost as fast as the GVSG and VSM with droop coefficients.

Hence, the step power test concludes that only the CGVSM, VSM with PLL and GVSG with PLL obtain an acceptable dynamic response that doesn't cross the maximum allowable overshoot. The GVSG is the fastest in its response followed by the CGVSG and VSM. The frequency ROCOF test outcome is then shown in Figure 5.14 to identify the control topologies most suitable for the application of this thesis.
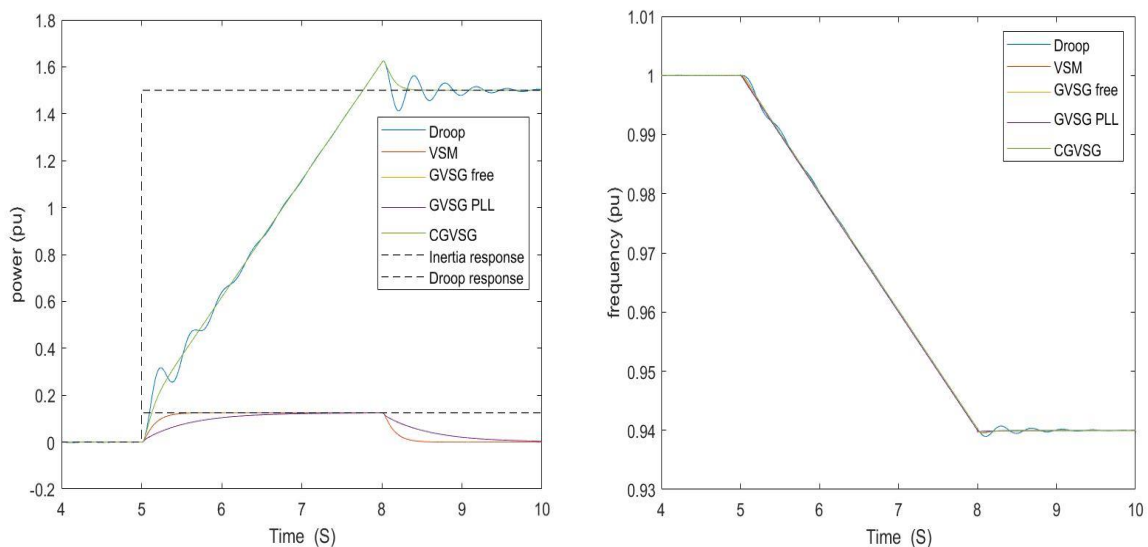
Figure 5.14. Figure on left shows the power injected by various grid-forming control methods under a ROCOF event, while the Figure on the right describes the virtual frequencies for these control methods under ROCOF event.

It can be noted that the methods implemented with PLL do not have a droop response during frequency change, but methods with droop coefficient are characterized by a droop response along with the inertial response.

At the start of ROCOF, the droop, CGVSG, and GVSG show a fast change in the power meaning that they provide more inertia and support to the grid, and they can reach the desired inertial response faster than other technologies. The VSM with PLL also shows a relatively fast response that is not much different from those mentioned technologies. An advantage of the VSM is that it only gives the inertial response minimizing the electric power spike.

On the other hand, the GVSG with PLL is showing a surprisingly very slow response that takes about two seconds to reach the desired constant inertial response. This response is not preferred in most applications as the system is required to react faster than that. So, the GVSG with a PLL can give a very good dynamic response with power perturbations but fails to reach the desired characteristics with frequency changes.

The only technologies that can be recommended for the system are CGVSG and VSM. Both technologies do not cross 10% overshoot even with changing the short circuit ratio. They can provide a constant inertial response with a fast-acting dynamics. The CGVSG is a little faster than the VSM and can provide more inertia during step changes of frequency mainly because of the dynamic response speed and the extra zero and pole that affect the inertial behavior during transient state. However, CGVSG has a higher risk in crossing the rated power compared with the VSM. Hence, it is concluded that both of these control methods are the most suitable grid-forming technologies for application.

6   Conclusion and future developments

In this final chapter, a summary of the thesis will be presented, highlighting the main advantages and concerns for the reference control methods. A further suggestion will be given for future topics and developments that can be implemented on the same topic.

Conclusion

The continuous rise of renewable energy systems calls for the need of using a different type of control methodology for inverters that is able to provide grid supporting services as a synchronous generator. A novel technique called grid-forming inverter was developed that can provide these services. Different types of grid-forming control structures were introduced in chapter 1, along with the advantages and disadvantages of each control method. According to the thesis objective, defined in the introduction and abstract, which depends on choosing a control topology suitable for good defined inertial and dynamic response with inner supporting controllers, three grid-forming control strategies were chosen for implementation and comparison of their dynamic behavior, that are VSM, GVSG, and CGVSG.

The case study designed for testing the reference control structures was introduced at the start of chapter 2, detailing the complete control block structure of the three grid-forming methods and circuit line diagram of the system. The modelling and tuning of the controllers were exploited in chapters 2 and 4.

The inner current and outer voltage controllers were tuned in chapter 2 along with the virtual impedance and phase lock loop. Following that, the chapter concludes by designing the active power controller parameters for VSM, Time constant and drag

coefficient, to define the VSM dynamic behavior. The main objective was to design all of the controllers with a suitable bandwidth that prevents instability caused by the dynamic interactions between these controllers.

The modelling of the other two grid-forming inverters, GVSG and CGVSG, was performed in chapter 4 with defining a range of data for their active power controller coefficients through inequality constraints.

A Simulink model was developed for testing these three grid-forming inverters in chapters 3 and 5. Three main tests were defined to check the reference control methodologies. A step power setpoint test shows the dynamic behavior of changing the reference power setpoint of the inverter to verify the response speed and overshoot of the electric power in following its reference. Step frequency and ramp frequency tests are described to investigate the inertial response and frequency supporting capabilities for the grid.

Chapter 3 implements the defined tests on the VSM, while chapter 5 apply them on GVSG and CGVSG. A final comparison is performed at the end of chapter 5, collating the dynamic behavior and inertial response of VSM, GVSG, and CGVSG along with two other control methodologies derived from VSM and GVSG by replacing PLL with a constant reference frequency and adding PLL respectively.

The thesis concludes by choosing VSM and CGVSG as the most suitable control topologies for the application of this thesis. Both of these control structures have their advantages and disadvantages. The CGVSG has a slightly better dynamic response. However, the inertial response is integrated with the droop causing a higher power change during frequency perturbations that can exceed the inverter ratings.

Future Developments

Through the tests of the various control structures defined in the thesis, it was noticed that there exist some points that can be further addressed on this topic.

- Developing a small signal model for GVSG to explore the effect of adding a PLL on the overall system stability. Moreover, the small signal model can be analyzed to explain why adding a PLL causes the system to react very quickly to power setpoint variations but shows a very slow dynamics in case of frequency perturbations as shown in section 5.5.

- The tuning criteria defined for GVSG and CGVSG can be investigated for further development to define another inequality constraints that can lead to better performances. Also, the tuning can be improved to meet the requirements of microgrid applications.

- Investigating the effect of active power dynamics on the voltage allowing for a more efficient definition of the active and reactive power flows instead of assuming a decoupled power flow.

Bibliography

[1] Eu-Eurostat, "22% of energy consumed in 2021 came from renewables," 19 January 2023. [Online]. Available: https://ec.europa.eu/eurostat/web/products-eurostat-news/w/DDN-20230119-1.

[2] A. Zygierewicz and L. S. Sanz, "Renewable Energy Directive, Revision of Directive (EU) 2018/2001," European Parliament, 2021.

[3] T. QORIA, E. ROKROK, A. BRUYERE, B. FRANÇOIS, and X. GUILLAUD, "A PLL-Free Grid-Forming Control With Decoupled Functionalities for High-Power Transmission System Applications," *IEEE Access,* vol. 8, pp. 197363-197378, 2020.

[4] D. B. Rathnayake, R. Razzaghi and B. Bahrani, "Generalized Virtual Synchronous Generator Control Design for Renewable Power Systems," *IEEE Transactions on Sustainable Energy,* vol. 13, no. 2, pp. 1021-1036, 2022.

[5] G. RANCILIO, "Battery Energy Storage Systems for Ancillary Services Provision," 2016.

[6] V. Nemes, "Inertia Ancillary Service Market Options," Australian Energy Council , 2021.

[7] R. Rosso, X. Wang, M. Liserre, X. Lu and S. Engelken, "Grid-forming converters: an overview of control approaches and future trends," *IEEE Open Journal of Industry Applications,* vol. 2, pp. 93-109, 2021.

[8] Australian Energy Market Operator , "Voluntary Specification for Grid-forming Inverters," 2023.

[9] J. Liu, Y. Miura and T. Ise, "Comparison of Dynamic Characteristics Between Virtual Synchronous Generator and Droop Control in Inverter-Based Distributed Generators," *IEEE TRANSACTIONS ON POWER ELECTRONICS,* vol. 31, no. 5, 2016.

[10] D. B. Rathnayake, M. Akrami, C. Phurailatpam, S. P. Me, S. Hadavi, G. Jayasinghe, S. Zabihi and A. B. Bahrani, "Grid Forming Inverter Modeling, Control, and Applications," *IEEE Acess,* vol. 9, p. 114781–114807, 2021.

[11] R. Liu, C. Xue and Y. Li, "Parameter Feasible Region Construction of Generalized Virtual Synchronous Generators with Improved Damping Capability," in *2023 11th International Conference on Power Electronics and ECCE Asia*, Jeju, Korea, 2023.

[12] R. Majumder, B. Chaudhuri, A. Ghosh, R. Majumder, G. Ledwich and F. Zare, "Improvement of stability and load sharing in an autonomous microgrid using supplementary droop control loop," *IEEE Trans. Power Syst.*, vol. 25, no. 2, pp. 796-808, 2010.

[13] S. D'Arco and J. A. Suul, "Virtual Synchronous Machines – Classification of Implementations and Analysis of Equivalence to Droop Controllers for Microgrids," in *IEEE Grenoble Conference*, Grenoble, 2013.

[14] U. Tamrakar, D. Shrestha, M. Maharjan, B. P. Bhattarai, T. M. Hansen and R. Tonkoski, "Virtual Inertia: Current Trends and Future Directions," *Applied Sciences*, vol. 7, no. 7, p. 654, 2017.

[15] T. QORIA, F. Gruson, F. Colas, X. Guillaud, M. -S. Debry and T. Prevost, "Tuning of Cascaded Controllers for Robust Grid-Forming Voltage Source Converter," in *2018 Power Systems Computation Conference (PSCC)*, Dublin, Ireland, 2018.

[16] A. El-Deeb, "CURRENT MODE CONT ROL OF REAL/REACT IVE POW ER," Advanced Generator Control Lectures, 2020.

[17] S. Buso and P. Mattavelli, "Digital control in power electronics," Power electronics Lectures, 2006.

[18] S. D'Arco, J. A. Suul and O. B. Fosso, "Control System Tuning and Stability Analysis of Virtual Synchronous Machines," in *IEEE Energy Conversion Congress and Exposition*, Denver, CO, USA, 2013.

[19] D. Cudazzo, "ANALYSIS OF THE INVERTER CONTROL, INTERFACING AN ESS TO THE GRID, FOR COPING VOLTAGE DIPS," Politecnico di Milano, 2016.

[20] F. Palombi, "HVDC INERTIA SUPPORT," Politecncio di Milano, 2018.

[21] X. Wang, Y. W. Li, F. Blaabjerg and P. C. Loh, "Virtual-Impedance-Based Control for Voltage-Source and Current-Source Converters," *IEEE Transactions on Power Electronics*, vol. 30, no. 12, pp. 7019-7037, 2015.

[22] "Power Flow through Transmission Line | Two Bus System," eeeguide, 17 November 2016. [Online]. Available: https://www.eeeguide.com/power-flow-through-transmission-line/.

[23] V. Kaura and V. Blasko, "Operation of a phase locked loop system under distorted utility conditions," *IEEE Transactions on Industry Applications*, vol. 33, no. 1, pp. 58-63, 1997.

[24] "For a standard 3rd order system determine $\zeta, \omega n, \omega d$ and tp.," Power System engineering (EE 3203).

[25] Vanderbilt University, "The Cubic Formula," [Online]. Available: https://math.vanderbilt.edu/schectex/courses/cubic/.

A Appendix A

3rd order system dynamic characteristics

Let's consider a 3rd order system with a characteristic equation.

$$a_3 s^3 + a_2 s^2 + a_1 s + a_o$$

We can think of this equation as a 2nd order dominant 3rd system. Hence,

$$a_3 s^3 + a_2 s^2 + a_1 s + a_o = (s + p)(s^2 + 2\zeta \omega_n s + \omega_n^2)$$

$$= s^3 + (p + 2\zeta \omega_n)s^2 + (2\zeta \omega_n p + \omega_n^2)s + \omega_n^2 p$$

By equating both sides the following equations can be obtained

$$a_3 = 1$$

$$a_2 = (p + 2\zeta \omega_n) \tag{1}$$

$$a_1 = (2\zeta \omega_n p + \omega_n^2) \tag{2}$$

$$a_o = \omega_n^2 p \tag{3}$$

From (1), (2), and (3)

$$a_1 = \frac{a_o}{p} + (b_2 - p)p$$

$$p a_1 = a_o + (b_2 - p)p^2$$

Then a 3rd order characteristic equation can be written in terms of coefficient p accordingly

$$p^3 - a_2 p^2 + a_1 p - a_o = 0$$

Solving the previous equation to get the values of p. Then, the dynamic characteristics of the 3rd order system can be obtained by substituting p value into (3) and (1)

$$\omega_n = \sqrt{\frac{a_o}{p}}$$

$$\zeta = \frac{a_2 - p}{2\omega_n}$$

$$\omega_d = \omega_n\sqrt{1 - \zeta^2}$$

Note that the 3rd order system dynamics can be represented by the previous equations only if it is a 2nd order dominant system.

List of Figures

List of Tables

List of symbols

VSM	Virtual Synchronous Machine
GVSG	Generalized Virtual Synchronous Generator
CGVSG	Compensated Generalized Virtual Synchronous Generator
PLL	Phase Lock Loop
PWM	Pulse-Width Modulation
PCC	Point of Common Coupling
PI	Proportional Integral
ROCOF	Rate of Change of Frequency
SCR	Short Circuit Ratio
FFR	Fast Frequency Response
BESS	Battery Energy Storage System

Acknowledgments

As I finish this chapter of my academic journey, I would like to express my profound gratitude to those who have been influential in this accomplishment of the conclusion of this thesis.

To my colleagues at work, your unwavering support and guidance have always inspired me and contributed to my personal and professional growth. Thank you for creating a comfortable, friendly environment at the workplace.

To my supervisor, Professor Roberto Perini, I would like to thank you for presenting such exceptional opportunity for me. Your academic guidance and constructive feedback have been pivotal in refining my work. Your academic rigor and knowledge inspire me, making you a role model.

To my co-supervisor, Francesco Palombi, I am deeply grateful for the countless hours you invested in mentoring me even with your busy schedule. Your encouragement, expertise, and inspiration have pushed me to purse prowess in my work.

I would like to express my deepest appreciation for my family. Your belief in my abilities have given me the strength to get through every impediment and accomplish my goals. Mom and Dad, your resilience and hard work have been a guidance and inspiration. To my friends, thank you for your help and support. It would not have been possible without you.

To my partner, Tania, your love, and endless support have been my sanctuary. Your belief in me, even in moments of doubt, has been a source of motivation.

Lastly, I would like to dedicate a moment to honour my grandfather, whose memory and teachings continue to guide me, and his legacy lives on through this academic achievement.